AN ANALYSIS OF RARE FINAL STATES PRODUCED BY 10 GeV/c K^+ MESONS IN HYDROGEN

Thesis

Submitted by

TIMOTHY M. RATCLIFFE, B.Sc.,

for the degree of

Doctor of Philosophy

University of Edinburgh

MARCH, 1974.

ABSTRACT

The rare final states produced by 10 GeV/c K^+ mesons in hydrogen are analysed, and values are given for many of their cross-sections, as well as details of the ambiguities present. Resonance production in these states is examined, and evidence is presented for the production of the K^*(890), the K_N(1420), the Σ(1385) and the f'(1514) resonances. Finally, the production characteristics of the anti-cascade particle are investigated and possible production mechanisms are suggested for the 3-body final states. No event was detected which could be reliably interpreted as involving the production of the anti-omega particle.

ACKNOWLEDGEMENTS

It is a pleasure to thank Dr. G.R. Evans, my supervisor, for constant help and encouragement with this work. I am grateful also to Dr. D.J. Candlin and Dr. N.E. Fancey for much help with computing and analysis of the data, to Dr. J.G. Colvine for help and advice during the initial part of this work, to Dr. J. Muir for assistance with travelling arrangements, to Dr. M.F. Votruba in Birmingham University, and to the scanning and measuring teams in both Edinburgh and Glasgow University, who did so much of the ground work. The assistance of Dr. P. Negus at Glasgow University is acknowledged. Thanks are due to Professor N. Feather, F.R.S., for extending the facilities of his department, to Mrs. Chester who made light of the enormous task of typing this manuscript, and to the Science Research Council for financial assistance.

Finally, I should like to thank my wife, Maddy, for her patience and understanding during the completion of this research.

CONTENTS

I. Introduction

II. The Data Analysis

III. The Calculation of the Cross-Sections

IV. Resonance Production in Rare Final States

V. Anti-Hyperon Production

Appendices:

2A A Justification of the Use of the χ^2 Method of Fitting

2B Fits to Hypotheses

3A Scanning Efficiency

3B Cross-Sections

3C Derivation of the Likelihood Function for N (Observed)

4A Phase Space

Inside Back Cover:

Reprint of, Nuclear Physics B <u>45</u> (1972) 77-87.

CHAPTER I

INTRODUCTION.

1.1 The Spectrum of Particle States
1.2 Quantum Numbers and Selection Rules
  1.2.1 G-Parity
  1.2.2 Parity
1.3 Resonance Production in K^+P Interactions
  1.3.1 The Reaction, $K^+P \rightarrow PK^o\pi^+$
  1.3.2 The $K\pi\pi$ Effective Mass
  1.3.2.1 The Q-region
  1.3.2.2 The L-region
  1.3.3 Other Results
  1.3.4 Z^*'s
1.4 The Rare Events
1.5 References for Chapter I.

CHAPTER 1

INTRODUCTION

1.1 The Spectrum of Particle States

When the nucleon is exposed to a beam of high energy mesons or nucleons, it is transformed into short-lived states of higher energy, which are known under various names, such as 'hyperons' or 'resonances'. These states form a spectrum of baryon states, of which the proton and neutron form an isospin ground state doublet. All other states can be reached by supplying the nucleon in the ground state with the necessary excitation energy.

Some of the excited states have different charges from the ground state. Some have different strangeness, or hypercharge. The excited states return to their ground state in one or several steps, with the emission of π-mesons, K-mesons, light quanta or electron-neutrino (lepton) pairs.

The charged mesons and the lepton pairs are charge carriers and are therefore emitted when there is a charge difference between excited and ground state. The K-mesons are also strangeness carriers and are emitted when the strangeness changes.

e.g. $$\Lambda^0 \longrightarrow p\,\pi^-$$

$$\Omega^- \longrightarrow \Lambda^0 K^-$$

$$\Sigma(1765) \longrightarrow N\bar{K} \quad .$$

An odd situation occurs with the lower excited states of different strangeness, such as the ones designated by Σ , Λ and

Ξ . They cannot de-excite by K-emission into the ground state because the mass of the K-meson is higher than the energy difference. These states, therefore, would be stable, if the conservation of strangeness were an exact law (such as the conservation of electric charge). In fact, however, strangeness is conserved in all interactions except the weak interactions. Therefore, there exist very slow transitions from these states to the ground state, with the emission of π-mesons, or lepton pairs, mediated by the weak interaction. Hence, the lowest states, with strangeness different from zero are metastable, and decay slowly into the only real stable state, which is the proton.

Apart from the baryon spectrum, there exists a second spectrum, called the meson spectrum, or boson spectrum. A careful analysis of the mesons produced by high energy collisions has revealed that there exists a series of excited states, referred to by various letters: ρ mesons, ω mesons, η meson.

In transitions from an excited state to a lower one, the energy difference is emitted mostly in the form of mesons, e.g. the ρ meson decays to two π mesons.

The dynamical basis of the baryon and boson spectra is not yet understood. However, inspection of the spectra definitely reveals multiplet structures which indicate certain symmetries, e.g. Isotopic spin multiplets are present in these spectra, i.e. the characteristic groups of levels of almost equal energy, which differ only in electric charge.

E.g. $\pi^+\pi^-\pi^o$, K^+K^o etc.

The most interesting observation, however, is the presence of an additional symmetry, to do with hypercharge, and known as SU(3) symmetry. This is based on the idea of quarks as the building blocks of the fundamental particles, a baryon being a combination of 3 quarks, and a meson being a quark-antiquark pair.

From such ideas, one can derive a super-multiplet structure for the levels of a 3-quark system, and of a quark-antiquark pair. This leads to the conclusion that a 3-quark system gives rise to singlets, octets and decuplets, and that a quark-antiquark pair to singlets and octets only. A possible baryon octet is shown in Fig. 1.1a, and a boson nonet in Fig. 1.1b.

It was the use of such multiplets which led to the prediction and subsequent discovery of the Ω^- particle, strangeness -3.

1.2 Quantum Numbers and Selection Rules

Particle states may be divided into two groups, viz. "stable" particles which decay through weak or electromagnetic interactions, and "resonances" which decay via the strong interaction. The lifetimes of these states are correspondingly different. Thus, the stable particle lifetime varies from $>10^{30}$s for the proton, to 10^{-17}s for the Σ^o, while the resonances normally have a lifetime of $\sim 10^{-23}$s. The Heisenberg uncertainty relation, $\Delta E \Delta t \approx h$ indicates that a lifetime $\approx 10^{-23}$s corresponds to an uncertainty in energy (mass) ≈ 65 MeV. The width of the stable particles is zero for practical purposes, whereas the resonance has more of a

FIG 1.1

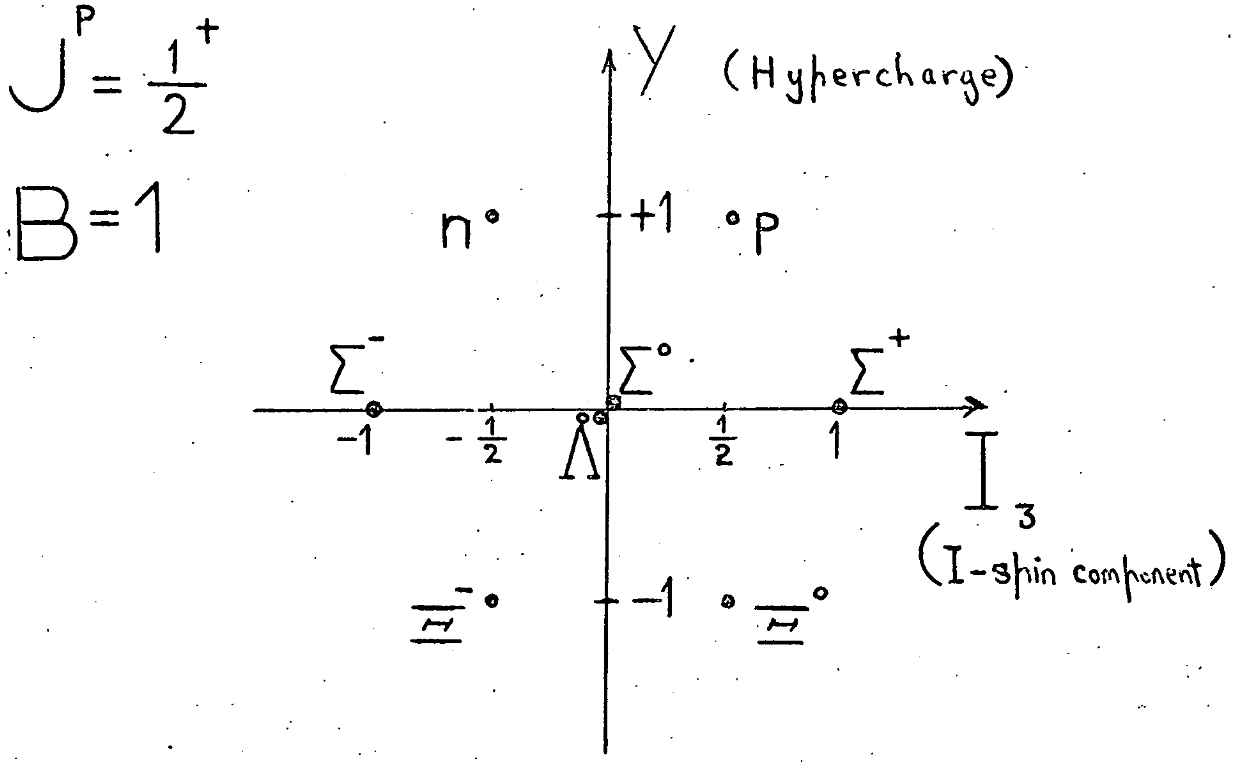

a) A Baryon Octet

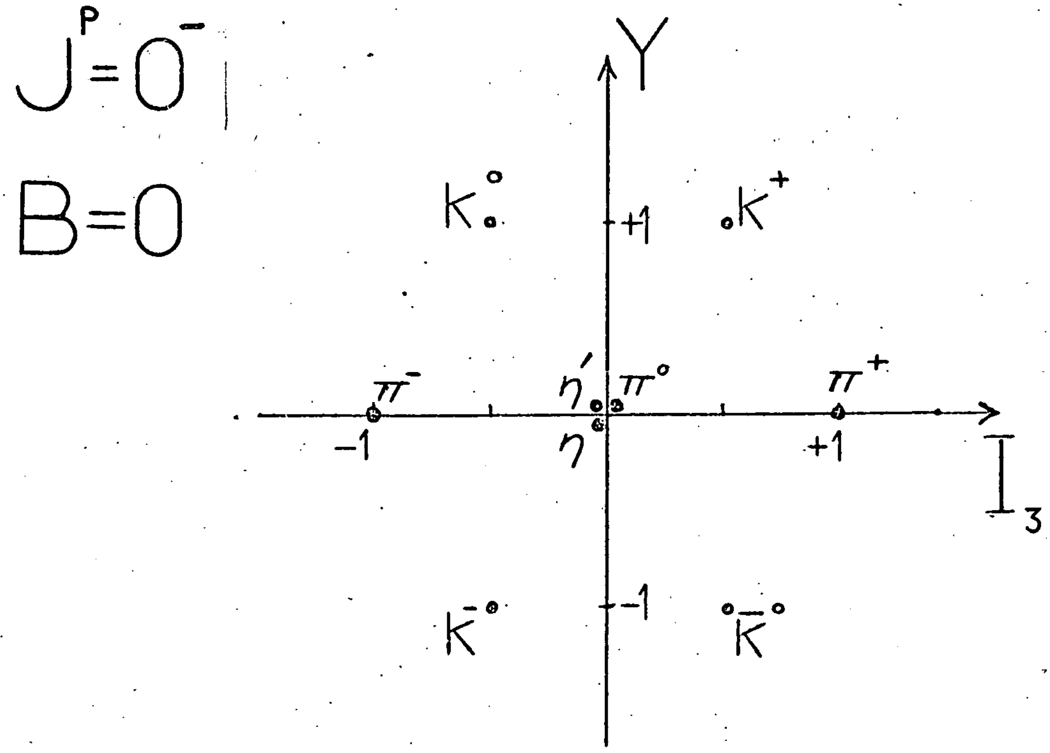

b) A Boson Nonet

statistical nature, giving rise to a mass distribution which resembles a "bump" rather than the "spike" of a stable particle.

A particle state may be defined by the numbers, M, , J, P, I, Q, S, B, L_μ, L_e, G (for non strange mesons), where

a) M is the mass of the state in MeV,

b) Γ is the width of the state, related to its lifetime, τ, by $\Gamma = \frac{1}{\tau}$ where $1\ (\text{MeV})^{-1} = 7 \times 10^{-22}\text{s}$, or $1\text{s}^{-1} \approx 7 \times 10^{-22}$ MeV.

c) J is the spin of the state.

d) P is the intrinsic parity.

e) I is the isotopic spin. The number of charge states is given by $2I + 1$.

f) Q is the electric charge quantum number.

g) S is the strangeness quantum number.

h) B is the baryon number, $= 0$ for all meson states or excited meson states.

i) L_μ, L_e are the lepton numbers, zero for all particles except the neutrinos, the electron, the muon, and their antiparticles.

j) G is the G-parity, defined later.

A nomenclature which has become commonly accepted is that $I = \frac{1}{2}$, $S = 0$ resonances are called N^*'s, and $I = {}^3/2$, $S = 0$ resonances are called Δ's, baryon resonances with $S = -1$ are called Y^*'s, subdivided into Λ's and Σ's according to their I-spin.

Instead of strangeness, a convenient quantity in discussing elementary particles is the hypercharge, Y, defined as

$$Y = S + B.$$

For "strange" particles, the charge, Q, differs from I_3, the third component of I-spin, by a constant which is characteristic of the multiplet, i.e.

$$Q = I_3 + \tfrac{1}{2}Y \quad .$$

1.2.1 G-Parity

An additional quantum number is introduced in the case of mesons. This is the G-parity quantum number, or "isotopic parity" quantum number. To understand G-parity one must first look at C, the charge-conjugation operator. This operator transforms a particle state into its anti-particle state, i.e.

$$C \left| X \right\rangle = \left| \bar{X} \right\rangle ,$$

where $\bar{X}$ has opposite charge and strangeness to X. Strong and electromagnetic interactions are assumed to be invariant under C. For the neutral, non-strange mesons, particle and anti-particle are indistinguishable, e.g. γ, π^o. Thus, these states will be eigenstates of C with eigenvalue $\pm$ 1. (It may be shown that the C-parity of γ is -1, and thus that the C-parity of the π^o is $+1$, from $\pi^o \longrightarrow \gamma\gamma$.) To extend this symmetry to the charged members, one defines the G-parity,

$$G = C \, . \, R = C \exp(i\pi \; I_2)$$

where R is the rotation of 180° around the y-axis in I-spin space. Then

$$G \begin{pmatrix} \pi^+ \\ \pi^o \\ \pi^- \end{pmatrix} \longrightarrow - \begin{pmatrix} \pi^+ \\ \pi^o \\ \pi^- \end{pmatrix} .$$

Thus, the G-parity of pions is -1. The minus sign arises from the fact that $R(\pi) \rightarrow -(\pi)$, since the eigenvalue of R for neutral non-strange states $= (-1)^I$. In general, the G-parity of a multiplet, I of mesons, of which the neutral member has a charge-conjugation parity, C_n, is

$$G = C_n(-1)^I .$$

If a system is coupled strongly to sub-systems of G-parity, G_1, G_2, G_3, ..., its G-parity will be defined by

$$G = G_1 \cdot G_2 \cdot G_3 \ldots\ldots ,$$

e.g. the observation of $\rho \longrightarrow \pi^+\pi^-$ leads to $G(\rho) = +1$. For n pions, $G = (-1)^n$.

This gives rise to a very important selection rule for strong interactions. An even (or odd) number of pions cannot be transformed into an odd(even) number of pions, if the system is an eigenstate of G.

1.2.2 Parity.

The wavefunction of any fundamental particle is an eigenstate of the parity operator, P, with eigenvalue ± 1.

i.e. $P\psi = +\psi$ even parity.

$P\psi = -\psi$ odd parity.

In practice, one is concerned with systems of at least two particles, where the whole wave function can be considered as the product of the intrinsic parities of the individual particles, and the parity of the orbital angular momentum part of the wave function. From the properties of spherical harmonics, it may be seen that the parity is given in terms of the orbital angular momentum quantum number, L, by

$P(L) = (-1)^L$.

The parity of the proton is chosen to be +1, and from this one can deduce the parity of the pions to be -1.

Since parity is conserved in strong interactions, one can make predictions about the J^P of the resonant state from its decay products, e.g., one which decays to two pions must have $J^P = 0^+, 1^-, 2^+, \ldots$ etc. (so-called "natural" spin-parity assignment), since the product of the intrinsic parities = +1, and the angular momentum part = $(-1)^L$ which is +1 if $L = 0, 2, \ldots,$ and -1 if $L = 1, 3, \ldots$ etc. High values of angular momentum are inhibited by the barrier effect.

Thus, the experimenter attempts to measure the mass and width of observed resonances, and from their decay angular distributions, or Dalitz Plot populations (which are also a function of spin), determine the J^P and I-spin quantum numbers.

These states may be compared with those predicted by the quark model, as a guide to the success of that scheme. States having quantum numbers which cannot be formed from a three-quark system, or a quark-antiquark pair, are called "exotic".

Meson states are given descriptive names, according to their J^P values, i.e.

a) 0^+ states are called scalar particles.

b) 0^- states are called pseudoscalar particles, e.g. π, η, because $P\psi = -\psi$, unlike most scalars under an inversion.

c) 1^- states are called vector particles, e.g. $K^*(890)$ $\phi(1019)$.

d) 1^+ states are called axial vector particles, since true vectors obviously change sign under an inversion ($x_i \longrightarrow -x_i$). E.g. A_1(1070).

e) 2^+ states are called tensor particles. E.g. f(1270), K_N(1420).

1.3 Resonance Production in K^+p Interactions

One must now examine more specific interactions, in particular those involving collisions of the proton, available in a liquid hydrogen target, with incident K^+ mesons.

It is known that the three and four-body final states from K^+p interactions are dominated by resonance production, and that an important fraction of the reactions proceed through quasi-two body states in which the K-meson and/or the nucleon are excited to the well-known K^*(892) and Δ(1236) resonances. The contribution of resonant processes giving final states of high multiplicities is less well-known. Its systematic study may provide information on resonance production and decay. The theoretical models describing multibody final states (multi-peripheral, statistical etc.) often neglect resonance production, so that a better understanding of the experimental situation may lead to improved models where it would be included.

1.3.1 The Reaction $K^+p \rightarrow pK^o\pi^+$

The reaction, $K^+p \rightarrow pK^o\pi^+$ (1)

is known to be dominated by the production of a few resonances, namely,

$K^*(892)$

$K^*(1420)$ - often called $K_N(1420)$

$\Delta^{++}(1236)$.

Each of these resonances is clearly observable, i.e. the signal to noise ratio is large. In Fig. 1.2 is shown the effective mass distribution for $M(K^o\pi^+)$ and $M(p\pi^+)$ from a K^+p experiment at 9 GeV/c, by V.G. Lind et al.$^{(1)}$.

The K^o is produced strongly forward in the C.M.S., the proton strongly backward, and the π^+ either strongly forward, or strongly backward, depending on whether it is a decay product of the $K^*(892)$, or of the $\Delta^{++}(1236)$.

Reaction (1) is considered as being composed of 4 channels (assumed to be non-interfering), namely

$$K^+p \longrightarrow K^{*+}(892)p \qquad (2)$$

$$K^+p \longrightarrow K_N^+(1420)p \qquad (3)$$

$$K^+p \longrightarrow \Delta^{++}(1236)K^o \qquad (4)$$

$$K^+p \longrightarrow pK^o\pi^+ \quad \text{(non resonant)}.$$

It may be seen from Fig. 1.3 that, for this channel, the fraction of observed quasi-two body reactions is approximately constant at a level ~ 60 - 70°/o over the range of incident momentum from 2 to 12.7 GeV/c.

Table 1.1 shows the relative fractions of events arising from the four possible channels, in the present experiment.

If one plots the distributions in $-t$, the four-momentum transfer squared, for reactions 2, 3, 4 (from the initial proton to the final proton in reactions 2 and 3, and to the $p\pi^+$ system in 4), one finds a dip in the cross-section at $-t \lesssim 0.1\ (\text{GeV}/c)^2$, which is considered to be due to the

FIG1.2

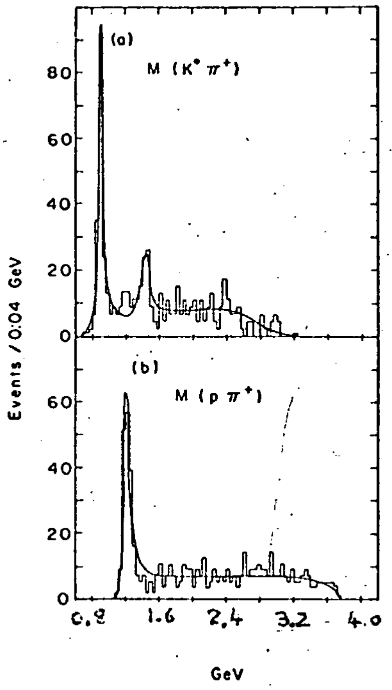

Effective mass of $M(K^{o}\pi^{+})$ and $M(P\pi^{+})$ from $K^{+}P$ interactions at 9 GeV/c. Taken from V.G Lind et al.(1)

FIG 1.3

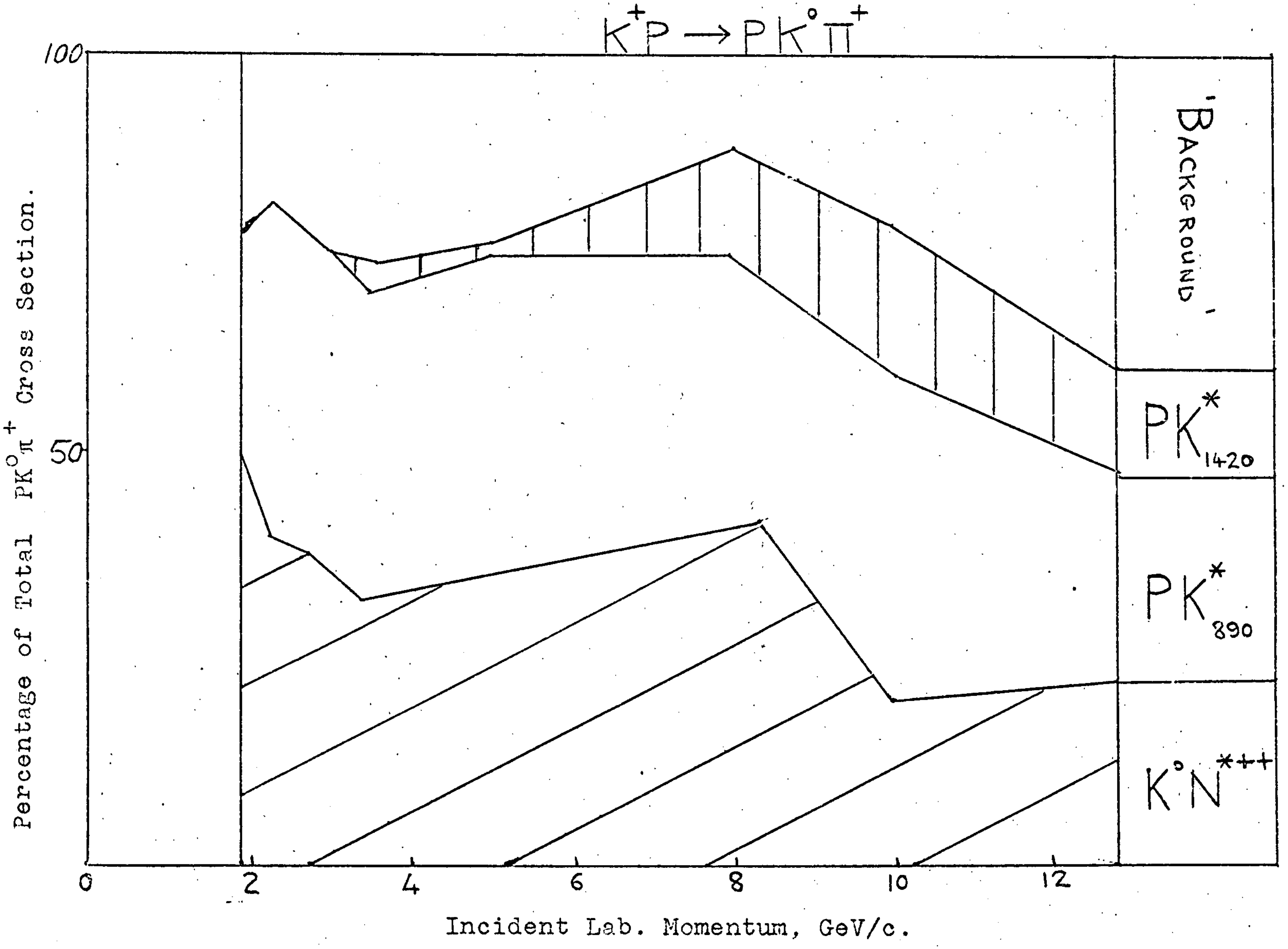
$K^+P \rightarrow PK^\circ\pi^+$
100
50
0
2
4
6
8
10
12
Percentage of Total $PK^\circ\pi^+$ Cross Section.
Incident Lab. Momentum, GeV/c.
'Background'
PK^*_{1420}
PK^*_{890}
$K^\circ N^{*++}$

TABLE 1.1 (see Ref. (2))

$K^+p \rightarrow K^0\pi^+p$

	Resonance	Mass (GeV)	Width (GeV)	Fraction	σ (μb)
1.	$\Delta^{++}(1236)$	1.206 ± 0.004	0.086 ± 0.008	0.27 ± 0.02	72 ± 10
2.	$K^{*+}(892)$	0.895 ± 0.002	0.058 ± 0.005	0.36 ± 0.02	96 ± 14
3.	$K_N^+(1420)$	1.425 ± 0.006	0.115 ± 0.020	0.19 ± 0.02	51 ± 9
4.	$K^0\pi^+p$ (non-resonant)			0.18 ± 0.02	47 ± 8
					266 ± 32 μb

Note that the K^+p total cross section = (17.3 ± 0.1)mb $^{(3)}$.

dominance of vector meson exchange(4), the particular mesons being the $\rho(765)$ (and the $\omega(748)$ meson). It was also concluded(2) that the decay angular distributions of the $K_N^+(1420)$ favoured a 2^+ or 3^- over a 1^- assignment for J^P values. The $K_N(1420)$ decays to two pseudoscalar particles, so its spin parity must be natural, i.e. 0^+, 1^-, 2^+,... . The angular decay distribution rules out 0^+, and previous work(5) ruled out 1^-, so that 2^+ and 3^- are the most likely assignments. The $K^*(892)$ is established as a 1^- particle.

Similar results were obtained by V.G. Lind et al.(1), who estimated that the J^P of $K_N^+(1420)$ is 2^+, with 18°/o pseudoscalar and 72°/o vector meson exchange in its production, the same proportion as for $K^*(892)$ production.

The results of the study of K^* production indicate that the reactions can be grouped into two classes, one with no exchange of charge $Q = 0$, and the other with charge exchange $Q = 1$, e.g. $K^+p \rightarrow K^{*0}\Delta^{++}$. It is found that $Q = 0$ reactions proceed by vector meson exchange while $Q = 1$ reactions have π-exchange. The observation of a dip near $t = 0$ in the differential cross-section, $\frac{d\sigma}{dt}$ for $Q = 0$ reactions, is characteristic of vector meson exchange reactions, while the non-observation of such a dip in $Q = 1$ reactions is consistent with other pion-exchange reactions.

1.3.2 The $K\pi\pi$ Effective Mass

1.3.2.1 The Q-region

One may divide the $K\pi\pi$ mass region into two distinct parts. The first, between 1.2 and 1.4 GeV/c^2, called the Q-region, and the second between 1.7 and 1.8 GeV/c^2, called the

L-region.

The combined distribution of the $K\pi\pi$ mass from the reactions,

$$K^+p \longrightarrow K^+\pi^+\pi^-p \qquad (5)$$

$$K^+p \longrightarrow K^o\pi^o\pi^+p \qquad (6)$$

is shown in Fig. 1.4. This shows the well-known low-mass enhancement between 1.2 and 1.4 GeV/c^2, known as the Q. If one treats the Q-region structure as a single bump, "the Q", then its production is highly peripheral, most events having a four-momentum transfer squared, t, of modulus less than 0.3 $(\text{GeV}/c)^2$. One experiment(6) which fitted an exponential e^{-bt} to the differential cross-section in the Q-region found a value of $b = 7.1 \pm 0.2\ (\text{GeV}/c)^2$. If the Q-region is considered as a single object (as it was when first discovered) then the 1972 Particle Data Group(7) give the mass as

$$m = 1298.8 \pm 11.3 \text{ MeV}/c^2, \text{ with a width,}$$

$$\Gamma = 82.5 \pm 21.6 \text{ MeV}/c^2.$$

However, the Q-region does not have a simple Breit-Wigner shape, and the number of people who see structure in this region is at least equal to the number of those who do not, and the number of sub-peaks and their position in the Q vary widely from experiment to experiment.

The Q has never been observed in the reaction

$$K^+p \longrightarrow K^o\pi^+\pi^+n,$$

and thus its isospin was taken to be = ½. (This was later confirmed in K^+D experiments(8).)

The Q decays predominantly into $K^*(890)\pi$, and $K\rho$ as may be seen by plotting the two-particle effective masses in this

FIG14

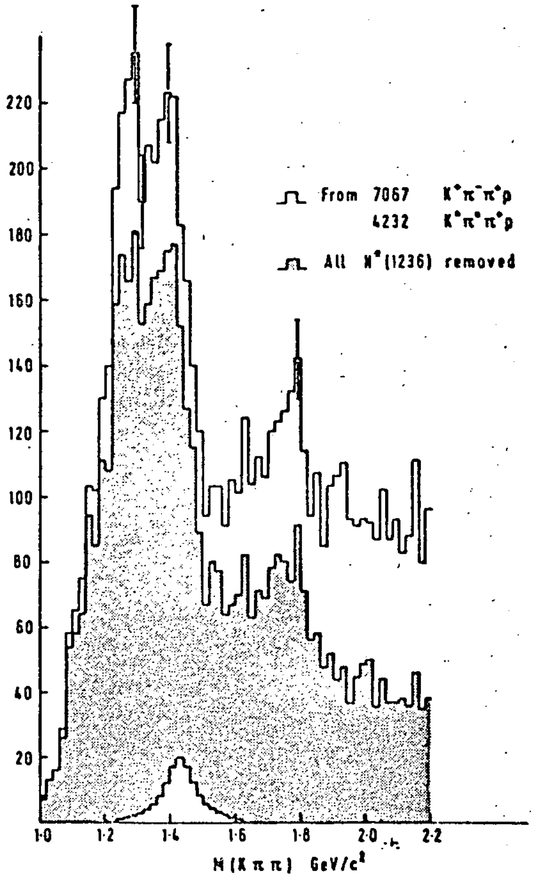

The distribution of $K\pi\pi$ invariant mass between 1.0 and 2.2 GeV/c^2. The unshaded histogram contains all $K^+\pi^-\pi^+$ and $K^o\pi^o\pi^+$ events in this range; the shaded histogram shows the effect of removing all N^* production. An estimate of the maximum $K_N(1420)$ contribution is also shown. - From K.W.J. Barnham et al.$^{(6)}$

region. Furthermore, the absence of signal in the $K\pi$ channel in the Q-region, suggests that states of the unnatural spin-parity series, 0^-, 1^+, 2^-, ... dominate the Q. All experiments performed so far have suggested a strong preference for the 1^+ assignment.

The possibility of more than one resonance in this region arose from the apparent variation in the mass of the "$K^*(1300)$" observed in different experiments, and the first observation of the actual splitting of the "$K^*(1300)$" was by Goldhaber et al. in 1967 in a K^+p experiment at 9 GeV/c(9).

The data from the present experiment also suggested that the Q was split, with a dip of ≈ 3 s.d. below the line joining the peaks. Thus, an attempt was made(6) to fit this Q-region using 3 models.

1) The sum of two incoherent resonances.
2) The sum of two coherent resonances.
3) The sum of two partially coherent resonances.

All three models provided a good fit to the data. It is of interest that the parameters describing the lower resonant amplitude in (3), notably,

$$m = 1.24 \pm 0.005 \text{ GeV/c}^2$$
$$\Gamma = 0.11 \pm 0.015 \text{ GeV/c}^2,$$

correspond well with the mass and width of the "C-meson" or the $K_A(1240)$, where the subscript 'A' indicates unnatural J^P.

This meson was studied in annihilation in $p\bar{p}$ at rest, into $K\bar{K}\pi\pi$ (10), and was found to have a mass of 1240 MeV/c^2, with a width of ≈ 130 MeV/c^2. The C-meson is in fact considered to be the only well-established candidate in the $K\pi\pi$

mass region below 1400 MeV/c^2, at the present time.

However, the Dalitz Plot distributions, and the angular decay distributions from the present experiment strongly support the hypotheses that the Q-enhancement consists of two 1^+ resonances.

The nature of the Q-region was also investigated using data from the International K^+ Collaboration(11), with ≈ 96,000 events at fourteen beam momenta, in the range, 2.5 ⟶ 12.7 GeV/c. This collaboration used a "World Tape" containing data from many experiments, including the present one. The reactions investigated were

$K^+p \longrightarrow K^+\pi^+\pi^-p$ (77,267 events)

$K^+p \longrightarrow K^0\pi^+\pi^0p$ (18,806 events).

To measure the spin-parity of the Q, they analysed the angular distributions of the dominant two-step decay,

$Q \longrightarrow K^{*0}\pi^+ \longrightarrow K^+\pi^-\pi^+$ (K^{*0} is the $K^*(892)$).

Their results gave $J^P = 1^+$ (although allowing lesser fractions where $J^P \neq 1^+$). Furthermore, the Dalitz plot densities gave good fits only to $J^P = 1^+$, and their results were clearly incompatible with the interpretation of the Q as a single resonance.

1.3.2.2 The L-region

Above the $K_N(1420)$ is the "L-region", i.e. a very definite bump around 1800 MeV/c^2. Enhancements in the $K\pi\pi$ and $K\omega$ effective masses near 1800 MeV/c^2 were first reported by Bartsch et al.(12). This enhancement was first thought to be simply a $K_N(1420)\pi$ threshold enhancement, but further evidence for decay to $K^*(890)\pi$ and $K^*(890)\rho$ from this experiment, has helped establish the L as a true resonance. Good evidence for decay to $K^*(890)\omega$ was also found.

The Particle Data Group Table of 1972 gave as the mass and width: L(1770)

$$m = 1763 \pm 10 \ \mathrm{MeV}/c^2$$
$$\Gamma = 100 \ {}^{+100}_{-50} \ \mathrm{MeV}/c^2$$

with an I-spin = ½, and $J^P = 2^-$ favoured, with 1^+ and 3^+ not excluded.

1.3.3 Other Results

In addition to studying the Q and L regions, and quasi-two body final states, the collaboration also submitted a paper to the Lund Conference on "A Double Regge Model Analysis of the reactions $K^+p \rightarrow K^+\omega^0p$, and $K^+p \rightarrow K^+\phi^0p$ at 10 GeV/c". (Birmingham-Glasgow Collaboration).

Using a modified CLA model (Chan, Loskiewicz, and Allison(13)), they considered the reaction

$$K^+p \longrightarrow K^+\omega^0p \qquad \omega^0(783) \longrightarrow \pi^+\pi^-\pi^0$$
$$K^+p \longrightarrow K^+\phi^0p \qquad \phi^0(1019) \rightarrow K^0\overline{K}^0, \ K^+K^- .$$

Their results showed that the modified double Regge model used in the analysis appeared to provide a good description of single particle distributions. This was especially true for the $K^+p \rightarrow K^+\omega^0p$ channel, where the parameters required no change between 6 and 10 GeV/c incident Kaon momentum.

1.3.4 Z^*'s

A 'Z^*' is a strange baryon resonance with $S = +1$, i.e. $Y = 2$. Over the last few years, several experiments have been performed to try to detect baryon resonances with hypercharge, 2, in K^+p and K^+D collisions. If such resonances do exist, the consequences are very far reaching. Firstly, the well-established hadron resonances have quantum numbers which permit their classification as quark-antiquark (mesons), or triple quark states. Each quark is assumed to have Baryon number, $B = \frac{1}{3}$, and only one quark has non-zero strangeness $S = -1$. Thus, a Z^* will not fit this scheme since one would require five quarks to form such a state, e.g. referring to Table 1.2, giving the quark quantum numbers, one possibility would be

$$Z^* \equiv \bar{Q}_3 Q_2 Q_2 Q_1 Q_1$$

with charge, +1.

R.L. Cool et al.(14) measured very accurately the total cross-section for K^+p and K^+D collisions between 0.9 and 2.4 GeV/c incident momentum, and found one bump in the $I = 0$ and another in the $I = 1$ state. Since then, several total cross-sections, phase shift analyses and production experiments have been performed. The bumps are around 1.25 GeV/c for K^+p and 1.15 GeV/c for K^+D. Assuming these bumps to be resonances, Cool et al. calculated that the masses would be

$$m = 1.863 \pm 0.020 \text{ GeV/c}^2 \text{ with } \Gamma = 0.150 \text{ for } Z_0^*.$$

$$m = 1.910 \pm 0.020 \text{ GeV/c}^2 \text{ with } \Gamma = 0.180 \text{ for } Z_1^*.$$

The latest data indicates that the $I = 0$ state is still very confused and suggest an elastic resonance at $\approx$ 1800 MeV/c^2

TABLE 1.2

'Quark Quantum Numbers'

Quark	B	I_3	S	q/e
Q_1	$\frac{1}{3}$	$+\frac{1}{2}$	0	$+\frac{2}{3}$
Q_2	$\frac{1}{3}$	$-\frac{1}{2}$	0	$-\frac{1}{3}$
Q_3	$\frac{1}{3}$	0	-1	$-\frac{1}{3}$

with a width of 300-600 MeV/c^2. However, the Particle Data Group still find the existence of exotic resonances a very open question, and suggest that very much more precise data is needed. It may be that production of possible Z^*'s is strongly inhibited by the abundant production of K^*, K_N, and Δ's.

There was no evidence found in the present experiment to suggest the existence of these states.

1.4 The Rare Events

An event is classed as "rare" if it includes at least two observed strange decays in the final state. Their cross-sections are of the order of 10μb as opposed to several hundred μb for common events. The K^+p total cross section is, at 10 Gev/c, (17.3 ± 0.1)mb$^{(3)}$. The analysis of these events provided values for previously unpublished cross-sections, as well as much information on the anti-cascade. The lowest energy state for production of a charged $\overline{\Xi}^+$ occurs in

$$K^+p \longrightarrow \overline{\Xi}^+ p \Lambda^0$$

with a C.M. energy of 3.375 GeV, requiring a beam momentum > 5.0 GeV/c. Because of the requirement of production of two baryons along with the $\overline{\Xi}^+$, the production cross-section is low, i.e. ~ few μb., so that the 51 fits obtained to $\overline{\Xi}^+$ states from the analysis of the rares, represent a significant contribution to the world data on mass, lifetime and production characteristics of these states.

There was a special interest in the rare events because of the possible production of an anti-omega particle, never seen before, partly because of its high mass and very low production cross-section. However, although possible candidates were seen, they were ruled out on the grounds that there were other more likely interpretations of the event. The first anti-omega was seen by J.H. Allardt in December 1970 in a K^+D experiment at 12 GeV/c$^{(15)}$. The reaction was

$$
\begin{aligned}
K^+D \longrightarrow\ & \overline{\Omega}^+ \Lambda^0\, \Lambda^0 p \pi^+ \pi^- \\
& \hookrightarrow \overline{\Lambda}^0 K^+ \\
& \qquad \hookrightarrow \bar{p} \pi^+
\end{aligned}
$$

where the $\bar{p}$ annihilated in the chamber, forming a "star".

REFERENCES FOR CHAPTER I

(1) Lind, V.G. et al., Nuclear Physics B14 (1969) 1-10.

(2) Barnham, K.W.J. et al., Nuclear Physics B28 (1971) 175.

(3) Galbraith, W. et al., Physical Review, 138B (1965) 913.

(4) Bialas, A., CERN Topical Conference on Hadrons, Vol. I (1968), 218.

(5) Bassompierre, G. et al., Nuclear Physics B13 (1969) 189.

(6) Barnham, K.W.J. et al., Nuclear Physics B25 (1970) 51.

(7) 'Review of Particle Properties', Physics Letters 39B (1972).

(8) Firestone, A. et al., Physical Review D 5(3) (1972) 505.

(9) Goldhaber, G., Physical Review Letters 19 (1967) 976.

(10) Astier, A. et al., Nuclear Physics B10 (1969) 65.

(11) Bingham, H.H. et al., Nuclear Physics B48 (1972) 589.

(12) Bartsch, J. et al., Nuclear Physics B8 (1968) 9; and
Bartsch, J. et al., Physics Letters 22 (1966) 357.

(13) Chan Hong Mo et al., Nuovo Cimento 57A (1968) 93.

(14) Cool, R.L. et al., Physical Review Letters 17 (1966) 102.

(15) Firestone, A. et al., U.C.R.L. Report 20235 (1970). and, Physical Review Letters 26 (1971), 410-413)

CHAPTER II

THE DATA ANALYSIS

2.1 Introduction

2.2 Delta-Ray Scanning

2.3 The Chamber

2.4 Scanning

    2.4.1 Topology of Events

    2.4.2 The Program 'CFSCAN'

    2.4.3 Consistency of Scanning

2.5 Measurement

2.6 The Program 'Geometry'

2.7 The Program 'Kinematics'

2.8 Choice of Hypotheses

2.9 Kinematic Output

2.10 Lifetime of Observed States

    2.10.1 The lifetime of the K_s^o meson

    2.10.2 The lifetime of the Λ^o-hyperon

    2.10.3 The lifetime of the Σ^+-hyperon

2.11 References to Chapter II.

CHAPTER II

EXPERIMENTAL BACKGROUND

2.1 Introduction

The data on which this work is based was drawn from several exposures of the 2m. Hydrogen Bubble Chamber (HBC) at CERN(1), to a beam of 10 GeV/c K^+ mesons. The main part of the work is based on exposures taken in 1968, although data collected in 1965/66 is also used. Table 2.1 gives a summary of the Runs.

Runs 1, 2, and 3 were analysed by Birmingham, Glasgow and Oxford Universities in 1966/67, and Runs 4, 5 by Birmingham and Glasgow and Edinburgh, from 1968 onwards. For the 1968 film, Birmingham took the even-numbered rolls of film, and Glasgow, the odd-numbered.

Runs 1 and 3 were found to have a high proton contamination, compared to runs 2, 4 and 5. It has been calculated by Lengler(2) that for 10 GeV/c secondaries, produced by 23 GeV/c protons at 0° from a Be target, the ratio of protons, pions and kaons, at the end of a 180 m beam line is

$$p : \pi^+ : K^+ = 300 : 77 : 1$$

so that protons will be the dominant contamination. This is particularly serious because of the relatively high pp total cross-section (40 mb against 17.3 mb for K^+p). It is known that Run 1 was subject to phase instability in the R.F. separators(2), and Run 3 had reduced beam purity, due to the opening

<u>TABLE 2.1</u>

	Run 1	Run 2	Run 3	Run 4	Run 5
Date	Dec. '65	June '66	July '66	Jan. '68	Feb. '68
No. of pictures	70,000	75,000	75,000	190,000	120,000
Magnetic field	17.30 kG	17.34 kG	17.34 kG	16.0 kG	17.34 kG

of collimators, because of poor secondary intensity.

The proton contamination in Runs 4 and 5 was estimated at less than 2°/o (3).

In part of Run 4, due to overheating in the magnet coils, the current was reduced from 10,000A to 9,000A, thus lowering the magnetic field value in the centre of the chamber.

i.e.

Roll numbers	Run	Magnet Current	
1A → 11B	4	10,000A	(Roll 3 - Bad film)
13A → 91B	4	9,000A	
(K^- film in here)			
261A → 379B	5	10,000A	

The distribution of beam momentum for fitted events on the final DST is shown in Fig. 2.0. The centre of the distribution is ≈ 10.08 GeV/c.

Since estimates of beam contamination were obtained by delta-ray scanning, this method will now be described.

2.2 Delta-ray Scanning

A delta ray is defined as an electron ejected with energy large compared to the ionisation potential. So the binding of the electrons can be neglected and their collisions with the incident heavy particles evaluated by means of the Rutherford scattering formula.

At relativistic velocities, a quantum-mechanical calculation results in a modifying factor so that the number of collisions in traversing an interval dx g cm^{-2} of the medium,

FIG 2.0

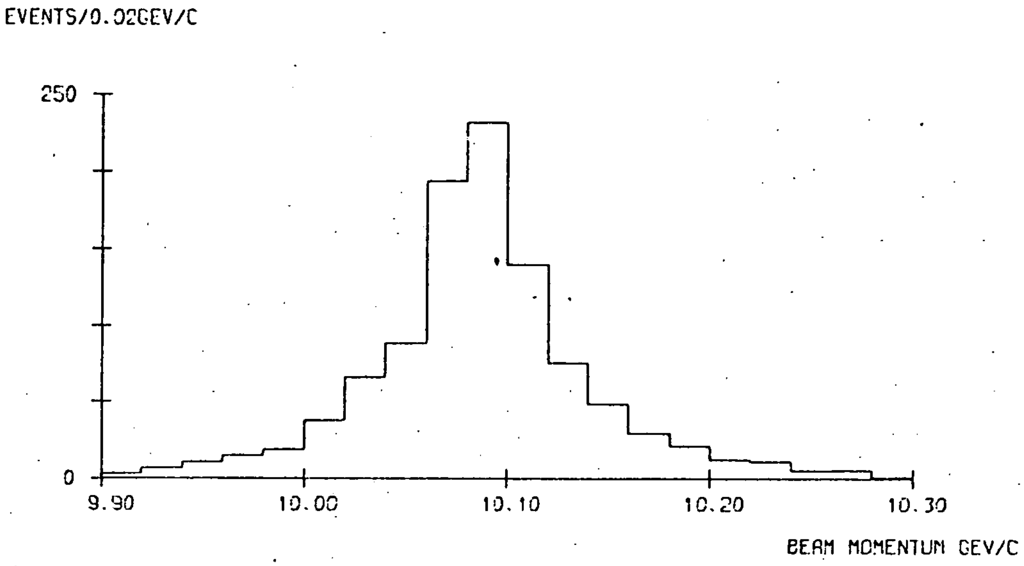

Distribution of beam momentum for fitted events resulting in energy transfers E' ⟶ E' + dE' is (4)

$$f(E')dE'dx = \frac{2\pi z^2 e^4 N_o Z\ dE'}{m_e v^2\ A\ E'^2}\ \left(1 - \frac{v^2}{C^2}\frac{E'}{E'_{max}}\right)dx \qquad (1)$$

where v and z_e are the velocity and charge of the incident particle, N_o is Avogadro's number, Z and A the atomic and mass numbers of the medium, and m_e the electron mass.

The maximum transferable energy, E'_{max}, is given by

$$E'_{max} = \frac{2m_e v^2}{1 - \beta^2} \qquad (2)$$

where $\beta = v/c$ for the incident particle (not electronic) and m_e = electron mass.

Thus, for a given momentum, a muon may transfer more energy than a kaon, which in turn may transfer more energy than a proton.

In fact, the maximum energy transferable by a 10 GeV/c

muon is ≈ 9 GeV
kaon is ≈ 0.4 GeV
proton is ≈ 0.11 GeV.

This fact was used,

a) to obtain an estimate of muon contamination,

b) to obtain an estimate of total kaon beam track length.

Delta-rays appear as single tracks, beginning on beam tracks, curving to the left and having minimum bubble density. Their curvature was measured on the table, using a template to classify them as type A(D101), type B(D102) or neither (momentum too low).

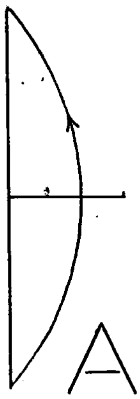

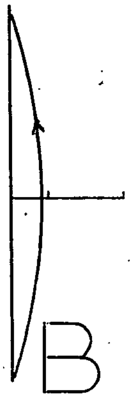

Type A corresponds to a momentum, p, in $0.11\ GeV/c < p < 0.4\ GeV/c$,

and Type B corresponds to a momentum $> 0.4\ GeV/c$.

Thus, all D102 types must be due to muons. From this, one can calculate the number of D101's due to muons and therefore calculate the number due to kaons (and which cannot be due to protons) and from equation (1), therefore estimate the total kaon track length.

2.3 The Chamber

The chamber used was the CERN 2m chamber(5), filled with liquid hydrogen at a temperature of 26°K, and a pressure of several atmospheres. At expansion, the pressure is reduced to nearly atmospheric pressure. The chamber contains $1.0\ m^3$ liquid hydrogen with a density of $62.75\ kg/m^3$ at 25.82 K and 1.9 atmospheres, at beam entry (i.e. after expansion). The magnetic field at the centre is nominally 17.4 kG, and four 50 mm cameras provide a visible volume of 200 cm × 50 cm × 60 cm. Fig. 2.1 shows the relative position of the chamber planes.

The beam enters the chamber in the X-direction, with a spread in the Y-direction. The spread of the beam is shown in Fig. 2.2 As shown in Fig. 2.3 , about 160 cm of the medial (i.e. beam) plane was visible to all four cameras. The chamber is viewed in the diagram, from the camera plate.

FIG 2.1

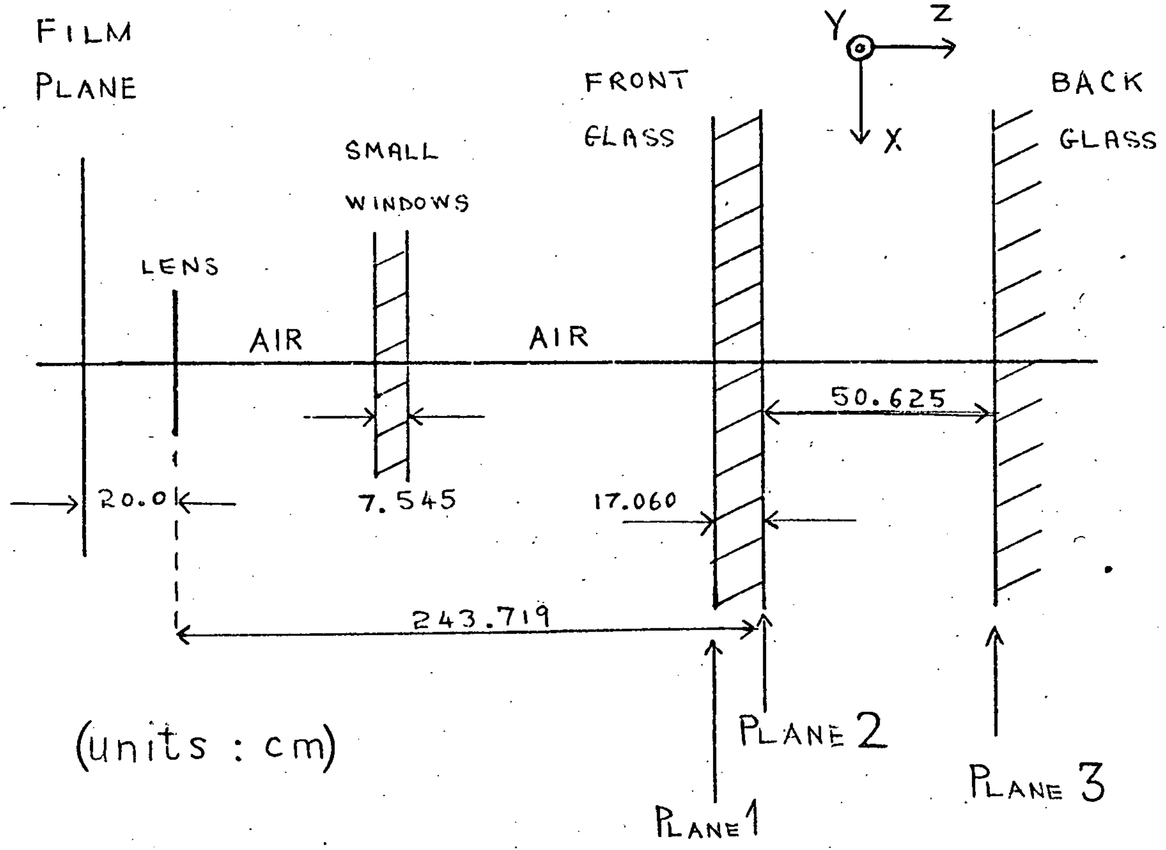

Relative Position of chamber planes

FIG 2.2

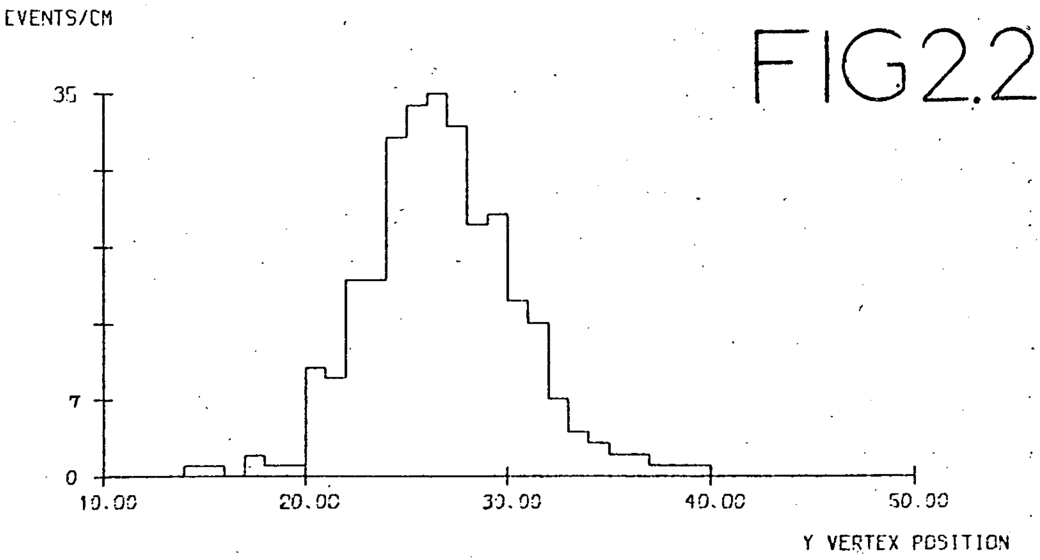

Spread of beam in Y-direction

FIG2.3

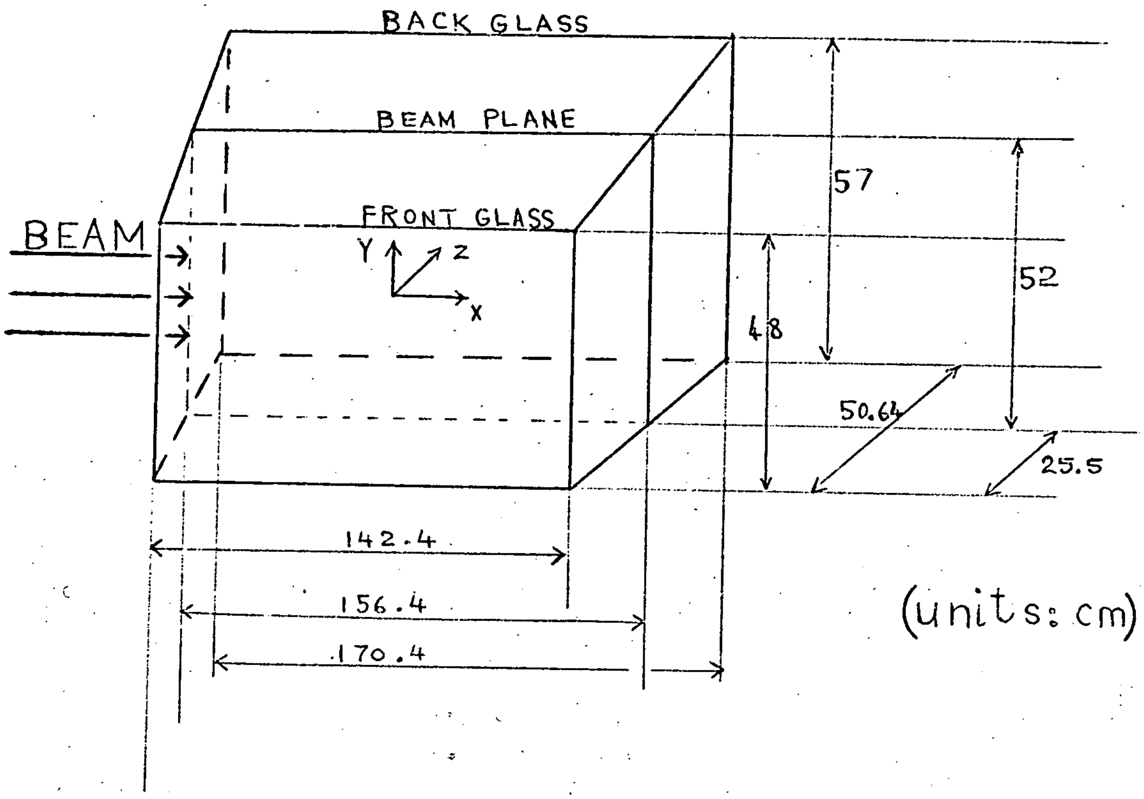

View of chamber from the cameras

FIG2.4

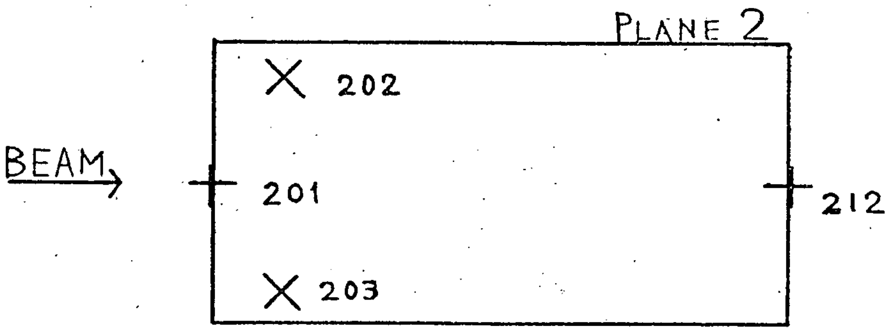

Fiducials - Plane 2.

There are fiducial marks on all three planes, to be used in the three-dimensional re-construction of the events. The scanning grid, used to provide a rough position of vertices for measurement, was based on the layout of the fiducial marks on plane 2, shown in Fig. 2.4.

In the X-direction, the fiducials, 201 - 212, were divided into 10 regions and in the Y-direction, fiducials 203 - 202, plus 1 cm (in the chamber) on either side, were divided into 10 regions. The first digit of the 3-digit fiducial name gives the plane on which the fiducial is etched. The fiducials on plane 3 were "gull-shaped", i.e.

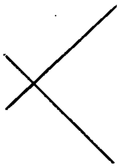

The positions of the fiducials mentioned above are given in Table 2.2.

The chamber was illuminated by three flashlamps with a light-pulse duration of approximately 200 μs.

Four cameras were used, with a focal length 182 mm., at f/32. The cameras were given names for use in scanning and measuring, viz.

camera	(1)	TOP 1
"	(2)	ENTRY 2
"	(3)	EXIT 3
"	(4)	BOTTOM 4.

The relative positions of the cameras on the camera plate are shown in Fig. 2.5 . The scanning grid was used with the TOP 1 view, with a (table:chamber) magnification of 0.8.

TABLE 2.2

Camera Window (no. 2). Plane 2

fiducial	X	Y	at 20°C, ± 0.05 mm.
201	0.0	194.90	units, mm.
212	1425.08	194.90	
202	125.10	389.50	
203	125.19	0.0	

FIG 2.5

Camera Plate of the 2m Bubble Chamber

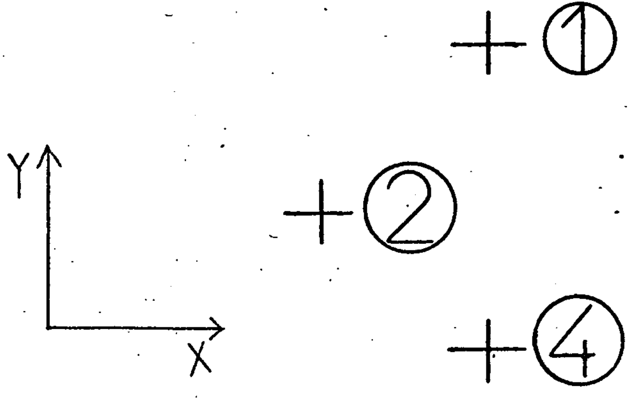

Camera	X	Y
1	410	600
2	110	300
3	710	300
4	410	0

units: mm ± 0.1 mm

2.4 Scanning

The scanning grid was divided (as described in Section 2.3), into 10 regions, denoted P, Q, ... X, Y, from beam entry to beam exit, and into 10 regions denoted 1,2,3... 10, from left to right across the table. On the scan sheet was recorded,

a) The roll and frame number.

b) The event number.

c) The topology (see later).

d) The grid position of the primary interaction, followed by the position of kinks (charged decays) and neutral decays (V^o's).

e) Comments - usually restricted to "COM V^o", if a neutral decay appeared to point to more than one event.

Every event was recorded, except two-prongs which were recorded, only every fifth roll.

"Common" events, i.e. events with at most one seen decay, were recorded only in grid regions $P \longrightarrow U$ inclusive, if the decay occurred below the top half of region, Y.

"Rare" events were recorded anywhere in the chamber.

A beam count was taken every 50 frames.

Events occurring in "bad" frames were not normally accepted (at the scanning stage) unless they were of special interest (e.g. a track which appeared to have a double kink, or a V^o pointing to a decay vertex). A "bad" frame is defined as one in which

a) whole or part of the frame has not been exposed;

b) the frame has been multiply exposed;

c) more than one of the three views is missing;

d) there are more than 30 tracks, of any sort, crossing the line separating regions R and S.

A check was kept on the number of bad frames.

Two scanners were employed, one with the grid on view TOP 1, with access to view EXIT 3 to resolve difficult events, the other with view BOTTOM 4. A V^o was accepted if it pointed to within 2 cm of the interaction, or decay vertex.

2.4.1 Topology of Event

The topology of an event is described by a three digit number, e.g. 201, 411, etc. The first digit gives the number of charged prongs leaving the primary vertex. The second digit gives the number of those charged prongs which are seen to decay (excluding $\pi\mu e$ decays), and the third digit gives the number of visible neutral decays associated with the event. For a "rare" event, the sum of the last two digits must be at least two.

2.4.2 The Program CFSCAN

The program "CFSCAN"$^{(6)}$ is a book-keeping program written at Glasgow University to look after the details of scanning information, comparison of two scans, and to produce a list of events to be measured.

Each scanner has a code name, consisting of a letter followed by a digit, and each event recorded on the scan sheet was transferred to a punch-card on an IBM card-punch. The information on each scan-card is exactly that on the scan-sheet. If any roll of film has been double-scanned, CFSCAN compares the information, accepts what is common to both, and prints out a a list of incongruities, which are then checked by a physicist in a third scan. This information from the third scan is punched on cards, and CFSCAN uses it to update the scanning record, stored on magnetic tape on the Glasgow University Computer, an IBM 360/44. The events found on a single scan are automatically accepted for measurement. The film from Run 1 and Run 3 which was re-scanned in Edinburgh, was completely double-scanned by scanners and check-scanned by the author, but only 2/9 of the 1968 film was double-scanned.

In Table 2.3 is given a list of the different topologies found at the scanning stage in 70 half-rolls of 9000A film.

2.4.3 Consistency of Scanning in Birmingham and Glasgow/Edinburgh

Six rolls of film which had been scanned and measured in Birmingham were scanned and measured in Edinburgh, and the results compared.

Birmingham scanned	37	"good" events.
Edinburgh scanned	39	"good" events,

of which 34 were common. Since the Glasgow scanning was known to be consistent with Edinburgh scanning, from a check on 27 half-rolls scanned by both, the assumption of consistency of scanning was assumed to be satisfactory.

2.5 Measurement

The great majority of the rare events were measured in Glasgow University on a "National" machine, and later re-measured on the SMP (Scanning Measuring Platten) machines.

TABLE 2.3

Topology	Number Found at Scanning Stage
201	3,106
202	322
203	32
211	58
212	7
401	2,752
402	242
403	11
411	89
412	9

Approximately 77°/o of all events sent for measurement succeeded in passing the Geometry programme$^{(7)}$ at the first attempt. All rare events found on a single scan were accepted without question for measurement. On average, less than ten candidates for rare events were presented per half roll of 750 frames, which means that the time consumed in loading and winding the film forms a large fraction of the total time taken for measurement, unless they are measured simultaneously with the common events. The same is true for ionisation consistency checking.

2.6 The Program "Geometry"

The principal task of the Geometry program is to calculate the momentum, p, at the centre of each track, and an error matrix, $\langle \partial p_i \; \partial p_j \rangle$ on this momentum. In addition, the program calculates the spatial coordinates of all vertices, together with errors, and also works out the topology of the event. The set of measured points for each track is fitted to a helix of radius ρ. From the parameters of the fitted helix, the momentum variables of the track used in the kinematic fits are calculated. These variables are all defined at the centre of the track, and are ϕ, the azimuthal angle, $\tan \lambda$, where λ is the angle of dip, and $\frac{1}{p}$, where p is the momentum of the track in GeV/c. The momentum p is given from the radius of the helix by

$$p = \frac{0.3 \; H\rho}{\cos \lambda} \times 10^{-3} \;\; \text{GeV/c}$$

where H is the Z-component of the magnetic field in kilogauss.

The program also calculates the "measurement error", σ, for each fit where σ is the R.M.S. displacement of the measured points about the fitted track (on film), normally $\sim 10\mu$. To the measurement errors calculated from the helix fit, are added the uncertainties in the momentum variables caused by multiple Coulomb scattering. This then gives the error on the momentum.

Note that $\frac{1}{p}$ is used as a variable rather than p, as this reciprocal is linearly related to the curvature of the track which is directly related to the measurements and therefore $\partial(\frac{1}{p})^2$ is expected to be more Gaussian than $\partial(p)^2$. Note also that the helix fits are mass dependent and each track may emerge from Geometry with three fits, one to a kaon, one to a pion, and one to a proton, each with different variables and errors. Those fits are stored in the Helix Fit List (HFL) in the record. The use of different values for the particle mass affects the results of helix fitting in two ways:

1) The momentum and angles differ because of the different slowing down corrections - this is significant only for low energy tracks.

2) The calculated errors differ because the Coulomb errors are mass-dependent.

For very low momentum tracks, four separate fits are carried out, using K, π, p and e masses.

2.7 The Program "Kinematics"(8)

This program takes a given reaction hypothesis and tests it against the data presented to it from the "Geometry" program.

Some fitting procedure has to be carried out for two reasons: firstly due to measurement errors, the kinematical variables will not satisfy energy-momentum conservation at an interaction vertex, and one needs to obtain the best estimate of the "true" values of these quantities, which will satisfy the constraints. The second reason arises from the lack of knowledge of the particle causing the track. The nature can sometimes be immediately seen from physical reasons, such as ionisation density, but only rarely, especially at 10 GeV/c. Therefore it is necessary to test a variety of hypotheses of particular mass assignments for one event, and this is done in the fitting program, using a χ^2 test as goodness-of-fit criterion. The theory of χ^2-testing demands variables whose errors are normally distributed.

From the geometry record, Kinematics calculates the direction cosines of a track,

$$\begin{aligned} \ell_x &= \cos\phi\cos\lambda \\ \ell_y &= \sin\phi\cos\lambda \\ \ell_z &= \sin\lambda \quad . \end{aligned}$$

The constraint equations at a vertex then become

$$\sum_i p_i \cos\phi\cos\lambda = 0 \quad \text{or} \quad \sum_i p_i \ell_{x_i} = 0$$

$$\sum_i p_i \sin\phi\cos\lambda = 0 \quad \text{or} \quad \sum_i p_i \ell_{y_i} = 0$$

$$\sum_i p_i \sin\lambda = 0 \quad \text{or} \quad \sum_i p_i \ell_{z_i} = 0$$

$$\sum_i \pm\sqrt{(p_i^2 + m_i^2)} = 0$$

Upon solution of these equations, the program also yields a new set of errors for the fitted variables which will in general be smaller than the measurement errors.

If σ_m is the error on the measured variable, X_m, then the program will choose as its best estimates, the variables, X_i, which satisfy

$$\chi^2 = \sum_i \frac{(X_i - X_m)^2}{\sigma_m^2} = \text{minimum}$$

- for a brief justification of this method, see Appendix 2A.

2.7.1 Kinematic Fitting

If one wishes to test an event against a given reaction hypothesis, one must first describe each track, and the particles at each vertex, as well as the order in which "Kinematics" must "fit" the event. The data describing this is fed in, on punched cards, which give, for each hypothesis

a) the topology and hypothesis number,

b) the number of tracks in the reaction, including the beam track,

c) the number of vertices, and the target particles at each vertex (0 for a decay),

d) one card per track giving (i) starting vertex number
   (ii) end vertex number
   (iii) electric charge
   (iv) code number (e.g. 5 for proton, 6 for Σ^+ etc.),

e) the total number of fits, and the order in which they should be attempted.

(The interaction vertex is normally given vertex number 1.)

In choosing a fitting sequence, the general philosophy is to first perform the fits which have the best chance of having the highest number of constraints - usually this is 3, corresponding to fitting a neutral decay to a vertex, where the momentum of the V- zero is unknown. This is known as a "3C-fit".

If one attempts a fit to a hypothetical charged decay at a vertex, usually this will be a 1C-fit, if the length of the decaying track is adequate to allow an estimate of its momentum or a 0C-fit, if it is straight.

A 0C-fit is not a fit at all, simply a calculation, and there can be no estimate of whether it is a good or a bad "fit" since it is not possible to calculate a χ^2-value. Sometimes a 0C-fit at a charged decay vertex gives two physical solutions, both of which must be tried. Events giving rise to 0C-fits (at the primary vertex) are not acceptable.

Hypotheses involving an unseen neutral from the production vertex, and a charged decay vertex with no associated V-zero, are likely to give rise to 0C-interaction fits. In Edinburgh, it was decided to fit only the 211-type topology in such cases, and not the 411-type, due partly to the very large number of such hypotheses which it would be necessary to construct and run, and also to the fact that such events would be fairly unreliable, due to the small number of constraints involved.

In Birmingham, it was decided to test such hypotheses, and in this way, fits were obtained to reactions such as

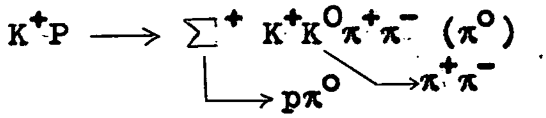

$$K^+P \longrightarrow \underset{\hookrightarrow p\pi^0}{\Sigma^+}\ K^+\underset{\searrow \pi^+\pi^-}{K^0}\pi^+\pi^-\ (\pi^0)$$

which were not attempted in Edinburgh.

2.8 Choice of Hypotheses.

There is a very large number of possible final states of the reaction

$$K^+p \longrightarrow \text{anything}$$, at a K^+ momentum of 10 GeV/c,

corresponding to a C.M.S. energy of 4.46 GeV. The different possibilities were computed by the program "HYPOTH" (9), which is told the C.M.S. energy, the initial state and which laws are to be conserved. From this list were selected the "rare" reactions which could give rise to at least two visible decays, and from this subset were chosen those reactions which it was thought possible to fit in Kinematics, having regard to the points mentioned in the previous section.

In this way, 362 hypotheses were chosen, with a maximum of four charged prongs and a description of each for Kinematics gave rise to ~ 5400 cards. The hypotheses were divided into four groups to avoid "overflows" in Kinematics, with each group containing approximately 10 202 type, 20 402 type, and 60 other hypotheses involving at least one charged decay.

In addition, a separate deck was made up of 26 212 type hypotheses and 25 411 type hypotheses, involving the decay of Ξ^-, $\bar{\Xi}^+$, Ω^-, or $\bar{\Omega}^+$ particles and an unseen neutral from the interaction vertex. These were run later but produced no fits.

The hypotheses numbers were agreed with Birmingham University and a list is given in Appendix 2B, along with the number of fits obtained in each laboratory.

As a summary of hypotheses tried in both laboratories, are listed below the numbers of each topology tried.

Topology	Number tried in Edinburgh	Number tried in Birmingham
202	39	39
203	8	30
211	46	46
212	50	88
402	77	77
411	66	150

2.9 Kinematics Output

Each Geometry tape submitted to 'Kinematics' results in the production of four Kinematics output tapes and four sets of print out - because there are four separate Kinematics decks of hypotheses. Each fit must be checked for consistency of ionisation density and for chi-squared probability. Any fit which involves either a production fit probability of $< 1^{\circ}/\mathrm{o}$ or an overall fit probability of $< 1^{\circ}/\mathrm{o}$ is rejected. Birmingham used the same criteria. This "bubble-density" checking is a very slow process with rare events because of film-winding and loading time. An event which is obscured may require more than one view to verify the fit. Where an event had more than one fit, no account was taken of the relative probabilities in deciding acceptable fits.

After the fits are verified, they are written on to a DST (Data Summary Tape) using the Rutherford Laboratory Program, "Judge" (10). For this purpose, a "choice-card" is punched out for each fit to tell Judge which fits to take, and which to ignore, on the Kinematics O/P tape. Obviously, this results in four separate DST's where the same event may occur on more than one tape. If the DST's are joined simply end-to-end, this creates difficulties in weighting events and calculating cross-sections, since it is necessary to know about the ambiguities when weighting an event and for this, it is necessary for the fits to be written up in strict numerical order. Therefore the author wrote a program, DSTMRG, which writes the combined D.S.T. in numerical order of frame number. This means also that a D.S.T. produced by a remeasure may be combined with the original D.S.T. at a later date. The events are now ready for analysis.

In the analysis of the Run 1 and Run 3 film, every event was re-examined after measurement and, where possible, given a chance of two re-measures if it failed to produce a fit.

In the Runs 4 and 5 film, the events were re-measured if they failed Geometry and later, every event was remeasured.

The care which needs to be taken when analysing rare events was amply demonstrated when one 411 type event which had failed to produce a fit, even though it looked a certain candidate for $\overline{\Xi}^+$ or $\overline{\Omega}^+$ (since the V^0 was almost certainly associated with the decay vertex), failed to produce a fit after careful measurement on the Vanguard Machine in Edinburgh. Although the V^0 gave a good fit to $\overline{\Lambda}^0 \longrightarrow \bar{p}\,\pi^+$, and the decay gave a good fit to

$$\overline{\Xi}^+ \longrightarrow \overline{\Lambda}^0 \pi^+ ,$$

the interaction fit failed. The most puzzling part was that for the lowest mass combination for a 411 of this type, i.e.

$$K^+p \longrightarrow \overline{\Xi}^+ p \pi^+ \pi^- (\Lambda^0)$$

the mass of the unseen neutral was calculated at only 900 MeV/c^2! i.e. there was not enough energy to form a Λ^o. The mystery was solved when the event was being remeasured as the measurer noticed a very slight kink on one of the prongs leaving the interaction. The event was measured again as a 421 and as expected gave a fit to

$$\begin{array}{l} K^+p \longrightarrow \overline{\Xi}^+\Sigma^+\pi^+\pi^- \\ \qquad\qquad\qquad\quad \hookrightarrow n\pi^+ \end{array}$$

which is, of course, a lower mass combination. However, this event had been scanned twice and measured twice before the Σ^+ - decay was noticed. Since this event increased the number of $\overline{\Xi}^+$'s found in Edinburgh by nearly 10°/o, this demonstrates one difference between working with common events and rare events.

2.10 The Lifetime of Observed States.

One may estimate the mean lifetime of states by making a logarithmic plot of observed lifetimes in bins of suitable size, and fitting a straight line to the data. However, putting data into bins results in a loss of information, viz. the position of each event in the bin. The 'Maximum Likelihood Method', which uses each individual event, should give a better result.

The Likelihood function, $\mathcal{L}$, which is a function of one parameter, τ , the mean lifetime, is the product of the probabilities of each event having that particular value of lifetime, assuming that the event came from a parent distribution characterised by the value τ. One then adjusts τ to maximise this probability.

the Likelihood function is,

$$\mathcal{L} = \prod_i \frac{1}{\tau} \frac{e^{-t_i/\tau}}{e^{-t_{min}/\tau} - e^{-t_{max}/\tau}}$$

where t_{max} and t_{min} are the upper and lower observable times for that event, due to the finite size of chamber and minimum visible track length (taken as 0.3 cm.). The above function, $\mathcal{L}$, may be maximised by Newton's Method, and this was the method adopted by the author.

2.10.1 Lifetime of the K_S^o meson

a logarithmic plot of the lifetime of 1075 K^o mesons observed in rare reactions in this experiment is shown in Fig. 2. 6 , where it is clear that there is a loss of events with very short lifetime ($< 0.1 \times 10^{-10}$S), due to the small distance travelled in the chamber by such particles.

A least-squares-fit was made to the points shown for $t > 0.1 \times 10^{-10}$S, to

$$\ell n\, N = at + b$$

(without weighting the points).

The best value for a is

$$a = -(1.232 \pm 0.05)$$

which corresponds to a mean lifetime of

$$= (0.811 \pm 0.03) \times 10^{-10}\text{S}.$$

Using the Maximum Likelihood Method gives

$$= (0.890 \pm 0.024) \times 10^{-10}\text{S} .$$

FIG 2.6

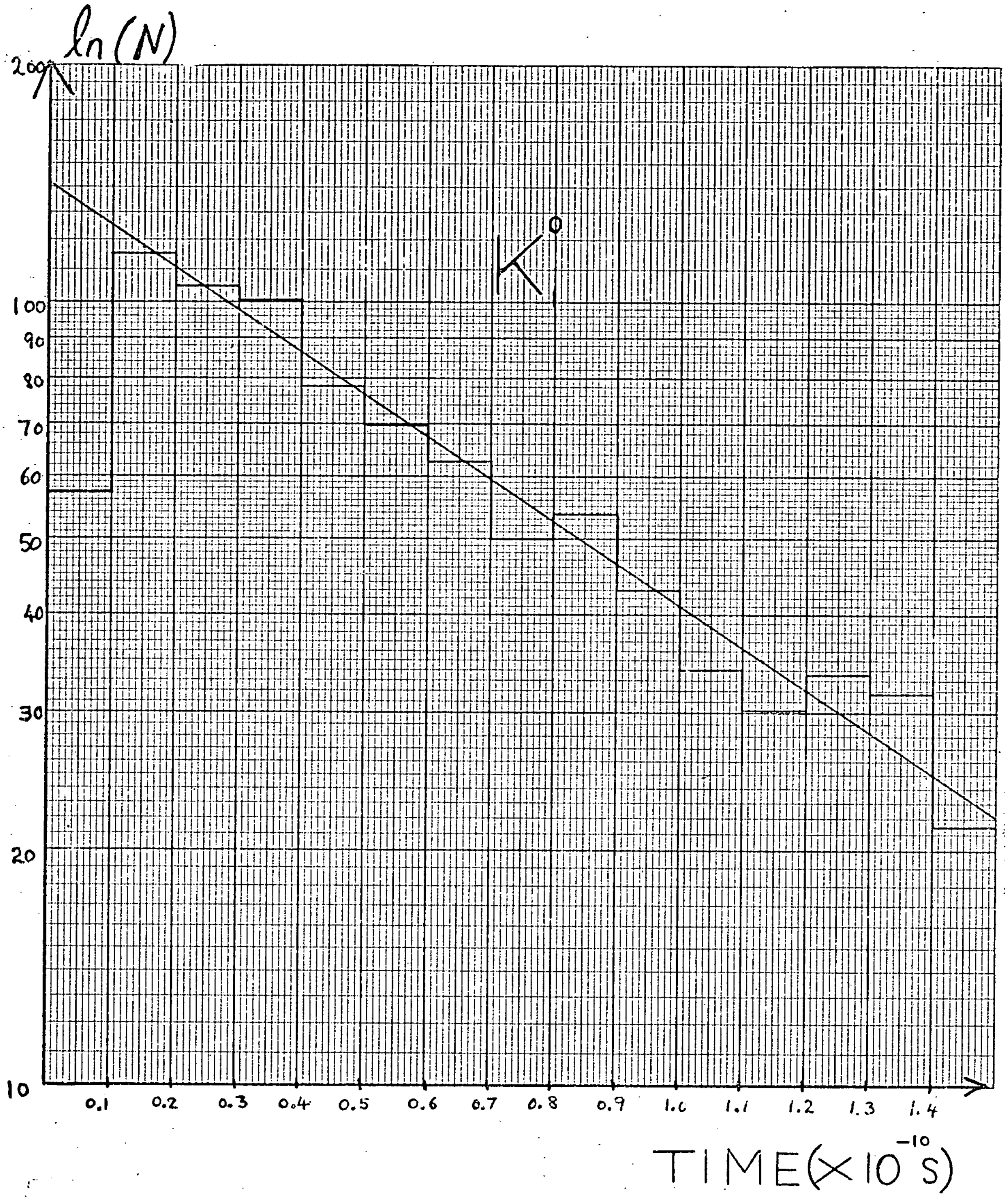

Logarithmic plot of lifetime for 1075 examples of the K_1^0. The fitted line corresponds to a lifetime of,

$$\tau = (0.811 \pm 0.03) \times 10^{-10} \mathrm{s}.$$

FIG 2.7

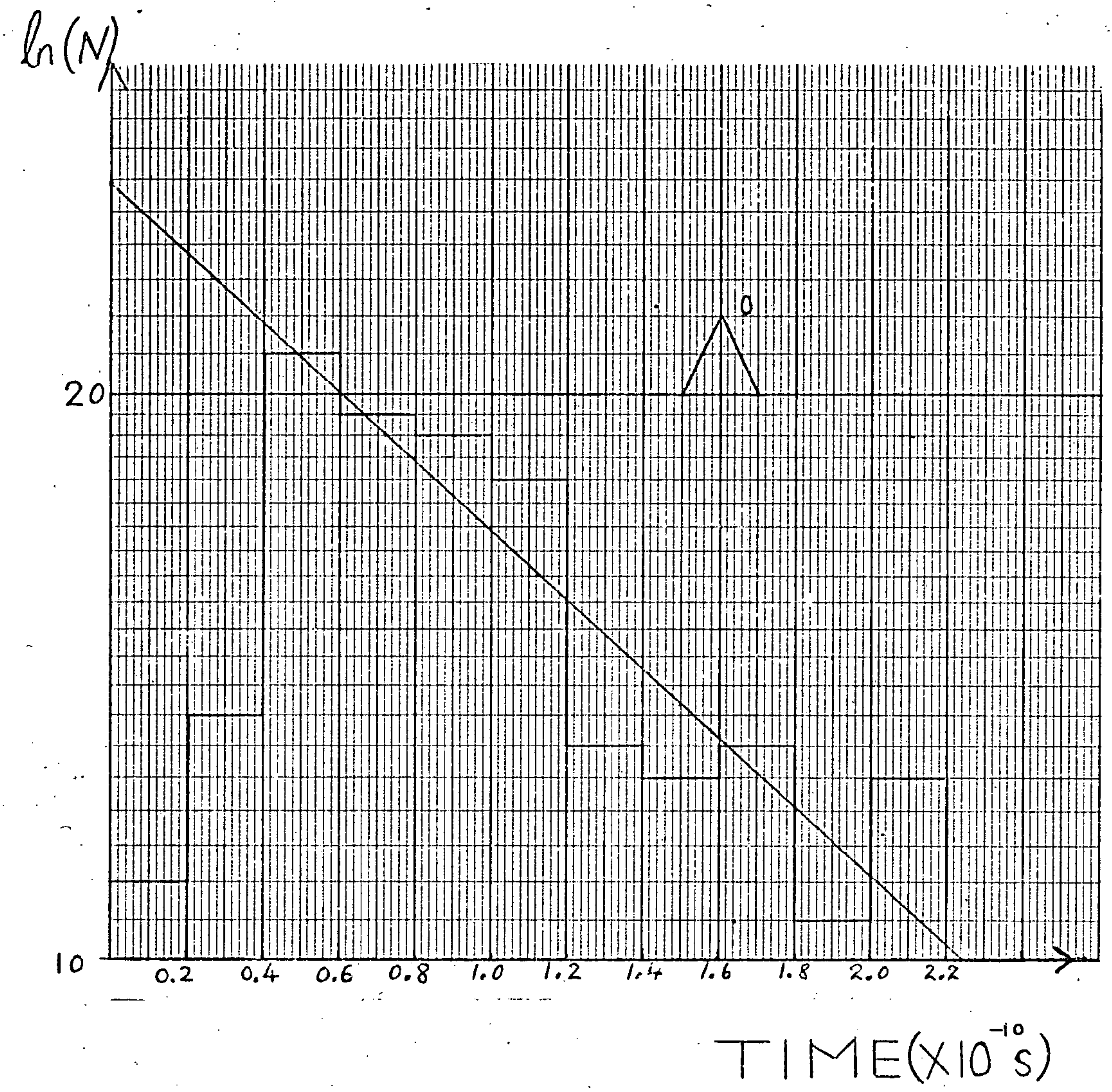

Logarithmic plot of lifetime for 336 examples of the Λ^0. The fitted line corresponds to a lifetime of,

$$\tau = (2.39 \pm 0.32) \times 10^{-10} s.$$

FIG 2.8

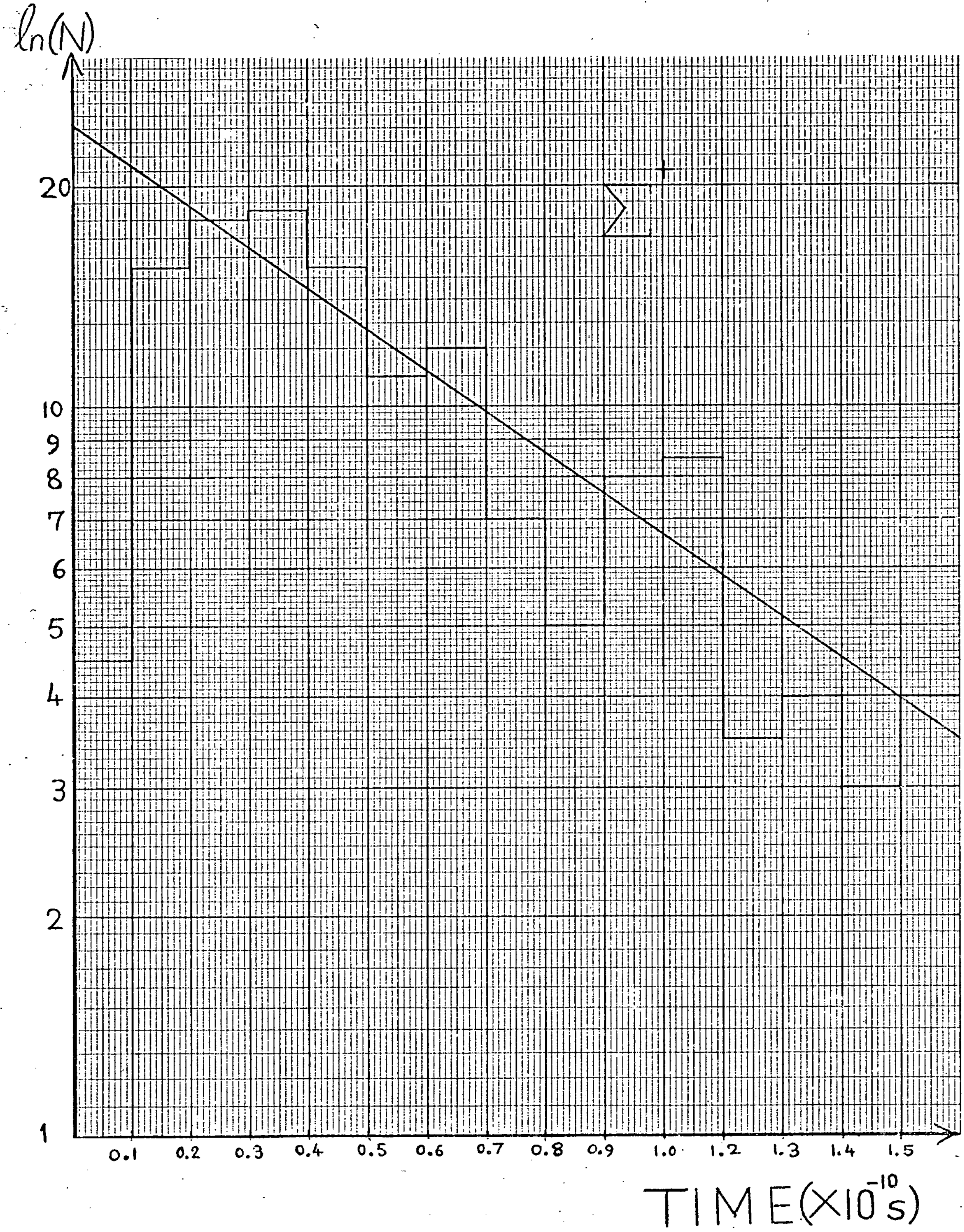

Logarithmic plot of lifetime for 245 examples of the Σ^+. The maximum likelihood lifetime shown is,

$$\tau = (0.773 \pm 0.053) \times 10^{-10}\text{s}.$$

This latter value may be compared with the latest value from the 1973 Particle Data Tables of

$$\tau = (0.882 \pm 0.008) \times 10^{-10}\text{s}.$$

The Likelihood function is slightly asymmetric, which means that the error should also be asymmetric, more positive than negative. The method employed to find the error assumes that the function is approximately asymptotically normal and this is true, for large numbers of events.

2.10.2 Lifetime of the Λ^{o}-Hyperon

A logarithmic plot of the lifetime of 336 Λ^{o}-hyperons is shown in Fig. 2.7 , where there is a clear loss of events for t $< 0.4 \times 10^{-10}$s.

The least-square fitted gradient of these points (again with no weighting) corresponds to a lifetime of

$$\tau = (2.39 \pm 0.32) \times 10^{-10}\text{s}.$$

The Maximum Likelihood lifetime is

$$\tau = (2.55 \pm 0.15) \times 10^{-10}\text{s}.$$

This may be compared with the 1973 accepted value of

$$\tau = (2.521 \pm 0.021) \times 10^{-10}\text{s}.$$

2.10.3 Lifetime of the Σ^{+}-Hyperon

The lifetimes of 245 Σ^{+}-hyperons observed in this experiment are shown plotted in Fig. 2.8.

The Maximum Likelihood lifetime for these states is

$$\tau = (0.773 \pm 0.053) \times 10^{-10}\text{s}$$

compared with the April 1973 value of

$$\tau = (0.800 \pm 0.006) \times 10^{-10} s.$$

Thus all three lifetimes investigated are totally consistent with the accepted values of April 1973.

2.11 REFERENCES FOR CHAPTER II

(1) C.E.R.N. - European Organisation for Nuclear Research.

(2) Lengler, H., CERN/TC/ Beam 65-4.

(3) Proctor, C. Thesis, Glasgow University, 1971.

(4) Perkins, D.H., 'Introduction to High Energy Physics', Addison-Wesley (1972) 25.

(5) 'Data of the 2m Bubble Chamber', CERN/D.Ph.II/200, 67-5.

(6) 'CFSCAN', Glasgow University Physics Department Program Library.

(7) 'The Geometrical Reconstruction of Bubble Chamber Tracks', J.W. Burren and J. Sparrow, (1963). NIRL/R/14.

(8) 'A Kinematical Fitting Program for the Analysis of Bubble Chamber Events' by A.G. Wilson, (1962), NIRL/M/38.

(9) 'Hypoth', Glasgow University Physics Department Program Library.

(10) 'A User's Guide to the 'Judge' Program' by T. Noland (1967).

CHAPTER III

THE CALCULATION OF THE CROSS-SECTIONS

3.1 Cross-Section

3.2 Consistency of Microbarn Equivalent for Birmingham and Edinburgh samples

3.3 Correction Factors

- 3.3.1 Scanning Efficiency
- 3.3.1.1 Edinburgh Sample Scanning Efficiencies
- 3.3.1.2 Birmingham Sample Scanning Efficiencies
- 3.3.2 Processing Efficiency for the Edinburgh Sample
- 3.3.2.1 Calculation for the Run 4 film
- 3.3.2.2 Calculation for the Run 5 film
- 3.3.2.3 Results for Processing Efficiency
- 3.3.2.4 Consistency of Processing in Edinburgh and Birmingham Laboratories
- 3.3.3 Lifetime Losses
- 3.3.4 Losses due to Small Angle Charged Decays
- 3.3.5 Losses due to Camera Azimuthal Angle
- 3.3.6 Events Lost Due to Neutral Decay Modes
- 3.3.7 The $K^0 \bar{K}^0$ System
- 3.3.8 Estimate of Loss due to Non-constrained Production Fits
- 3.3.9 Correction for Loss of Events in Kinematic Fitting

3.4 Combination of Cross-section from the Two Samples

3.5 Combination of Cross-section of Mutually Ambiguous Reactions

3.6 The Λ^0/Σ^0 Ambiguities

3.7 Error on Cross-section due to Random Fluctuation

3.8 Reliability of Single Constraint Interaction Fits

3.9 References for Chapter III

CHAPTER 3

THE CALCULATION OF THE CROSS SECTIONS

3.1 Cross-Section

By observing a sufficiently large number of occurrences of a given reaction, one can also measure the probability that it should occur.

Let the target contain N_o protons capable of participating in the reaction under study, and let there be observed, per second, n events of a predetermined kind. The number of particles in the beam is specified by the flux, ϕ, i.e. by the number of particles per second which cross unit area, normal to the beam direction. Then the probability per unit time of observing one event of a given kind, when there is one proton in the target is

$$P = \frac{n}{N_o} .$$

This probability is itself proportional to ϕ, and a parameter independent of the beam intensity is defined by the ratio

$$\sigma = \frac{P}{\phi} .$$

The parameter, σ, has the dimensions of an area, and is called a cross-section. The unit of measurement is the barn (10^{-24} cm^2), with its sub units, millibarn (mb) and microbarn (μb).

If the target contains N_H protons per unit volume, and the length of beam track = L, then

$$N = L \sigma N_H$$

is the number of times the reaction should occur.

The length of beam track may be calculated in several ways.

(i) By selecting a random sample, say 10°/o, of the film, and counting the number of good beam tracks crossing the chamber every 50 frames. From this, one can estimate the total number of tracks.

ii) Knowing the mean lifetime of the K^+ meson, and the fraction of its decays which go via

$$K^+ \longrightarrow \pi^+\pi^+\pi^-$$

i.e. by 'Tau' decay, one can count the number of identified (i.e. scanned and measured) events on a given sample of film, correct this number for scanning and processing losses, and use this to find the total number.

iii) By scanning and measuring (on the table) the number of delta rays, as explained in Section 2.2.

All methods demand that a check be kept on the number of "bad" frames, i.e. those not scanned.

Using the results of all three methods, the physicists at Glasgow University estimated a beam-track length of 188 ± 25 km on 29 half rolls, from a total number of 187 half rolls, for a fiducial length of 96 cm.

This corresponds to a microbarn equivalent of

$$\frac{\sigma}{N} = (0.22 \pm 0.03)\ \mu\text{b per event}$$

i.e. one seen event corresponds to a cross-section of $(\frac{\sigma}{N})$ μb.

3.2 Consistency of Microbarn Equivalent for Birmingham and Edinburgh Samples

The scanners at Glasgow University were asked to accept rare events over the whole of the scanning region, i.e. - 37.5 cm to + 97.5 cm = 135 cm.

However, if one examines the X-coordinates of fitted events in Fig. 3.1 , there is a clear fall-off at X = + 60 cm. near the end of the fiducial length defined as acceptable for common events. It is therefore necessary to impose a cut off at this point for the purpose of cross-section calculation, and the "rares" fiducial length then becomes 97.5 cm, which implies a microbarn equivalent of

$$\frac{\sigma}{N} = (0.216 \pm 0.03)\ \mu b \text{ per event.}$$

Examining Fig. 3. 2 , a plot of the X-coordinates of fitted events on the Birmingham sample of film, one sees that the distribution is relatively flat from X = -37.5 cm to X = +100 cm. Using this fiducial length of 137.5 cm, the Birmingham sample microbarn equivalent is estimated as

$$\frac{\sigma}{N} = (0.110 \pm 0.01)\ \mu b \text{ per event.}$$

A check was made on the consistency of these two estimates by comparing the number of fits to the reaction,

$$K^+P \longrightarrow \pi^+PK^0$$

where the K^0 is seen to decay, giving a 4C interaction fit, relatively free of ambiguities.

Using the above numbers, together with scanning efficiencies, the estimated ratio of fits in Birmingham to those in Glasgow is 1.56 ± 0.25.

FIG 3.1

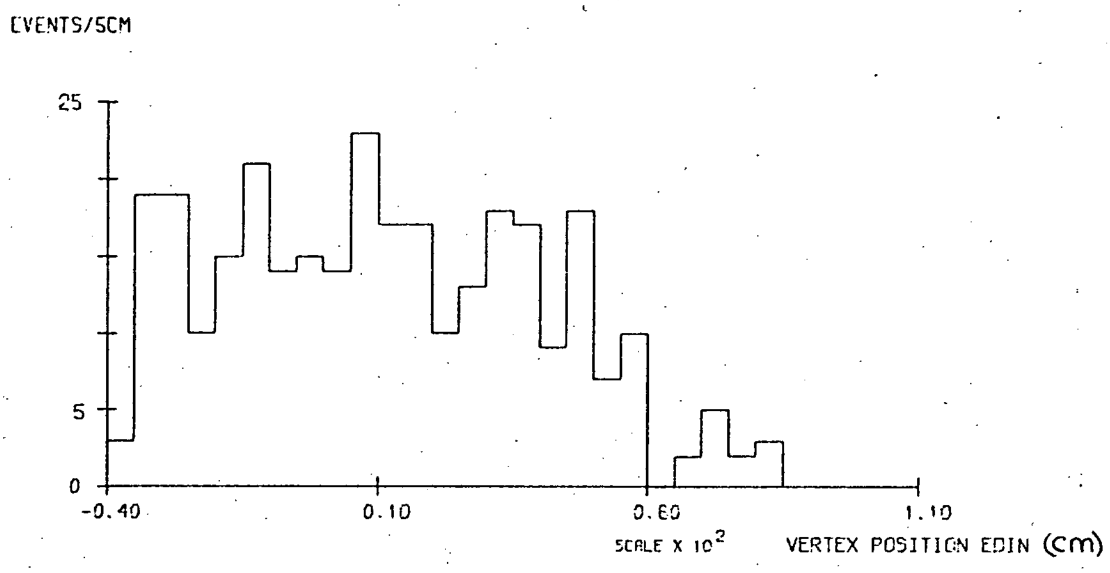

Vertex Positions - Edinburgh data.

FIG 3.2

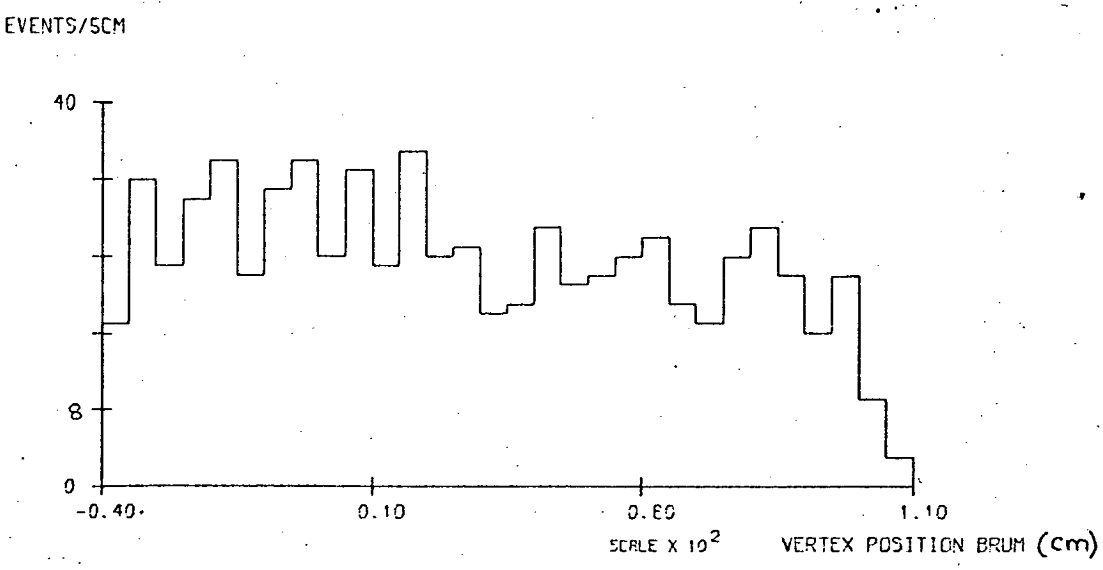

Vertex Positions - Birmingham Data.

The actual ratio $= \frac{509}{323} = 1.575$, which is in very good agreement.

The estimates of microbarn equivalent were thus assumed to be satisfactory.

3.3 Correction Factors

The number of reactions which actually take place has to be estimated from the number of events observed, by applying suitable correction factors. Losses occur in scanning, processing, neutral decays etc. These losses and their correction will now be considered.

3.3.1 Scanning Efficiency

The efficiency calculations are based on the assumption that all events of a given topology are equally likely to be seen by either scan, and that the chance of missing an event is purely random, i.e. independent of its position in the chamber.

Thus,

if scan 1 finds N_1 events,

and if scan 2 finds N_2 events,

of which both scans find N events,

then the efficiency of scan 1 $= E_1$, say $= \frac{N}{N_2}$,

and the efficiency of scan 2 $= E_2$, say $= \frac{N}{N_1}$,

so that the true number of events $= \frac{N_1 N_2}{N} = N_T$ say.

i.e. $N_T = \frac{(N_1' + N)(N_2' + N)}{N}$ where $N_1' = N_1 - N$

$$= N_1' + N_2' + N + \frac{N_1'N_2'}{N},$$

and the overall scanning efficiency $= E = \frac{N_s}{N_T}$

where $N_s = N_1' + N_2' + N$.

It is shown in Appendix 3A that the likely error on a single scan efficiency, E_1,

$$\text{is} \quad \frac{\Delta E_1}{E_1} = \sqrt{\frac{1 - E_1}{N}}$$

and that the likely error on the overall efficiency is

$$\frac{\Delta E}{E} = \sqrt{\frac{1 - E}{N}} \quad .$$

3.3.1.1 Edinburgh Sample Scanning Efficiencies

Only 2/9 of the Edinburgh film sample was double scanned.

Results

Topology	Estimated Scan Efficiency (Single)
202 (203)	76°/o ± 4°/o
402 (403)	69°/o ± 6°/o
211 (212)	69°/o ± 9°/o
411 (412)	62.5°/o ± 9°/o

3.3.1.2 Birmingham Sample Scanning Efficiencies

The Birmingham sample was completely double scanned and the efficiencies estimated as follows.

Topology	Efficiency
202 (203)	96.3°/o ± 3°/o
402 (403)	95.9°/o ± 3°/o
211 (212)	95.8°/o ± 3°/o
411 (412)	96.5°/o ± 3°/o

3.3.2 Processing Efficiency for the Edinburgh Sample

The Runs 4 and 5 film must be treated separately, since they have different 'Geometry' constants and were measured in separate batches. The first measure was followed by a re-measure of those events which had either failed or had been badly measured. A complete second measure of the rare events was carried out at a later stage.

The results of the processing, according to topology, are given in Table 3.1.

In the Run 4 film, 726 events were sent for measure, and in the Run 5 film, 1190 events were sent for measure.

3.3.2.1 Calculation for the Run 4 film

Let G be the efficiency for converting a scanned event into a successful Geometry record.

Let K be the kinematic efficiency for fitting a Geometry record to the correct reaction.

Then in the complete re-measure, if N is the true number of fittable events, from Table 3.1 one has,

$$79 = NGK .$$

TABLE 3.1

Number of fitted events on the DST after the different measures.

a) Run 4 film

Topology	202/3	211/2	402	411	Total
1st measure	30	10	17	5	62
Remeasure	8	3	6	1	18
2nd measure	40	14	19	6	79
Common	23	9	13	4	49
Total	55	18	29	8	110

b) Run 5 film

Topology	202/3	211/2	402	411	Total
1st measure	43	17	26	9	95
Remeasure	21	10	11	7	49
2nd measure	38	16	32	8	94
Common	25	10	18	7	60
Total	77	33	51	17	178

But of the 80 events fitted in the first measure and re-measure, 49 were common to the second measure,

$$\text{i.e.} \quad 49 = 80\,G\,K.$$

These two equations are sufficient to calculate N, viz.

$$N = 129 \pm 7 \quad \text{using} \quad \frac{\Delta N}{N} = \sqrt{\frac{1-E}{C}}$$

where C = number of common events

E = overall efficiency = 0.85.

2.3.2.2 Calculation for the Run 5 film

A similar calculation to the previous one leads to the estimated true number of fittable events in the Run 5 film as,

$$N = 227 \pm 14 \quad .$$

3.2.2.3 Results for processing Efficiency

Thus the estimated total number of events in Runs 4 and 5 film is

$$N_T = 356 \pm 16 \quad .$$

The measures just considered yielded a total of 288 events. A further 11 events were added later, having been re-measured on the Edinburgh measuring machine, Vanguard, giving a total of 299 out of an estimated 356 ± 16, which represents a total processing efficiency of

$$E = 84\% \pm 5\% \quad .$$

The Birmingham sample processing efficiency was estimated as

83°/o ± 4°/o.

3.3.2.4 Consistency of Processing in Edinburgh and Birmingham Laboratories

Six rolls of film which had been scanned and measured in Birmingham University, were scanned and measured in Edinburgh and the results compared. The scanning was very similar, and the same fits were obtained to the measured events in both cases, suggesting that the processing was similar in both laboratories.

3.3.3 Lifetime Losses

In Fig. 3. 3 is shown the theoretical spectrum of monochromatic Λ^0 hyperons produced at a point in the chamber, after a time, t. Those Λ^0's which decay in a time $t < t_1$, will be missed in the scanning, as they will not travel far enough in the chamber to make them recognisable as V^0's on the table. Those Λ^0's which decay in a time $t > t_2$ will be lost because they will decay near the edge of, or outside the chamber.

If the mean lifetime $= \tau$, then from the graph it is clear that the fraction of Λ^0's seen

$$= e^{-t_1/\tau} - e^{-t_2/\tau} = K, \text{ say.}$$

Therefore to each seen decay, one should attach a weight, $\frac{1}{K}$, where t_1 = time taken by the Λ^0 to travel a minimum visible distance, XX, and t_2 is the time taken by the Λ^0 to travel to one of the boundaries of the chamber.

FIG 3.3

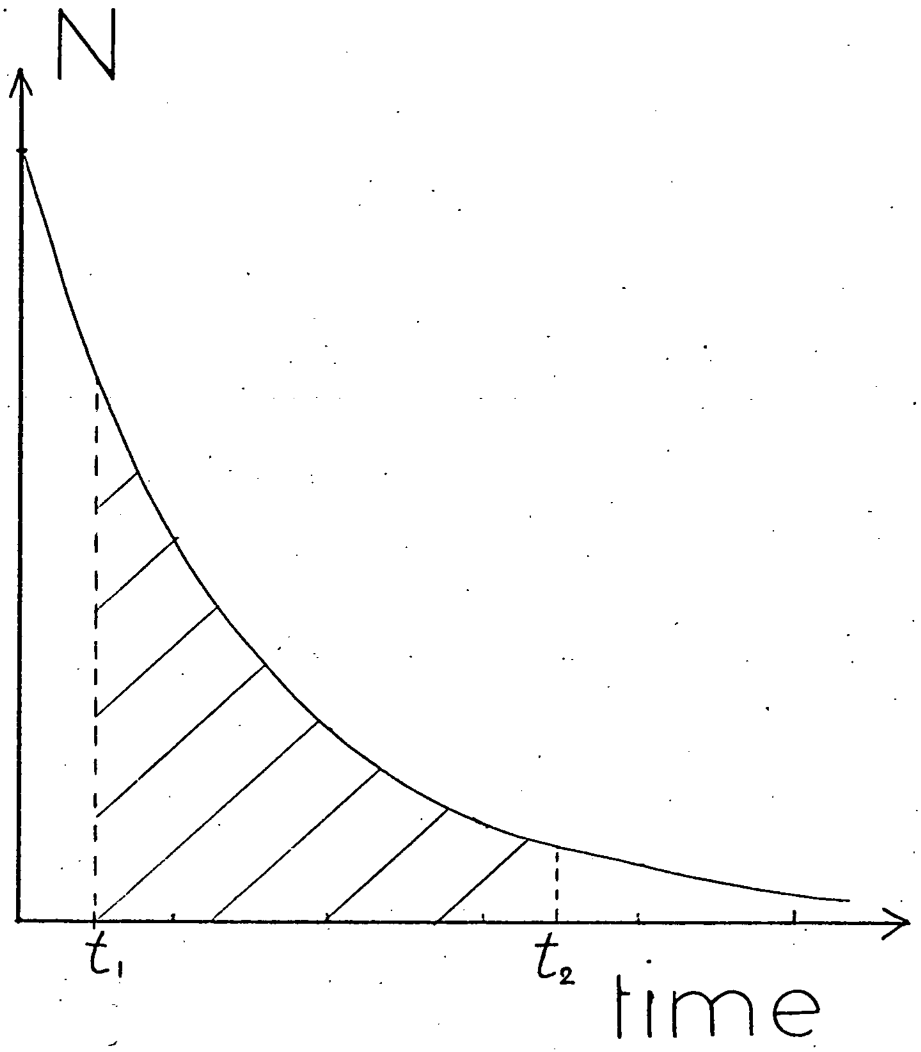

Theoretical decay curve.

TABLE 3.2

Effect of minimum cut-off length, XX, on weighted number of events. The second column gives the number of events where the decay length $>$ XX.

XX	N($>$ XX)	Weighted Number
0.0	958	
0.1	947	998
0.2	940	1021
0.3	930	1045
0.4	917	1064
0.5	887	1060
0.6	869	1070
0.7	848	1076
0.8	831	1087
0.9	802	1076
1.0	785	1087
1.5	677	1076
5.0	283	1060
10.0	99	1246

This also means that all events containing a decay length XX, must be rejected for purposes of cross-section calculation. Since the rare events contain at least two visible decays, each event is assigned at least two lifetime weights and the weighted numbers are therefore average values. The effect of choosing different minimum cut-off distances is shown in Table 3.2 where it may be seen that between $\ell = 0.5$ cm and $\ell = 5.0$ cm, the weighted number of events varies by less than 1.5°/o. To avoid losing too many events, and thus decreasing the available statistics, the cut-off value, XX, was set at 0.3 cm, giving an average weight of $\sim$ 11°/o.

The author wrote his own program to perform these calculations since the standard program did not operate correctly on some rare events. The lifetime weight was written into word 9 on the DST.

3.3.4 Losses due to small-angle charged decays

The Σ^+ hyperon has two main modes of decay,

$\Sigma^+ \longrightarrow p\,\pi^0$ (1) 51.6%

$\pm$ 0.7°/o .

$\Sigma^+ \longrightarrow n\,\pi^+$ (2) 48.4%

Since the speed of the proton in the C.M.S. of the decaying Σ^+ is low, the direction of the emitted proton in the lab. will not differ much from that of the Σ^+, giving rise to small decay angles, and a consequent loss of events.

Fig. 3.4 shows the projected decay angles, ϕ, from decay (1) above, where it may be seen that the majority of events lie in $-20^\circ \lesssim \phi \lesssim 20^\circ$.

FIG 3.4

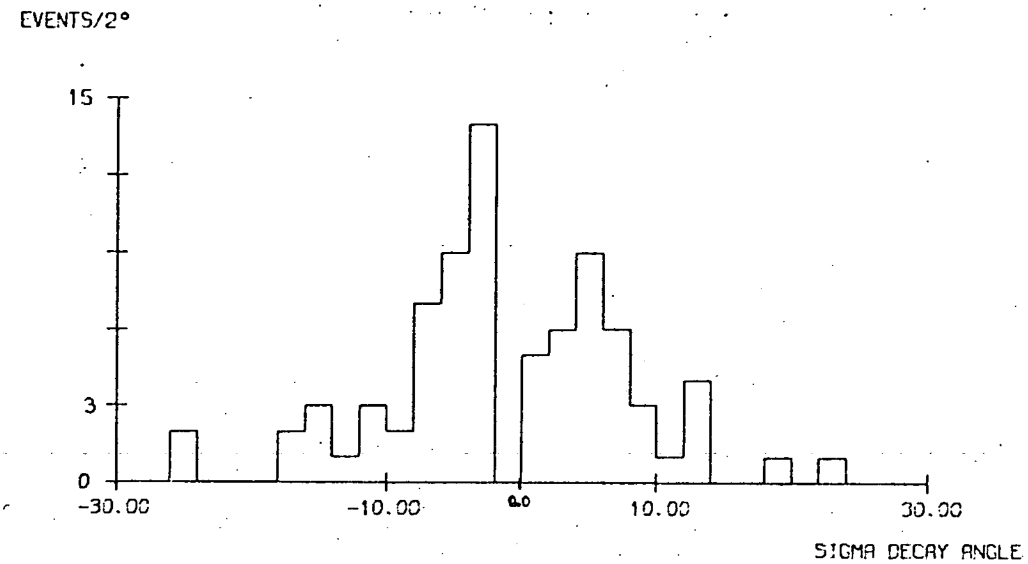

Projected decay angles for the decay, $\Sigma^+ \rightarrow p\pi^0$.

FIG 3.5

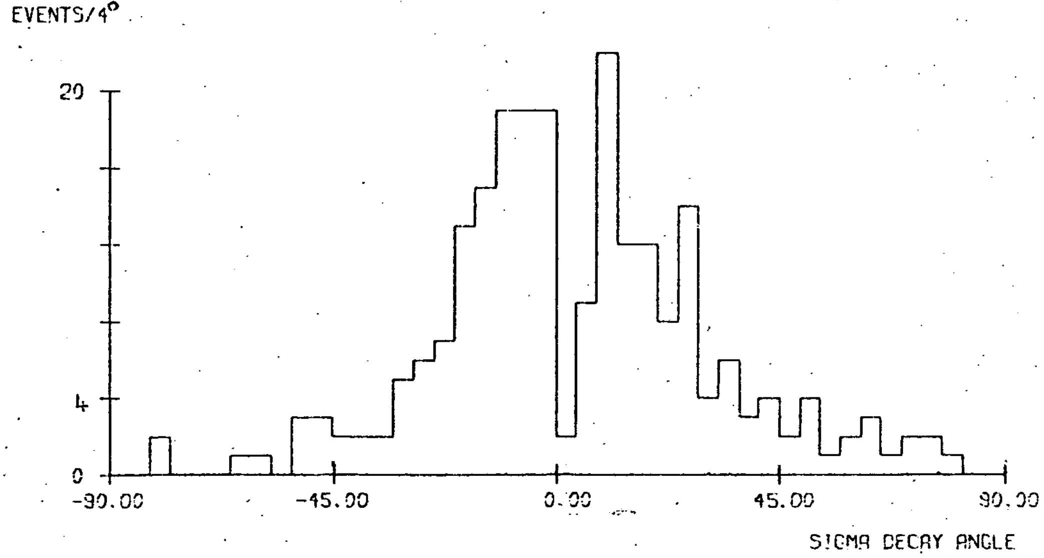

Projected decay angles for the decay, $\Sigma^\pm \longrightarrow n\pi^\pm$

The projected decay angle is defined as

$$\phi = \phi_P - \phi_D$$

where ϕ_P = azimuthal angle of the decaying sigma hyperon,
and ϕ_D = azimuthal angle of the decay product.

If this angle, $\phi < 0^\circ$, then the decay is of the form

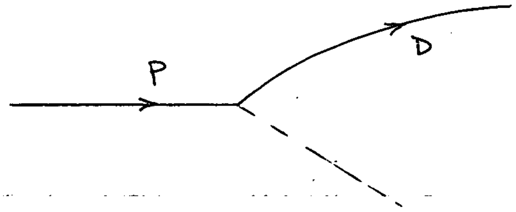

and if this angle, $\phi > 0^\circ$, the decay is of the form

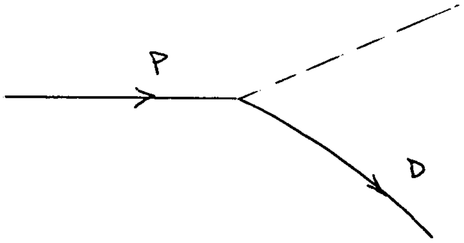

Fig. 3.5 shows the projected decay angles for decay (2), as well as those for the decay,

$$\Sigma^- \longrightarrow n \pi^- \quad . \qquad (3)$$

It is seen that the angles are in general much larger, stretching out to ± 75°.

The losses which occur can be appreciated by an examination of the momentum spectrum of the parent Σ-hyperons in decays (1) and (2), shown in Figs. 3.6 and 3.7 respectively. Not only are there almost twice as many detected decays of type (2) but the momentum spectrum for the protonic decay mode ceases at a sigma momentum of 3.7 GeV/c, whereas the other extends past 5 GeV/c.

Although one does not know the expected number of projected decay angles in the range $-4^\circ \lesssim \phi \lesssim 4^\circ$, it is clear from

FIG 3.6

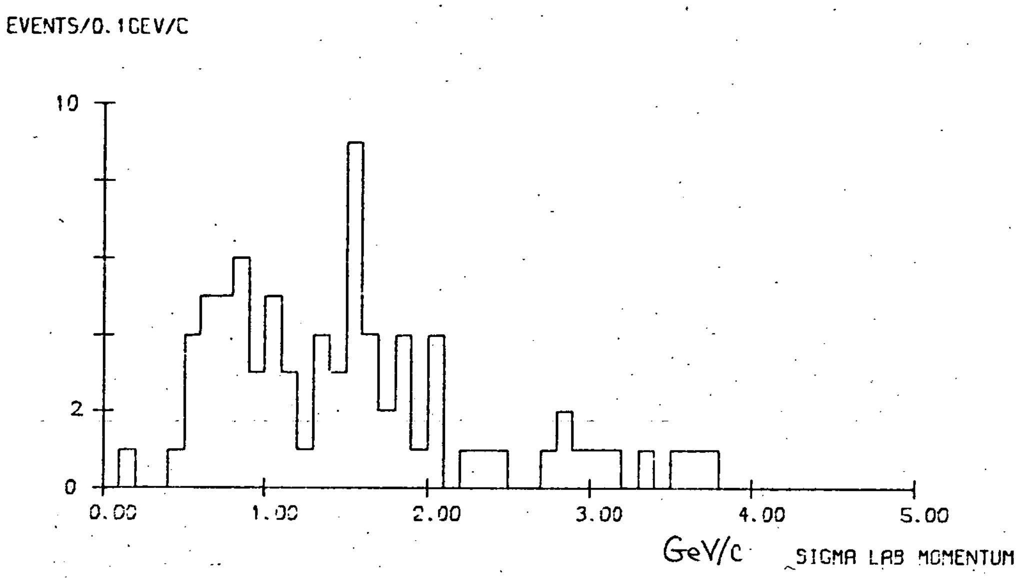

Laboratory momentum of sigma-hyperon giving,

$\Sigma^+ \rightarrow P\pi^o$.

FIG 3.7

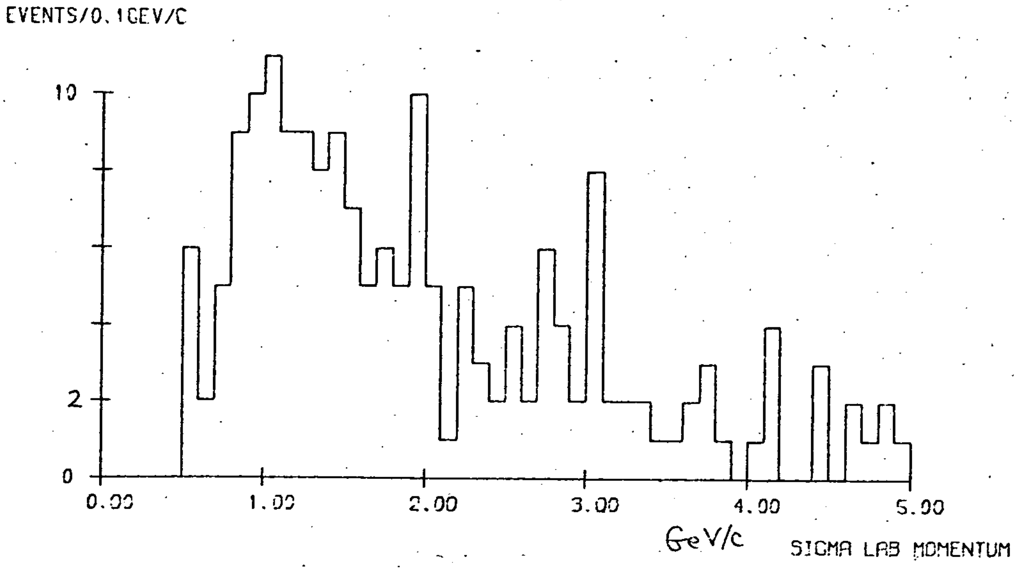

Laboratory momentum of sigma-hyperon giving,

$\Sigma^+ \rightarrow n\pi^+$.

Figs. 3. 4 and 3. 5 that both pionic and protonic decay modes suffer from losses in this region, and these are obviously more important for the latter modes, for reasons given above. (One other high energy experiment(1) performed at 6 GeV/c incident momentum, also found that this effect became important at an angle of approximately 4°.)

To examine this further, random Σ-pion and Σ-proton decays at sigma momentum in the range, $0 \longrightarrow 5$ GeV/c in 100 MeV/c intervals, were generated, and the projected decay angle for each was calculated. These were plotted as percentage of decays with $|\phi| < 4^{\circ}$, versus momentum of the sigma, separately for pionic and protonic decay modes. The result is shown in Fig. 3. 8 .

It is clear from this figure that for a sigma momentum >3.4 GeV/c, no protonic decay can have a projected angle, $>4^{\circ}$. The percentage of decay angles $< 4^{\circ}$ for the pionic decay mode can be represented from Fig. 3 .8 , approximately as

$$y = 7P + 9$$

where P = sigma momentum, i.e. at 1 GeV/c Σ -momentum, the percentage is 16°/o.

For the Σ -proton decays, the percentage is (to $\sim$ 3°/o)

$$y = 40\sqrt{P} + 5P^{3/2} .$$

If the number of events were large, one could remove from the sample, all events having a projected angle $< 4^{\circ}$ say, and correct the remainder using the equations above. i.e. the weighting factor for Σ -pion events would be

FIG 3.8

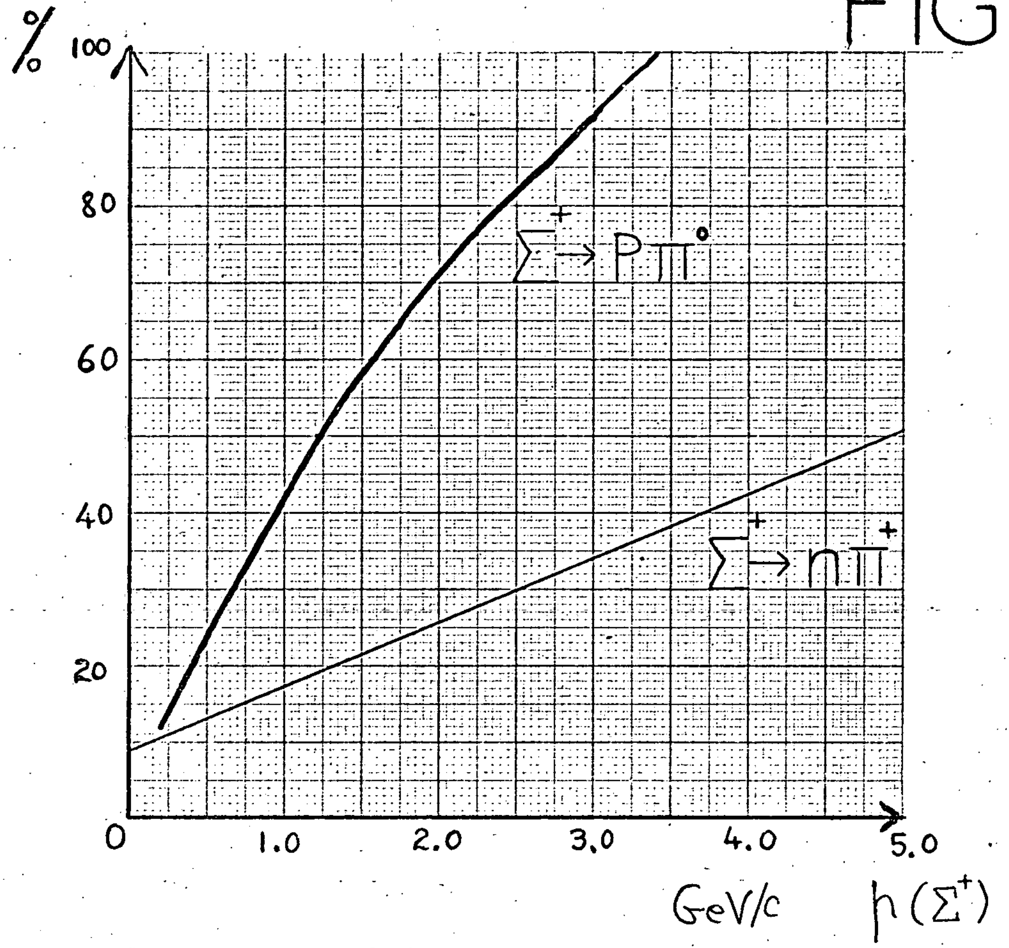

Percentage of decays giving a projected angle ≤ 4°.

FIG 3.9

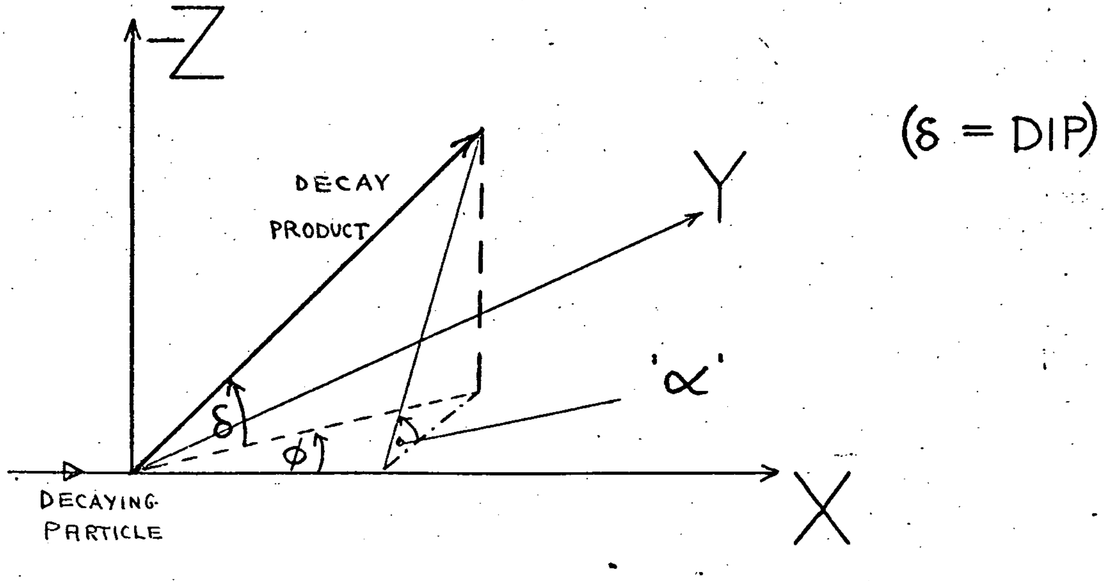

Definition of Camera azimuthal angle 'α'.

$$W = \frac{100}{(91 - 7P)} \approx \frac{1}{1 - 0.1 \times P} .$$

(This latter factor was the one used in the published results.)

The author removed from the sample, all Σ-events with a projected decay angle $< 4^\circ$ and weighted the remaining events using the above factors. The results of this procedure were poor in that it did not improve the disagreement between cross-sections as calculated from the Σ-proton and Σ-pion decay modes. It is felt therefore that the best estimate of cross-section for events containing Σ-decays would be obtained by considering only the Σ-pion decay modes, weighted as above.

3.3.5 Losses due to Camera Azimuthal Angle

In addition to losses due to the smallness of the decay angle, all decays will suffer a loss when the decay plane is very nearly parallel to the camera axis, so that the projected angle is small.

To investigate this loss, it is useful to define the "camera azimuthal angle" α, as shown in Fig. 3. 9 .

The beam enters along the X-axis as shown, and the chamber set of axes is left-handed, i.e. $X \wedge Y = -Z$. The cameras point along the positive Z-axis. Dip angles, δ, are positive in positive z-directions, and the chamber azimuthal angle, ϕ, is anti-clockwise as seen by the cameras, with the X-axes at $\phi = 0^\circ$.

The camera azimuthal angle, α, is anti-clockwise as seen from positive X, and $\alpha = 0^\circ$ in the XY plane.

FIG 3.10

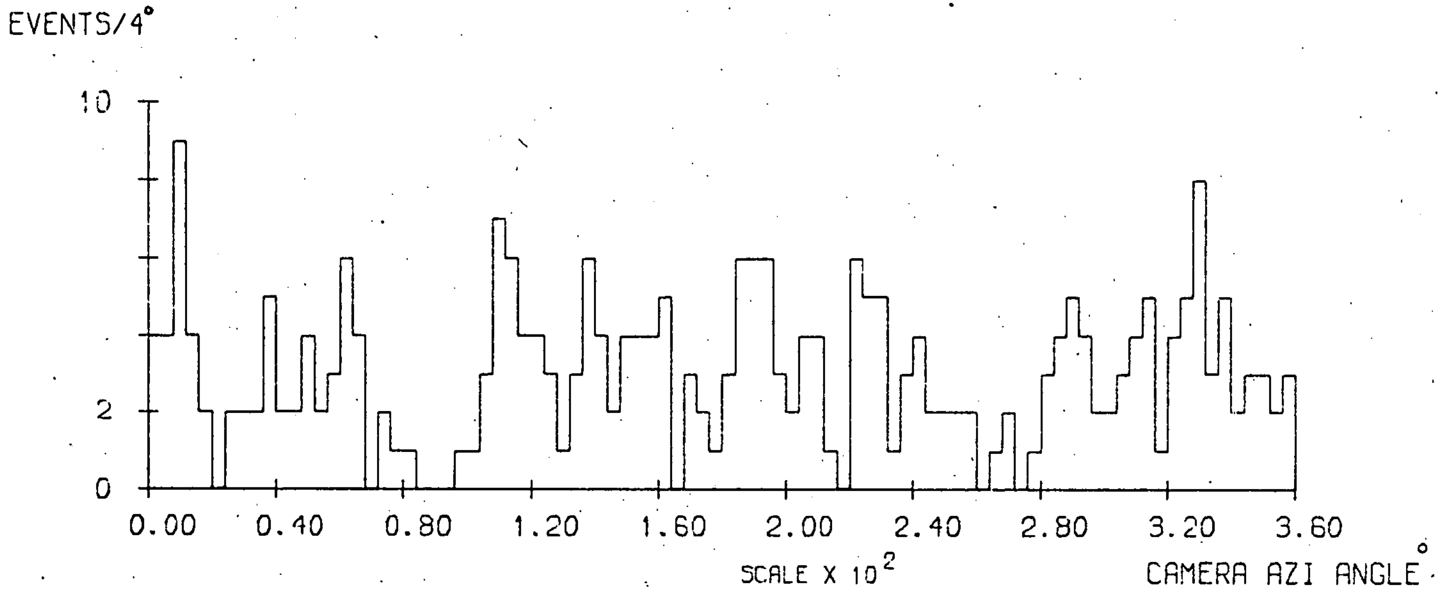

Camera azimuthal angle for all Σ^+ decays.

Fig. 3.10 shows the distribution in α for charged sigma decays, where there is an obvious gap in the distribution for $64^\circ \lesssim \alpha \lesssim 104^\circ$, corresponding to decays in which the decay product rises towards the camera, almost collinearly with the decaying track. The fact that the gap is not centred around $\alpha = 90^\circ$ may be explained by the fact that α is calculated for a camera which has its axis perpendicular to the beam plane, whereas camera TOP 1, whose view is usually examined first, is about 6° off the perpendicular, reducing the camera azimuthal angle.

The loss seems to be smaller for dipping tracks, e.g. examining the distribution around $\alpha = 270^\circ$, the density of events is similar to other regions of the plot, excluding that part just considered.

Outside the region $64^\circ \lesssim \alpha \lesssim 104^\circ$, there are 275 events in the remaining 320°, which suggests that there has been a loss of approximately 30 events, i.e. about 10°/o of decays are lost by virtue of their camera azimuthal angle.

3.3.6 Events lost due to Neutral Decay Modes.

The Λ^0 hyperon has two main modes of decay, viz.

$\Lambda^0 \longrightarrow p\,\pi^-$ 64°/o

$\Lambda^0 \longrightarrow n\,\pi^0$ 36°

The K^0_s meson has also two main modes of decay, viz.

$K^0_s \longrightarrow \pi^+\,\pi^-$ 68.7°/o

$K^0_s \longrightarrow \pi^0\,\pi^0$ 31.3°/o .

In addition, any K^0 produced, may decay either as K^0_s, with

a lifetime of 0.86×10^{-10}s, or as a K^o_L, with a lifetime 5×10^{-8}s, so that the K^o_L mode will rarely be observed. i.e. If "n" Λ^o-decays are seen, the number produced is assumed to be $\frac{n}{0.64} = 1.53n$.
Similarly, if "n" K^o_s-decays are seen, the number of K^o-mesons produced $= \frac{2n}{0.687} = 2.92n$.

When a reaction involves the production of three V^o particles, there are several probabilities to account for materialisation of two out of three of the V^o's, e.g. in the reaction,

$$K^+P \longrightarrow \pi^+\pi^+K^oK^o\Lambda^o,$$

there are 24 different configurations of the three neutral particles, including decays which take place outside the chamber, and only 6 of these will be scanned as rare events, giving the three channels

$$K^+P \longrightarrow \pi^+\pi^+K^oK^o(\Lambda^o)$$

$$K^+P \longrightarrow \pi^+\pi^+K^o\Lambda^o(K^o)$$

$$K^+P \longrightarrow \pi^+\pi^+K^oK^o\Lambda^o$$

If suitable correction factors are applied to each of these channels, this information can be used to arrive at a better estimate of the cross-section for the initial reaction. All weighting procedures adopted assume that any event will be fitted to the highest topology, e.g. that a genuine 212-type of event will not be fitted to a 211-type of hypothesis.

Consider the reaction which is observed as,

$$K^+P \longrightarrow \pi^+\pi^+K^o\Lambda^o(K^o) \quad .$$

Let x be the probability of one K^0 decaying outside the chamber,

Let x' be the probability of the other K^0 decaying outside the chamber.

Let y be the probability of the Λ^0 decaying outside the chamber.

Then in a sample of N reactions with the same configuration, the fraction one might expect to see (ignoring scanning and processing losses) is

$$f = \underbrace{\tfrac{2}{3}(1-y)}_{(i)} \times \underbrace{2 \times \tfrac{2}{3} \times (1-x) \times \tfrac{1}{2}}_{(ii)} \times \left\{ \underbrace{\tfrac{1}{2} + \tfrac{1}{2} \times \tfrac{1}{3} + \tfrac{1}{2}\,\tfrac{2}{3}\,x'}_{(iii)} \right\}$$

$$= \frac{4}{27}(1-y)(1-x)(2+x')$$

where (i) represents the fraction of seen Λ^0-hyperons

(ii) represents the fraction of seen K^0-mesons

(iii) represents the unseen K^0 meson.

Then $^1/f$ represents the weight attached to such an event. Similar factors were calculated for the other reactions observed and placed in word (9) on the DST record.

If the hypothesis does not involve an unseen V^0, the weights are straightforward, e.g. for the hypothesis,

$$K^+P \longrightarrow K^+\pi^+K^0\Lambda^0$$

the weight for the unseens is $2 \times 1.46 \times 1.53$.

Hypotheses involving a $K^0\,\overline{K}^0$ pair pose special problems, and the $K^0\overline{K}^0$ system will now be discussed.

3.3.7 The $K^o\,\overline{K}^o$ System

There are two neutral K-mesons, the K^o with strangeness $S = +1$, and the $\overline{K}^o$ with strangeness $= -1$. Both particles may decay via the weak interaction to $\pi^+\pi^-$, and since their decay products are indistinguishable, the states $|K^o\rangle$ and $|\overline{K}^o\rangle$ are coupled through the weak interaction. This means that the above states which are eigenstates of strangeness, are not appropriate for a study of K^o-decay, in which strangeness is not conserved.

However, in general, weak interactions do exhibit CP invariance and it would be more appropriate to choose eigenstates of CP to represent K^o-decay. Since the operators CP and S do not commute, the CP eigenstates will be ambiguous with respect to strangeness. They are defined by,

$$CP\,|K_1^o\rangle = |K_1^o\rangle$$

$$CP\,|K_2^o\rangle = -\,|K_2^o\rangle$$

where

$$|K_1^o\rangle = \frac{1}{\sqrt{2}}\left(|K^o\rangle + |\overline{K}^o\rangle\right)$$

$$|K_2^o\rangle = \frac{1}{\sqrt{2}}\left(|K^o\rangle - |\overline{K}^o\rangle\right) .$$

Although the K^o and $\overline{K}^o$ cannot be distinguished by their decay products, the K_1^o and K_2^o can, since final pion states can have different CP values, viz.

$$K_1^o \longrightarrow 2\pi \qquad CP = +1 \qquad \text{high Q-value}$$

$$K_2^o \longrightarrow 3\pi \qquad CP = -1 \qquad \text{low Q-value.}$$

Thus the K_1^o with a high Q-value should have a much shorter lifetime than the K_2^o, and in fact the mean lifetimes are found to be;

$$\tau(K_1^o) = 0.862 \times 10^{-10} s$$
$$\tau(K_2^o) = 5.172 \times 10^{-8}\ s\ .$$

For this reason, the K_1^o is generally known as the K_S^o (short) and the K_2^o as the K_L^o (long).

(It was later shown that the K_2^o may in fact decay to two pions, with a branching ratio $\sim 10^{-3}$, which represents a small CP violation effect.)

For strong interactions, in which K^o or $\overline{K}^o$ are produced, one may consider such states to be a mixture of the states K_S^o and K_L^o .

If one has two particles K^o and $\overline{K}^o$ in space states A and B respectively, with angular momentum, ℓ, one may write, instead of $K^o\,\overline{K}^o$,

$$(K_A^o\,\overline{K}_B^o + K_B^o\,\overline{K}_A^o)/2 \qquad \text{for even } \ell \text{ values.}$$

$$(K_A^o\,\overline{K}_B^o - K_B^o\,\overline{K}_A^o)/2 \qquad \text{for odd } \ell \text{ values.}$$

i.e. for even ℓ values, using CP eigenstates,

$$K^o\,\overline{K}^o = \frac{1}{2}\left\{\frac{1}{\sqrt{2}}\left(A_{K_S^o} + A_{K_L^o}\right) \times \frac{1}{\sqrt{2}}\left(B_{K_S^o} - B_{K_L^o}\right) + \right.$$
$$\left. + \frac{1}{\sqrt{2}}\left(B_{K_S^o} + B_{K_L^o}\right) \times \frac{1}{\sqrt{2}}\left(A_{K_S^o} - A_{K_L^o}\right)\right\}$$
$$= \tfrac{1}{2}\left(A_{K_S^o}\,B_{K_S^o} - A_{K_L^o}\,B_{K_L^o}\right)$$

i.e. both "short" or hoth "long" .

For odd ℓ values, one finds

$$K^o \overline{K}^o = \tfrac{1}{2}\left({}^A K_L^o \; {}^B K_S^o - {}^A K_S^o \; {}^B K_L^o\right)$$

i.e. one "short" and one "long".

This means that if both K^o and $\overline{K}^o$ are seen, i.e. "short", they must have been produced in a state of even angular momentum. However, if either K^o or $\overline{K}^o$ is missing, it is not possible to say anything about the angular momentum states.

For the K^oK^o system, the CP eigenstate representation is more straightforward. The system must be symmetric under interchange of particles, i.e. one can represent K^oK^o as

$$\begin{aligned} K_A{}^o \, K_B{}^o &= ({}^A K_S^o + {}^A K_L^o)\,({}^B K_S^o + {}^B K_L^o)/2 \\ &= \frac{{}^A K_S^o \; {}^B K_S^o}{2} + \frac{{}^A K_S^o \; {}^B K_L^o}{2} + \frac{{}^B K_S^o \; {}^A K_L^o}{2} + \frac{{}^A K_L^o \; {}^B K_L^o}{2} . \end{aligned}$$

That is, $^1/_4$ of all K^oK^o pairs produced, will decay by the $K_S^o \, K_S^o$ mode.

3.3.8 Estimate of Loss due to Non-contrained Production Fits

If a reaction takes place in which an unseen neutral is produced at the interaction vertex, and one of the outgoing charged tracks interacts in a short distance, so that its momentum is unmeasurable, then there will be four unknowns at the primary vertex, i.e. a zero-constraint fit, which is not acceptable.

To estimate the losses involved, a count was made of the numbers of $\pi^{\pm}$, $K^{\pm}$, P involved in the different topologies, together with their average momenta. The minimum measurable sagitta was taken as 1 mm, and the lengths required to give a sagitta of 1 mm were calculated for the various momenta.

Using this information, together with the total cross-sections, estimates were made of the likely number of interactions which would take place. The losses were estimated to be as follows (approximately)

Topology	Loss
202	4°/o ± 1°/o
211	3°/o ± 1°/o
402	8°/o ± 2°/o
411	7°/o ± 3°/o

3.3.9 Correction for loss of events in Kinematic Fitting

A cut-off value of 1°/o was imposed on the χ^2 probability for the Kinematic fit. Figure 3.11 shows the distribution of χ^2-probability, in bins of 5°/o, for 452 fits (representing 321 actual events). There is a small "bulge" near the low probability end of the distribution but otherwise it is acceptably flat.

Fig. 3.12 shows the distribution of probabilities in 1°/o bins from 0% to 10°/o, and it appears that were it not for the 1°/o cut, the expected content of the first bin would be $\sim$ 15 fits, representing a loss of approximately 10 events, or 3°/o of the total number of events.

3.4 Combination of Cross-sections from the Two Samples

The problem arose, of combining the cross-sections calculated from the two batches of film, i.e. the Edinburgh and Birmingham samples. A program called "FT" was written by the

FIG 3.11

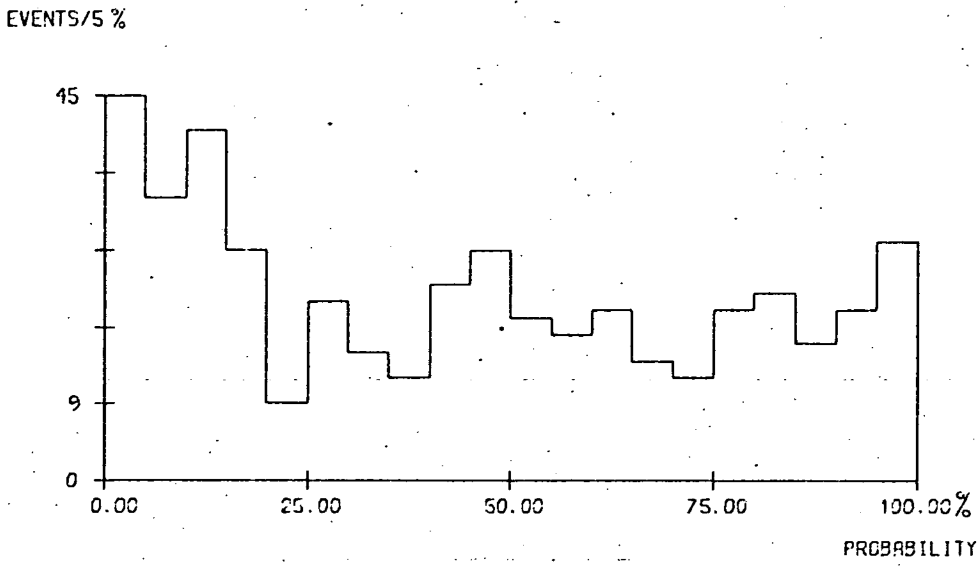

Chi-squared probability of fit: 452 fits.

FIG 3.12

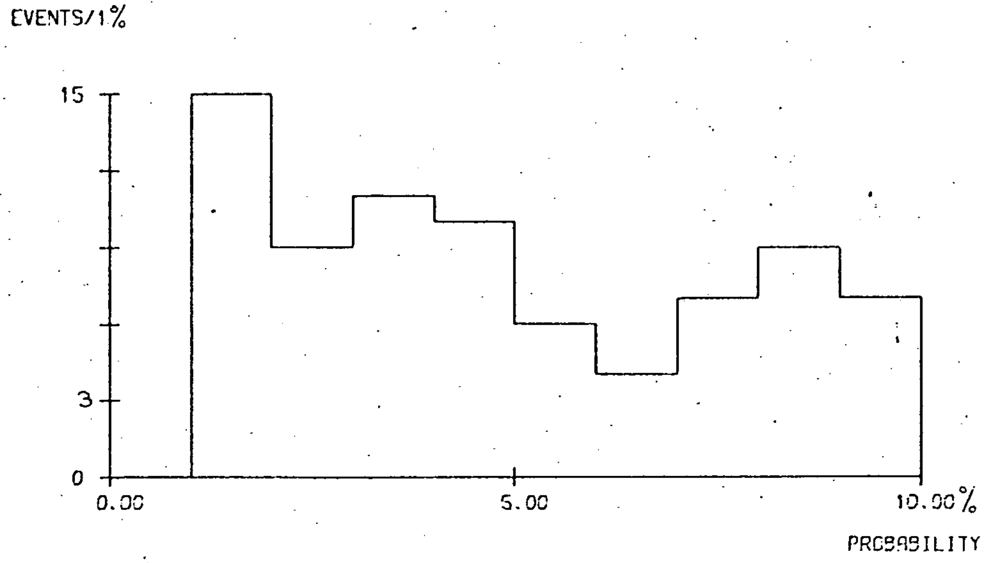

The first ten per cent of Fig. 3.11.

author to calculate a weighted mean, together with its associated error. This method assumes that the two estimates are consistent, i.e. that the difference between them is not significant. "FT" also calculates a chi-squared value based on the two estimates, the average value of which should be = 1.0. In fact the average value of the χ^2 values based on 40 calculations = 0.994, which is encouraging as an indication of realistic errors.

If for any calculated value, $\chi^2 > 1.0$, the error on the weighted mean was increased by $\sqrt{\chi^2}$, following the method adopted by the Particle Data Group$^{(2)}$. The distribution of the χ^2 values is shown in Fig. 3.13 together with the theoretical distribution, normalised to 40 events. The agreement is good.

The χ^2 test does not reveal whether the cross-sections calculated from one sample, are consistently higher, or lower than those calculated from the sample. For this reason, "FT" also calculates a normalised stretch function for each reaction, where the stretch, S, is defined, for the Birmingham sample as

$$S_B = \frac{\sigma - \sigma_B}{\sqrt{(\partial_B^2 - \partial^2)}} = - S_E$$

where σ = weighted mean value of cross-section.

σ_B = cross-section calculated from Birmingham sample

∂ = error on weighted mean.

∂_B = error on Birmingham sample cross-section.

S_E = Edinburgh stretch function.

Such a function, S, is expected to be normally distributed$^{(3)}$ about 0.0, with standard deviation 1.0 and the distribution of

FIG 3.13

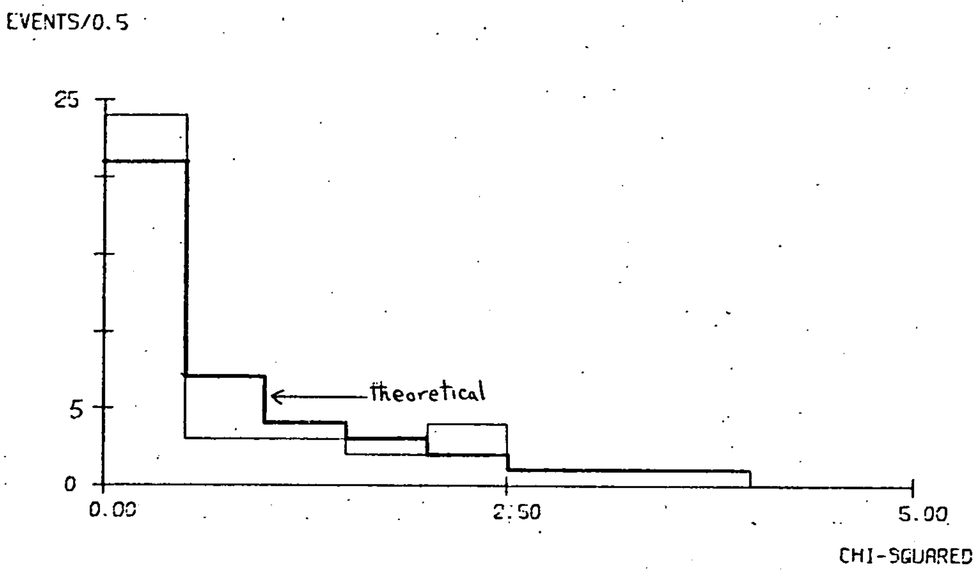

Chi-squared distribution for cross-section calculations.

FIG 3.14

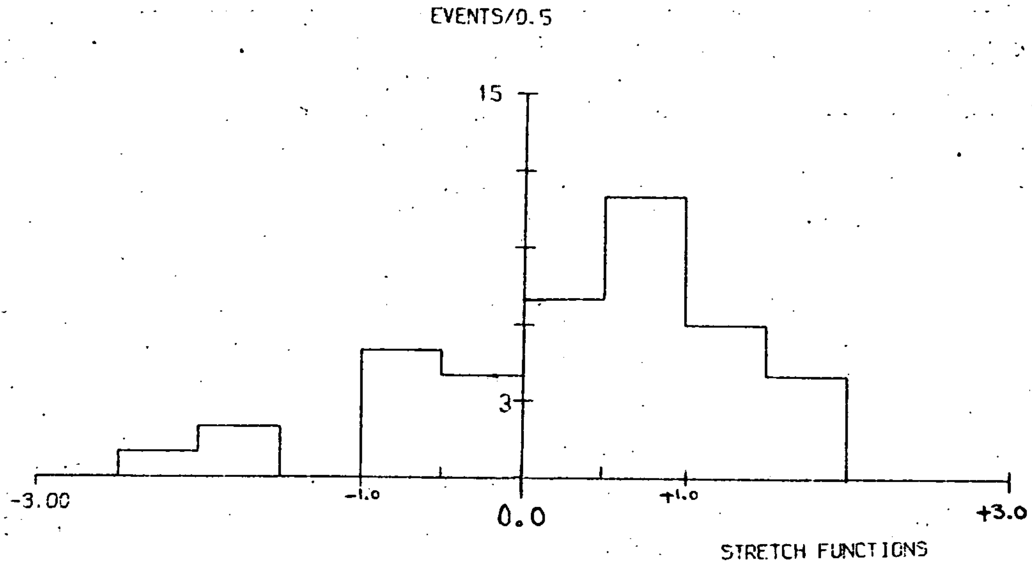

Stretch-functions for cross-section calculations.

of S_B is shown in Fig. 3.14. There is an excess of 16 events on the positive X-axis, meaning that, overall, the cross-sections calculated for the Birmingham sample are smaller than those calculated from the Edinburgh sample. However, bearing in mind the ambiguities present, the agreement between the samples is very encouraging. All calculated cross-sections together with their errors are listed in Appendix 3B.

3.5 Combination of Cross-sections of Mutually Ambiguous Reactions

Many ambiguous interpretations of an event arose from $K - \pi$ ambiguities, e.g. 27 events were ambiguous between

$$K^+p \longrightarrow K^+\pi^+\pi^+\pi^-K^o\Lambda^o(\pi^o)$$

and $$K^+p \longrightarrow \pi^+\pi^+\pi^+\pi^-K^o\Lambda^o(K^o) \quad .$$

Similarly, 32 events were ambiguous between,

$$K^+p \longrightarrow \Sigma^+K^+K^o(\pi^o)$$

and $$K^+p \longrightarrow \Sigma^+\pi^+K^o(K^o).$$

In calculating the cross-sections for reactions such as the above, the method used was to allow a weight of 0.5 per event, to each reaction, although no attempt was made to estimate the likely error arising from this method.

In the case of triple ambiguities, the weight was 0.33, e.g. 10 events gave equally acceptable fits to all of

$$K^+P \longrightarrow K^+\pi^+K^o\,\bar{K}^o\,(n)$$

$$K^+P \longrightarrow \pi^+\pi^+K^oK^o(\Lambda^o)$$

$$K^+P \longrightarrow \pi^+\pi^+K^oK^o(\Sigma^o)\quad .$$

It was later decided that it would be better to sum the cross-sections for ambiguous reactions, if possible, since this would give a more truthful picture than any arbitrary weighting method. Since the Birmingham data had a different microbarn equivalent, and different correction factors, this also necessitated treating the two samples separately.

Obtaining this information on cross-ambiguities from 1500 fits on a DST is a complicated process, and a special program called "JINGS" was written by the author to list each reaction with its number of unique fits (which includes track-swaps) followed by an ambiguity matrix. A sample output is as follows:

```
"Hypothesis 202093

                    Number of unique fits    =   11

                    Number of competing      =   2
                       hypotheses

 Ambiguity array                    202203     202103
                                       5          3     202203

                                       0          0     202103"
```

This indicates that for hypothesis number 202093, viz.

$$K\ P \longrightarrow \pi^+P\ K^o\bar{K}^o(K^o)$$

there are 11 unique fits.

There are 5 single ambiguities with hypothesis number 20203, viz.

$$K^+p \longrightarrow K^+pK^o\overline{K}^o(\pi^o)$$

and 3 double ambiguities with 202203 and 202103 where the latter represents,

$$K^+p \longrightarrow K^+\pi^+K^o\overline{K}^o(n) \ .$$

This is more clearly expressed as a Venn diagram, as shown in Fig. 3.15.

Sometimes as many as ten or more different reactions were involved in collecting all the information on ambiguities for a single channel, although only two or three of them formed the dominant ambiguity, e.g. for the hypothesis,

$$K^+p \longrightarrow K^+\pi^+\pi^+\pi^-K^o\Lambda^o(\pi^o)$$

there were 9 other hypotheses at some time ambiguous with this one, but 8 of these 9 had no more than two ambiguous fits, and the ninth had 19 ambiguities, this being $K^+p \longrightarrow \pi^+\pi^+\pi^+\pi^-K^o\,\Lambda^o(K^o)$. There were 28 unique fits to the original hypothesis.

Fig. 3.16 shows the ambiguities found in the Birmingham 202-type hypotheses. The K^oK^o or $K^o\overline{K}^o$ events, and the Λ^oK^o events form two distinct sets, and there seems no simple way of treating several hypotheses together, to calculate a combined cross-section.

Fig. 3.17 shows the equivalent sets for the Edinburgh sample. These ambiguities are simpler, probably because there are fewer events.

Fig. 3.18 illustrates the ambiguities encountered in dealing with seen Σ^o decays, for 202-type hypotheses, and Fig. 3.19 is the equivalent diagram for the 402-type hypotheses.

FIG 3.15

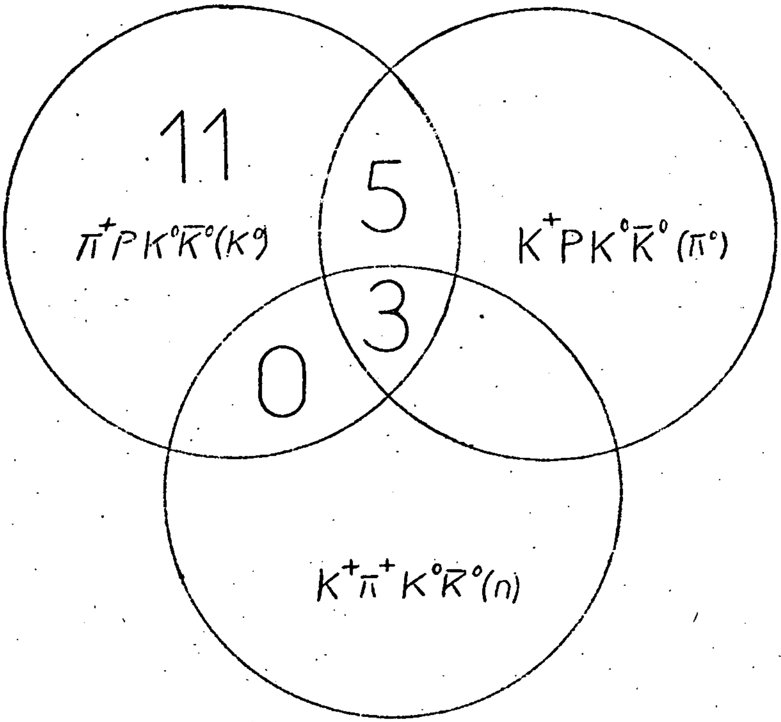

Venn diagram of ambiguities for the channel,

$K^+P \rightarrow \pi^+P\ K^0\ \bar{K}^0(K^0)$.

FIG 3.16

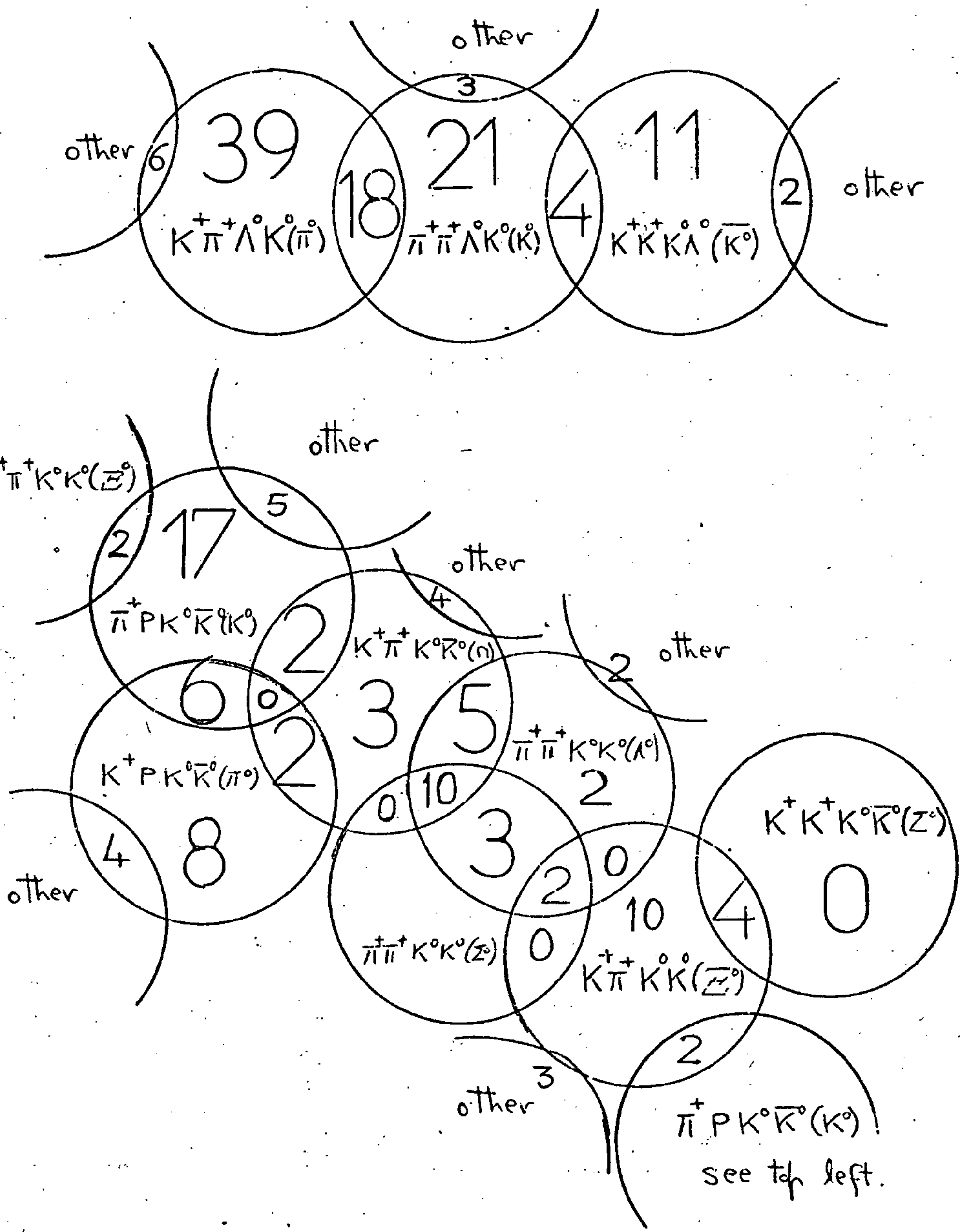

Ambiguities: Topology 202

Birmingham Data.

FIG 3.17

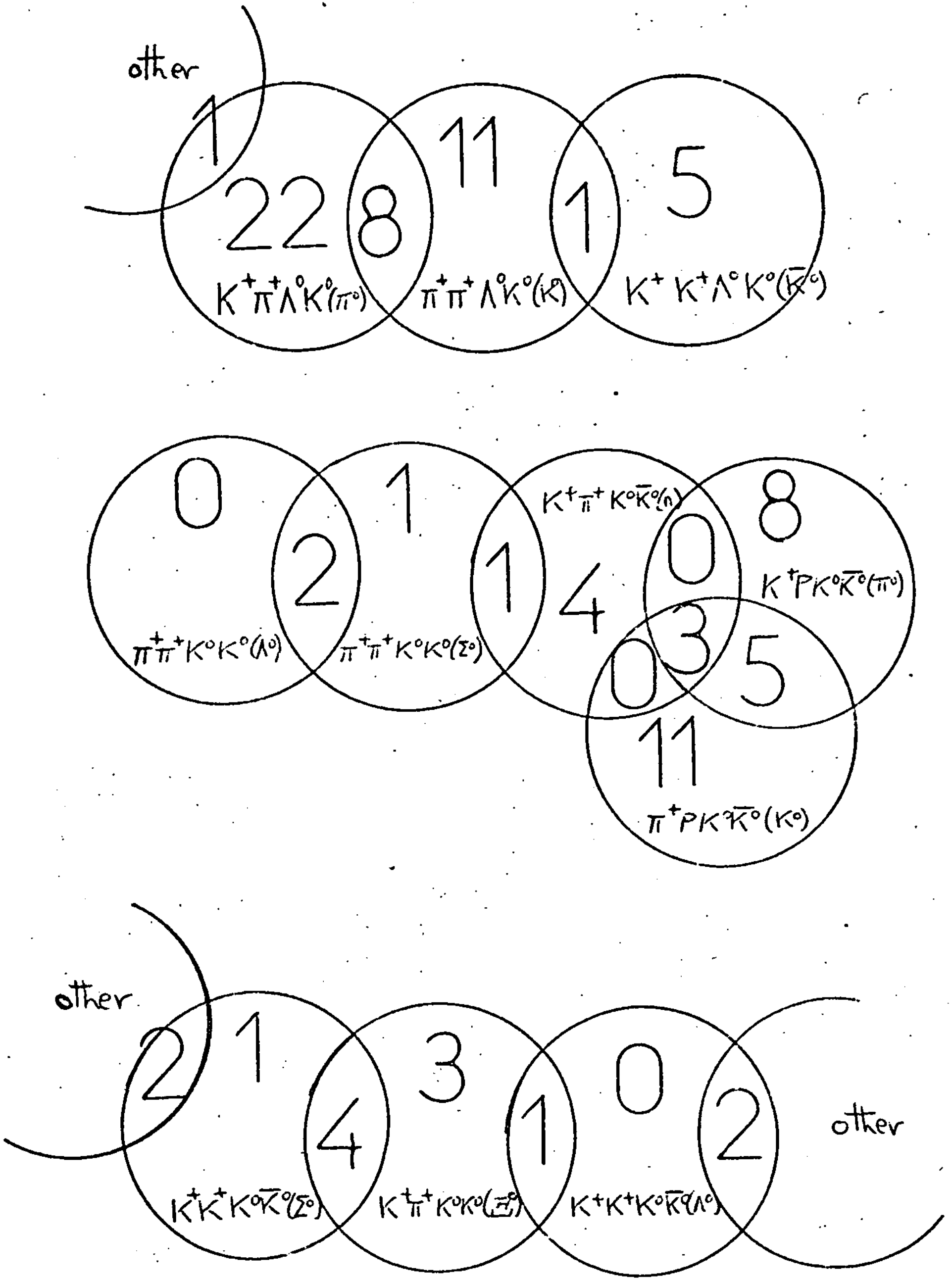

Ambiguities: Topology 202

Edinburgh Data.

FIG 3.18

The Λ^0/Σ^0 Ambiguities: Topology 202.

a) Edinburgh Data

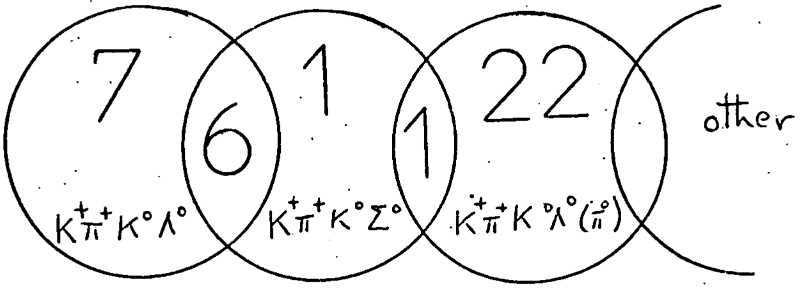

b) Birmingham Data

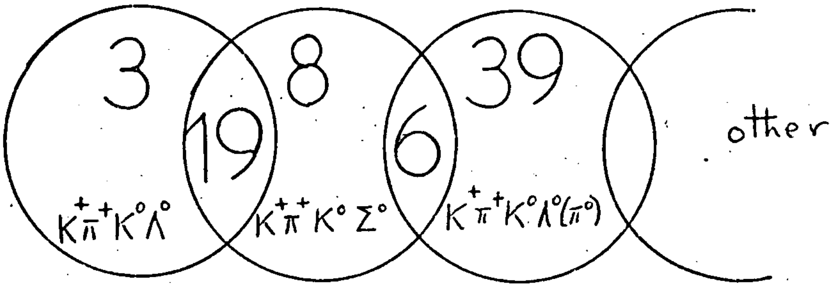

FIG3.19

The $\Lambda^\circ/\Sigma^\circ$ Ambiguities: Topology 402.

a) Edinburgh Data

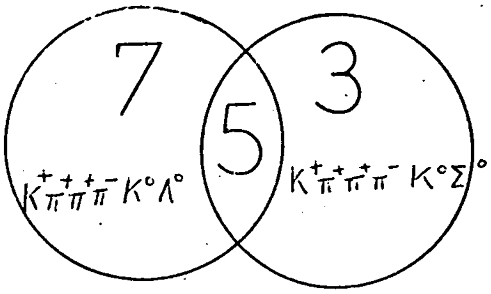

b) Birmingham Data

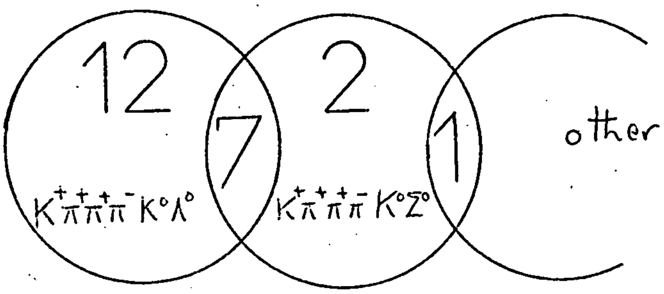

FIG 3.20

Ambiguities: Topology 402

a) Edinburgh Data

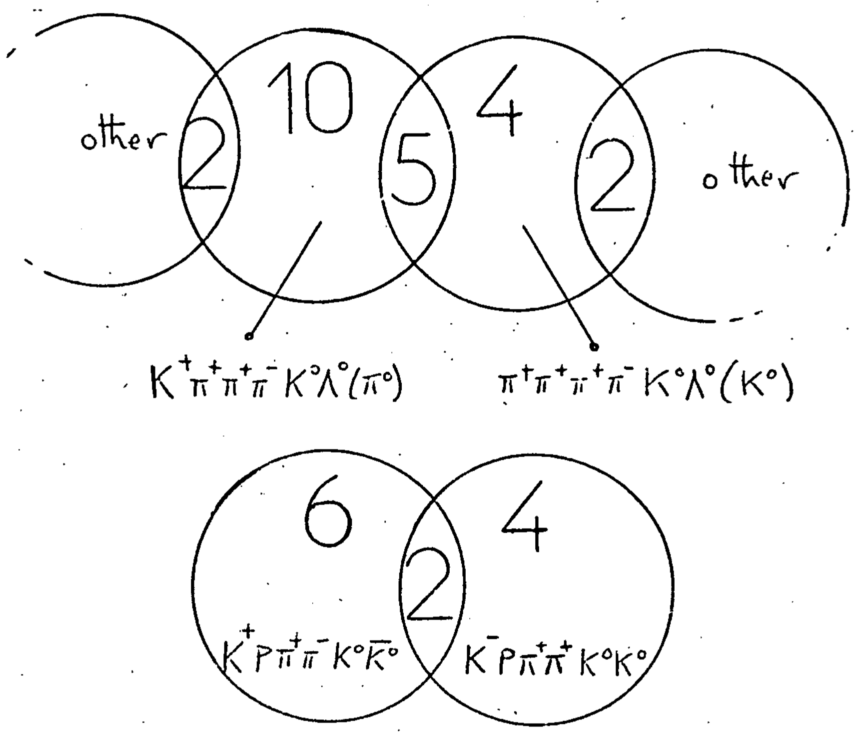

b) Birmingham Data

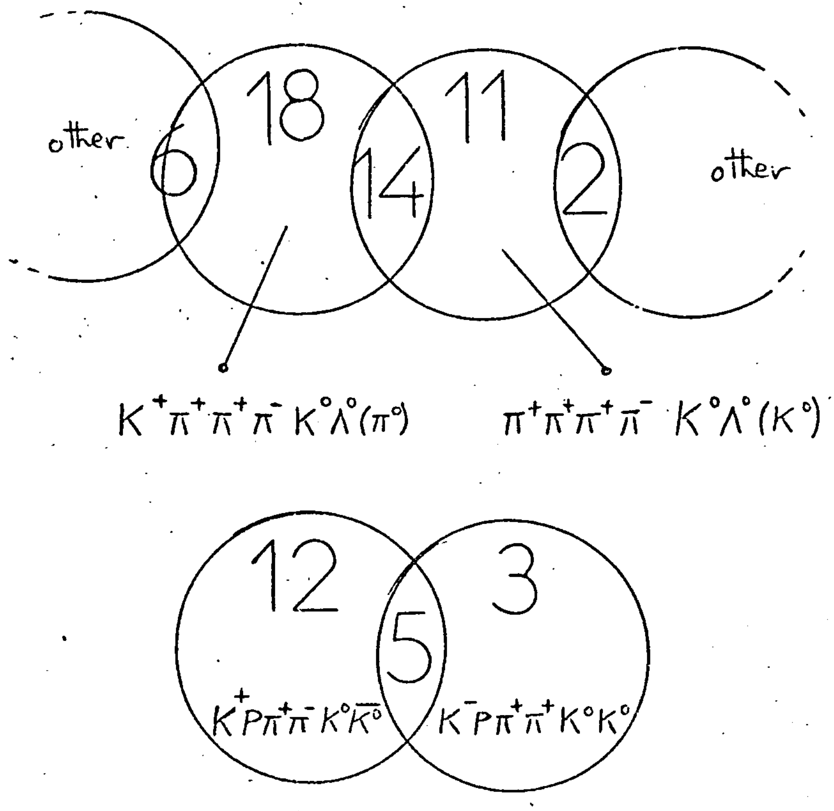

Ambiguities: Topology 211 and 411

FIG 3.21

a) Edinburgh data: 211

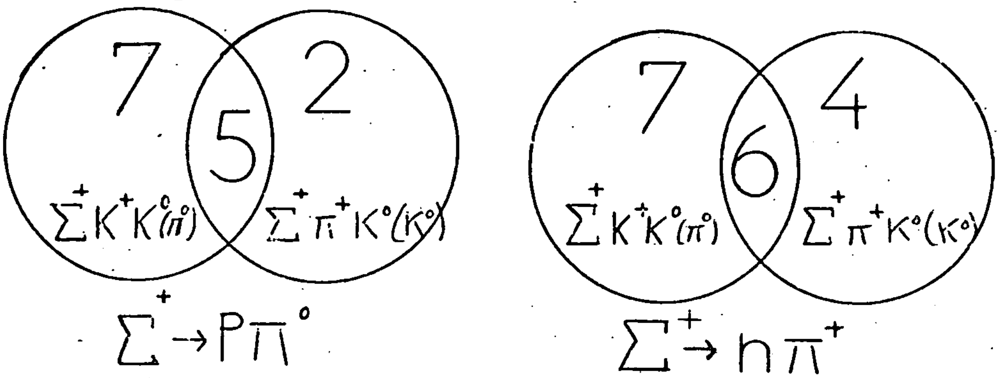

b) Birmingham data: 211

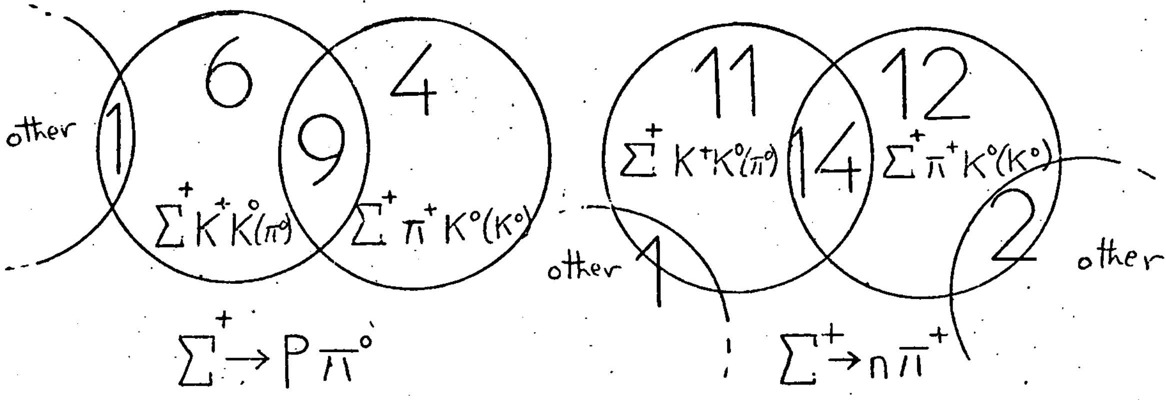

c) Birmingham data: 411

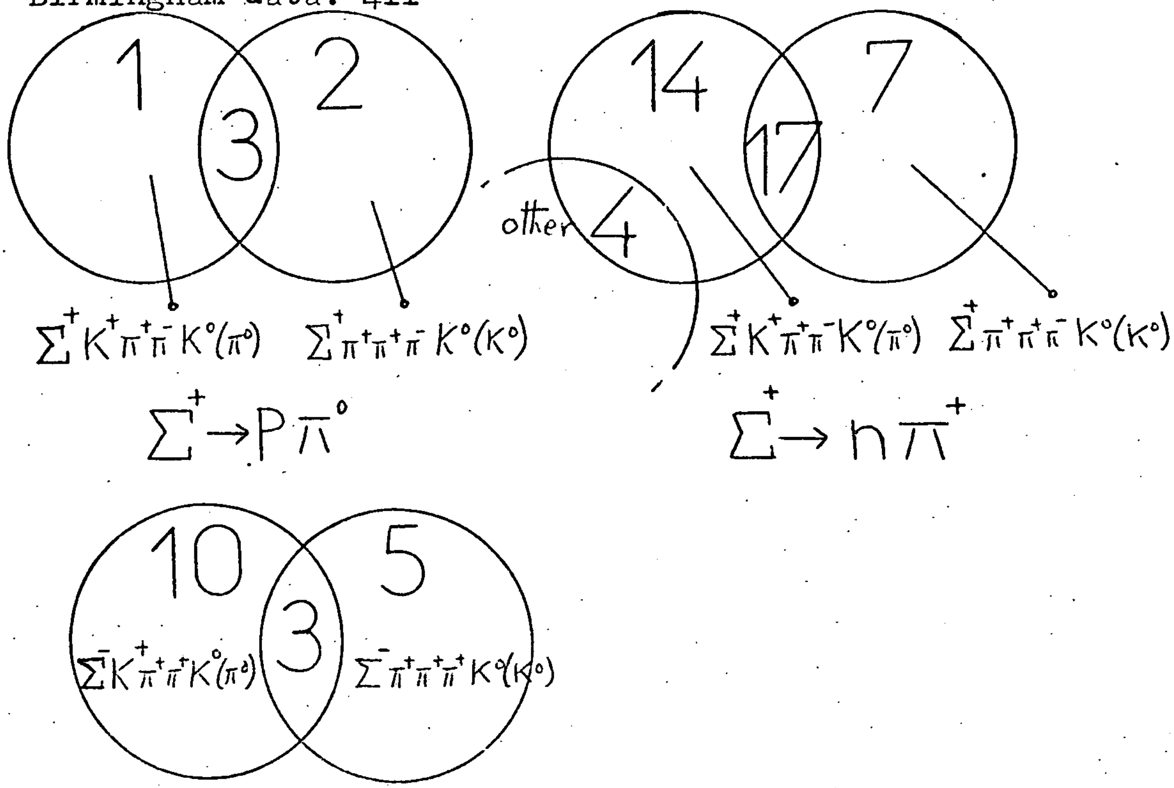

In general, the 402-type hypotheses are more contaminated by ambiguities than are the 202-types. Only the dominant channels are shown in Fig. 3.20.

Finally, Fig. 3.21 shows the ambiguities found in the 211 and 411 type of hypotheses.

The general impression gained from these diagrams is one of entanglement, really not surprising with six and seven body final states at high energy. The combination of different channels is difficult and probably not instructive, and one cannot separate final states containing K^oK^o or $K^o\overline{K}^o$ with any confidence. Combined cross-section estimates were thus not attempted.

3.6 The Λ^o/Σ^o Ambiguities

There were many ambiguities between the hypotheses

$$K^+P \longrightarrow K^+\pi^+K^o\Lambda^o \qquad (1)$$

and $$K^+P \longrightarrow K^+\pi^+K^o\Sigma^o \qquad (2)$$

and between the hypotheses,

$$K^+P \longrightarrow K^+\pi^+\pi^+\pi^-K^o\Lambda^o \qquad (3)$$

and $$K^+P \longrightarrow K^+\pi^+\pi^+\pi^-K^o\Sigma^o \qquad (4)$$

e.g. there were 10 unique fits to reaction (1), 9 unique fits to reaction (2) and 27 fits were ambiguities between (1) and (2). The Σ^o decays electromagnetically,

$$\Sigma^o \longrightarrow \Lambda^o\gamma$$

in a time so short that its decay vertex is, for measurement purposes, at the same position as the production vertex. The gamma from the decay is usually not seen, so that three constraints are lost.

In the C.M.S. of the Σ^o, the decay should be isotropic, so that if one plots the distribution in $\cos\theta^*$ where θ^* is the angle between the gamma in the C.M.S. of the Σ^o, and the direction of the Σ^o in the laboratory, the distribution should be flat.

If events which were examples of genuine Λ^o production were fitted to Σ^o production, one would expect the $\cos\theta^*$ distribution to be peaked backwards, since the Σ^o is more massive than the Λ^o.

Let F and B respectively represent the numbers of events in the forward and backward hemispheres in the Σ^o C.M.S. Then one may define the asymmetry by a number, k, where

$$k = \frac{B - F}{B + F}$$

so that k represents the fraction of ambiguous events which are genuine Λ^o events.

Let $$B + F = N,$$

then $$k = 1 - \frac{2F}{N} \implies \Delta k \approx -\frac{2}{N}\Delta F$$

which gives the likely error in k.

Approximately, $$\Delta F = NP(1 - P)$$

where P = probability of the event lying in the forward direction, $\approx \frac{F}{N}$

i.e. $$k \approx \sqrt{\frac{2FB}{N^3}}$$

then $$k = \frac{B - F}{B + F} \pm \sqrt{\frac{2FB}{N^3}} .$$

Fig. 3.22 shows the $\cos\theta^*$ distribution for events ambiguous between hypotheses (1) and (2) above. Then F = 5, B = 22,

FIG 3.22

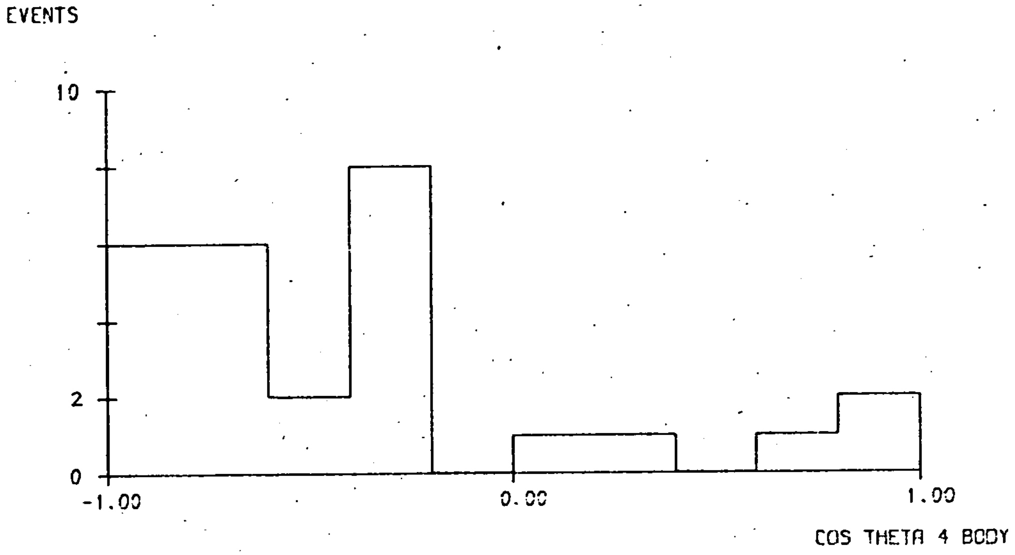

Σ^{o}/γ decay angle for 4-Body final states

FIG 3.23

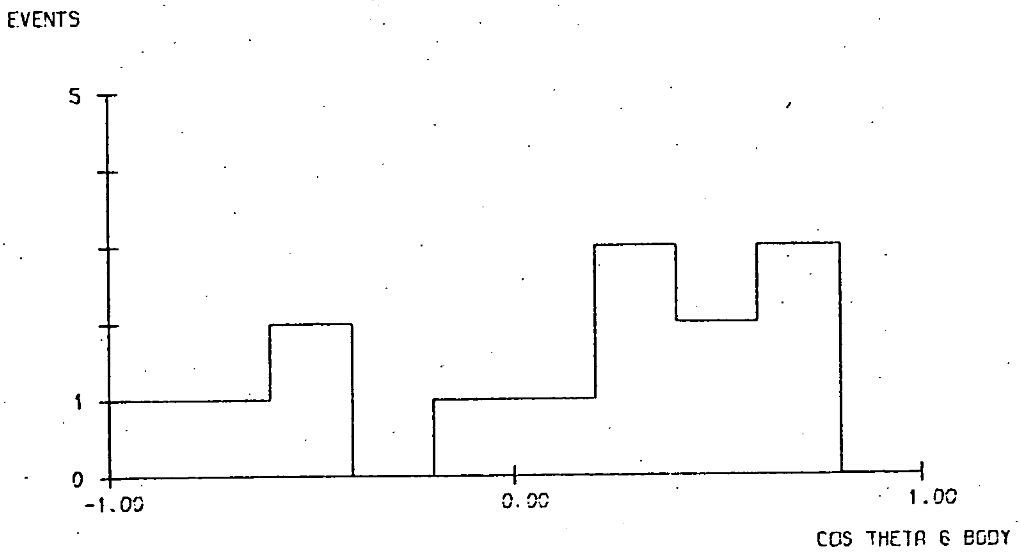

Σ^{o}/γ decay angle for 6-Body final states.

N = 27

i.e. $k = 0.63 \pm 0.11$, which implies that of the 27 ambiguous events, the number of genuine Λ^{o} events $= 17 \pm 3$.

For the six-body final states, which are ambiguous between hypotheses (3) and (4) above, the $\cos\theta^{*}$ distribution is shown in Fig. 3.23. Then $B = 5$, $F = 8$,

$$\text{and} \qquad k = -0.23 \pm 0.20,$$

which is consistent with uniformity.

The results above were used to apportion the ambiguous events and calculate the resulting cross-sections listed in Appendix 3B.

3.7 Error on Cross-section due to Random Fluctuation

For a large number, N, of events, the statistical fluctuation is taken to be $\pm\sqrt{N}$, according to Poisson statistics. However, for small N, this is no longer true and a proper calculation of the likely error in N shows that for $N \lesssim 5$, the error is asymmetric, and for $N = 1$ the uncertainty in the positive direction is twice as large as that in the negative direction, e.g. only one example of the reaction

$$K^{+}p \longrightarrow \Xi^{+}\, p\, \Lambda^{o}(\pi^{o})$$

was observed and its cross-section was estimated as,

$$\sigma = 0.5 \begin{smallmatrix} +0.7 \\ -0.3 \end{smallmatrix}\ \mu b \ .$$

The Likelihood function for N (observed) is shown in Fig. 3.24, for different values of N. It is clear from this figure that as N increases the asymmetry becomes less, very

FIG3.24

LIKELIHOOD FUNCTION FOR CROSS-SECTION FOR N EVENTS

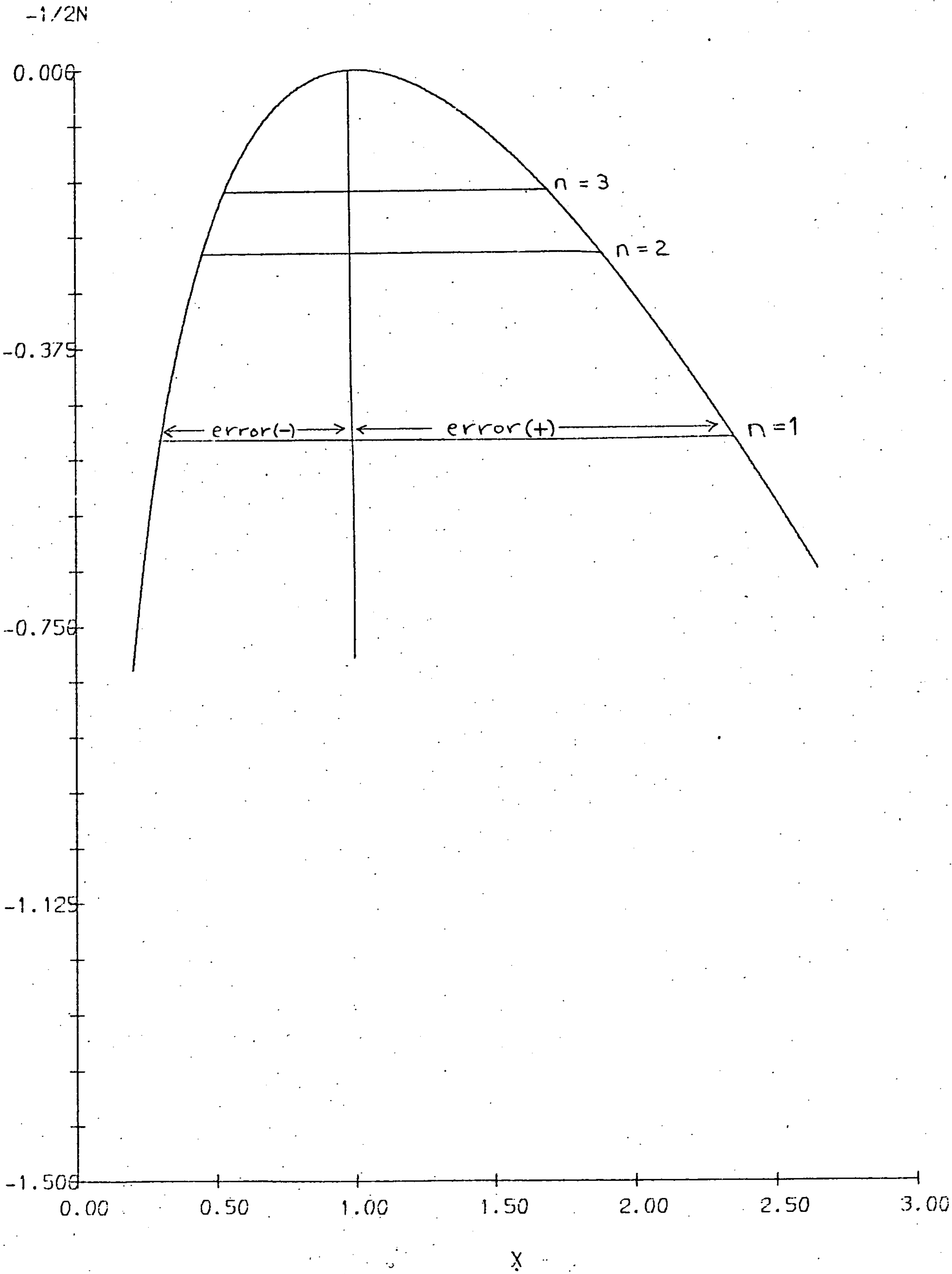

rapidly, and for n = 5, the asymmetry is 15°/o. The derivation of the Likelihood function employed is given in Appendix 3C.

3.8 Reliability of Single Constraint Interaction Fits

In most cases, the hypothesis fitted includes an unseen neutral from the interaction vertex, i.e. a one constraint fit.

e.g. $$K^+P \longrightarrow \pi^+\pi^+\Lambda^oK^o(K^o) \quad .$$

It seems likely that in some cases, the Kinematics program will be unable to distinguish between the above case and

$$K^+P \longrightarrow \pi^+\pi^+\Lambda^oK^o(K^o\pi^o)$$

because of the small mass of the π^o.

As a check, events which gave unique 1C fits to the 202 hypothesis,

$$K^+P \longrightarrow K^+\pi^+K^o\Lambda^o(\pi^o)$$

were tried out on the 201 hypothesis,

$$K^+P \longrightarrow K^+\pi^+\Lambda^o(K^o).$$

Seven good 201 type fits were obtained to the original 22 unique 202 type fits.

It was also noticed that good 203-type events which gave fits to hypotheses involving an unseen π^o, often gave fits to 202-type hypotheses involving only one unseen particle.

These facts throw doubt on the reliability of 1C fits at this energy.

3.9 REFERENCES FOR CHAPTER III

(1) Scotter, D.G. et al., Nuovo Cimento 62A (1969) 1057.

(2) 'Review of Particle Properties', Physics Letters 39B (1972) xiv.

(3) 'A Kinematical Fitting Program for the Analysis of Bubble Chamber Events', A.G. Wilson N.I.R.L./M/38, page 19.

CHAPTER IV

RESONANCE PRODUCTION IN RARE FINAL STATES

4.1 Introduction

4.2 The Oxford Film

- 4.2.1 Measuring and Data Processing
- 4.2.2 Scanning Efficiency
- 4.2.3 Processing Efficiency
- 4.2.4 Chi-squared Probability of Fit
- 4.2.5 Estimation of a Microbarn Equivalent
- 4.2.6 Tau-scanning on the Oxford Film
- 4.2.7 Cross-section Calculations

4.3 Resonance Production

- 4.3.1 The States $K^+\pi^+K^0\Lambda^0\pi^0$ and $\pi^+\pi^+K^0\Lambda^0K^0$
- 4.3.1.1 Λ^0 Production
- 4.3.1.2 The $K\pi$ mass enhancements.
- 4.3.2 The $K\bar{K}$ System
- 4.3.2.1 Reactions studied
- 4.3.2.2 The $K_1^0 K_1^0$ Effective Mass Spectrum
- 4.3.2.3 The f'(1514) Meson
- 4.3.2.4 Production Characteristics of the $K_1^0 K_1^0$ System

4.4 Conclusion

4.5 References for Chapter IV.

CHAPTER IV

RESONANCE PRODUCTION IN RARE FINAL STATES

4.1 Introduction

For this study, the data obtained from the Run 4 and Run 5 film was combined with that from the Run 1 and Run 3 film, which had been analysed separately in Edinburgh by the author. This latter batch of film consisted of 62 half rolls of film sent to Edinburgh from Oxford University Physics Department in 1970. Before looking at final state distributions, a brief description of the analysis of this film will be given.

4.2 The Oxford Film

It was intended that the analysis of this film should not only produce more rare events, but also serve as a fair operational test of the recently commissioned "Vanguard" measuring machine, set up in Edinburgh, together with the associated computer software. The machine had previously been tested on a small number of events on the Run 4 film, and performed satisfactorily, as described elsewhere(1).

4.2.1 Measuring and Data Processing

The Vanguard measuring machine was linked to a PDP8 Computer in the Physics Department, which performed on-line checking for the measurer, using a program WEED(2), which also wrote the measuring data on to magnetic tape.

This data was then interpreted by a program called SEEWEED(3), which re-arranged the data into a form suitable for presentation to the 'Geometry' program at Glasgow University.

Due to the incompatibility of the PDP8 Computer tape, Edinburgh Regional Computing Centre (E.R.C.C.) tape, and the Glasgow University Computer tape, hold-ups were frequent, and the fastest possible time for analysis of an event was about three days, allowing for transit time between the computers. Difficulties were also experienced with hardware errors from the electronics panel attached to the Vanguard machine, and a great deal of computing was necessary to rectify the faulty data, before it was passed to the 'Geometry' program. A small change was later made to "WEED" which overcame the problem.

4.2.2 Scanning Efficiency

All the film was double-scanned in Edinburgh, and check-scanned by the author. The efficiencies were calculated as in Chapter III, and gave the following results:

Topology	Efficiency
202 (203)	96°/o ± 3°/o
211 (212)	93°/o ± 6°/o
402 (403)	96°/o ± 4°/o
411 (412)	98°/o ± 2°/o

4.2.3 Processing Efficiency

As far as possible, every event was given two chances for kinematic analysis, if it failed the first attempt.

Let there be a total, N_T, of scanned events, and let there be N_G events which have a "flaw" causing them to fail 'Geometry' repeatedly. Of the $(N_T - N_G)$ events remaining, let N_K correspond to fittable reactions. Let 'M' be the measuring efficiency and let 'K' be the efficiency for fitting a measured event to the correct hypothesis.

Assume that M and K are the same for all measures and all topologies.

Fig. 4.1 shows the breakdown of events, from scanning to fitting. Then on the first measure, and re-measure respectively one has,

$$189 = (242 - N_G)M$$

$$\text{and} \quad 38 = (53 - N_G)M$$

i.e. $N_G \approx 5$ events, and in fact 5 events repeatedly failed Geometry. One therefore considers the number of 'clean' events to be 237.

Then on the first measure,

$$M = \frac{189}{237} = 80^{o}/o = \text{measuring efficiency.}$$

Furthermore, on the first measure, from Fig. 4.1

$$88 = N_K\, M\, K$$

and on the first kinematic re-measure,

$$12 = N_K\, M(1 - K)M\, K.$$

FIG 4.1

Measuring the 'Oxford' Film

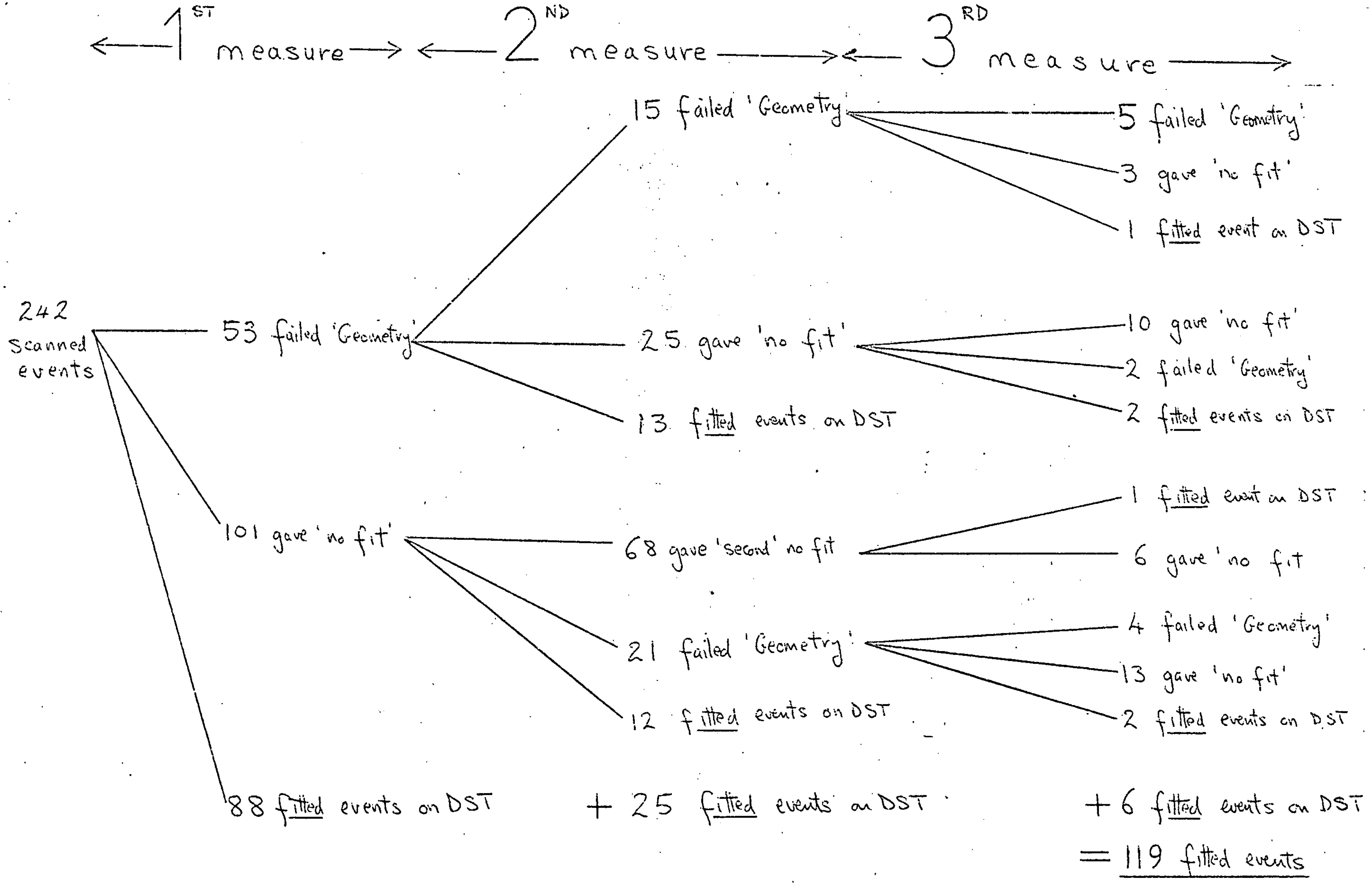

These equations give $K = 83^\circ/o$ = kinematic efficiency, and $N_K = 133$ events.
The total number of events fitted after three measures = 119 events, therefore the overall efficiency, E, is

$$E = \frac{119}{133} = 89.5^\circ/o \ .$$

To estimate the error involved, a formula similar to that used to find the error on a single-scan efficiency, was used for each of the three measures. In this way the error was estimated as $10^\circ/o$, and the final processing efficiency, P, taken as

$$\underline{P = 90^\circ/o \pm 10^\circ/o} \ .$$

4.2.4 Chi-squared Probability of Fit.

The distribution in chi-squared probability of fitted events from the Oxford film sample is shown in Fig. 4.2, and is considered to be acceptably flat.

4.2.5 Estimation of Microbarn Equivalent

A beam count was taken every 50 frames, and a check was kept on the number of bad frames. In the Run 1 film the number of tracks per frame was 16.1 ± 4.8, with $3.5^\circ/o$ bad film, and in the Run 3 film, there were 12.0 ± 3.8 tracks per frame, with $4.5^\circ/o$ bad film. The general film quality was poor.

Runs 1 and 3 were known to have a fairly high beam contamination, and previous work(4) on this film, using comparison scans with the R.F. separators off and on, indicated that the

FIG 4.2

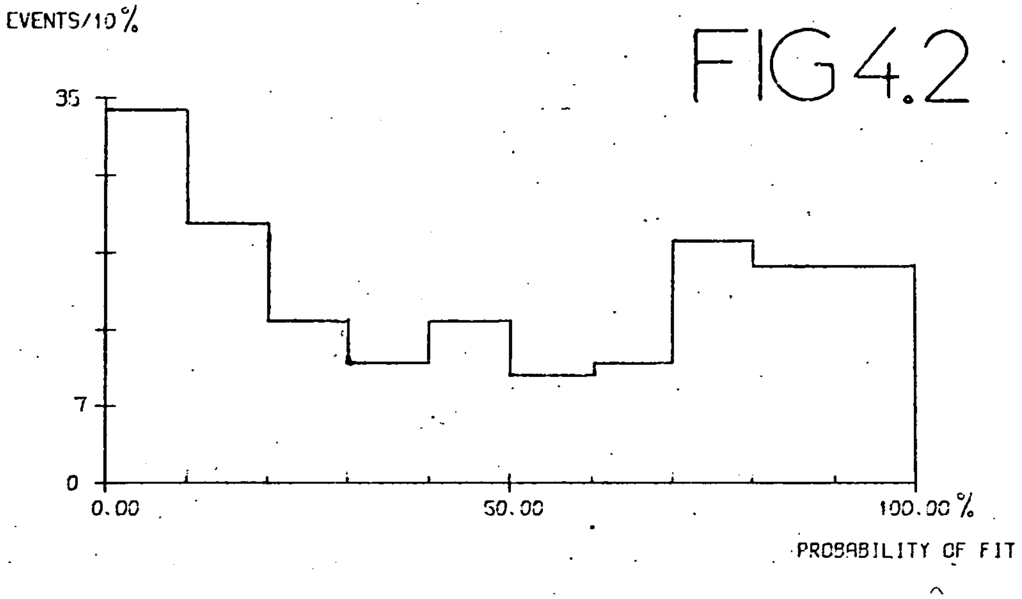

Chi-squared probability of fit: 'Oxford' data.

FIG 4.3

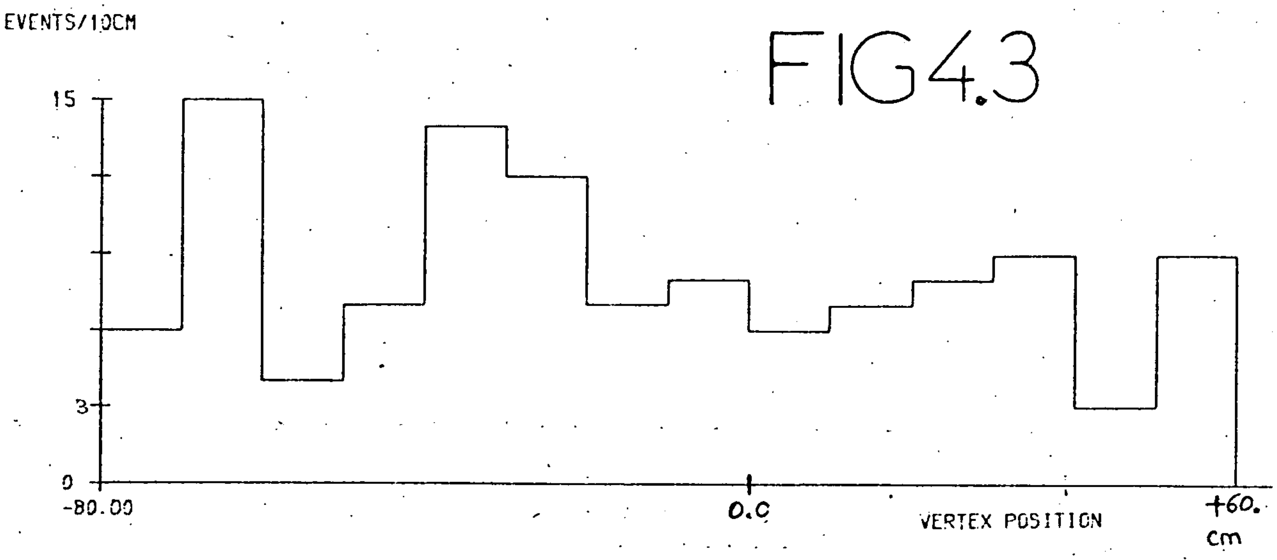

Vertex position of fitted events: 'Oxford' data.

likely contamination was as follows:

	Run 1	Run 3
Average number of protons per frame	0.5	1.3
Average number of muons per frame	3.35	1.9

Using these results, the estimated total number of tracks on the Oxford film was

$$N_T = (4.36 \pm 0.46) \times 10^5 \text{ tracks.}$$

Figure 4.3 shows the vertex position in the X-direction of 118 fitted events on the Oxford film, and the distribution is seen to be reasonably flat over the fiducial length of 1.35m. The above figures lead to an estimated microbarn equivalent for the Oxford film, of

$$\sigma/N = (0.34 \pm 0.04)\mu b \text{ per event.}$$

4.2.6 Tau-scanning on the Oxford Film

As well as scanning for rare events, the Oxford film was also scanned for "tau"-decays, i.e. the decay of a beam track into three charged prongs, presumed to derive from,

$$K^+ \longrightarrow \pi^+\pi^-\pi^+ .$$

A total of 206 examples were found in the film, but were not measured. Using the scanning efficiency for tau decays (73°/o ± 7°/o), the estimated true number of tau decays was,

$$N_T = 296 \pm 25 \text{ events.}$$

The tau's were scanned in a restricted fiducial region of 0.96 m, and using the above number, the estimated total beam track length was

$$L = (5.98 \pm 0.5) \times 10^5 \text{m}.$$

Using the information derived from beam track counts in Section 4.2.5, gives an estimated beam track length of

$$L = (5.88 \pm 0.66) \times 10^5 \text{m},$$

in good agreement with that derived from tau-decays.

4.2.7 Cross-Section Calculations

To compare estimates of cross-section calculated from the Oxford film, and the 1968 film, two reactions were chosen:

a) $K^+P \longrightarrow K^+P\, K^o\, \overline{K}^o$

- a well constrained but scarce channel.

b) $K^+P \longrightarrow K^+\pi^+\, \Lambda^o K^o (\pi^o)$

- a more abundant but less well-constrained channel.

The usual corrections, described in Chapter III, were made and the results compared.

a) $K^+P \longrightarrow K^+P\, K^o\, \overline{K}^o$

The cross-section as estimated from analysis of the Oxford film is

$$\sigma = (7.3 \begin{smallmatrix} +5.2 \\ -3.5 \end{smallmatrix})\, \mu b$$

compared with

$$\sigma = 12.9 \pm 2.7 \ \mu b$$

calculated from analysis of the 1968 film.

b) $K^+P \longrightarrow K^+\pi^+K^o\, \Lambda^o(\pi^o)$

The cross-section calculated from the Oxford film is

$$\sigma = 36.5 \pm 11\ \mu b$$

compared with

$$\sigma = 38.6 \pm 5\ \mu b$$

calculated from the 1968 film.

The agreement in cross-section values is good, and it was found that the general pattern of ambiguities in the fitted hypotheses was very similar to that found for the data from the 1968 film, implying that the data obtained from the Oxford film is compatible with that obtained from the 1968 film.

4.3 Resonance Production

It was found that with such complicated final states, the large number of combinations to be taken into account in mass distribution produces a large experimental background, which makes difficult, with the low statistics available, the identification of resonances. Furthermore, most of these multi-body final states can be studied only in one-constraint reactions, of which a high proportion of events are ambiguous with other one-constraint, or multi-neutral reactions.

4.3.1 The States $K^+\pi^+K^o\Lambda^o\pi^o$ and $\pi^+\pi^+K^o\Lambda^oK^o$

These states were fitted as the hypotheses,

$$K^+P \longrightarrow K^+\pi^+K^o\Lambda^o(\pi^o) \qquad (1)$$

and

$$K^+P \longrightarrow \pi^+\pi^+K^o\Lambda^o(K^o) \qquad (2)$$

They are the most prolific of the rare final states, and their main ambiguity is with each other. For initial analysis, all mutually ambiguous states were assumed to be genuine examples of hypothesis (2). This results in 182 "uniquely" assigned states. There was a total of 153 fits to hypothesis (1), of which 85 were unique, a total of 97 fits to hypothesis (2), of which 47 were unique, and 40 of which were ambiguous with hypothesis (1).

4.3.1.1 Λ^o Production

The C.M.S. production angles, $\cos \theta^*$, of the Λ^o in the above states is shown in Fig. 4.4 where it is seen that, as expected, the distribution is strongly peaked in the backwards direction. Approximately 20°/o of the Λ^o's are produced in the forwards direction.

If one looks for enhancements in the $\overset{o}{\Lambda}\pi$ effective mass spectrum, there are two entries per event, giving the 364 entries shown in Fig. 4.5, where there are no obvious enhancements and the distribution resembles phase space.++

If one now assigns all ambiguous states to hypothesis (1) instead, this gives the mass spectrum shown in Fig. 4.6, which has a general shape bearing a truer resemblance to phase space, but with more of a suggestion of a peak centred on the bin, $1360 \longrightarrow 1400$ MeV/c^2, i.e. in the $\Sigma(1385)$ region. The $\Sigma(1385)$ is a well established $I = 1, {}^3/2^+$ resonance whose main ($\sim$ 90°/o) decay mode is $\Lambda\pi$, and which has a width of 34 MeV/c^2.

It was thought that the distributions might be improved by making cuts on the missing-mass squared (MMS) of the unseen

++ See Appendix 4A.

FIG 4.4

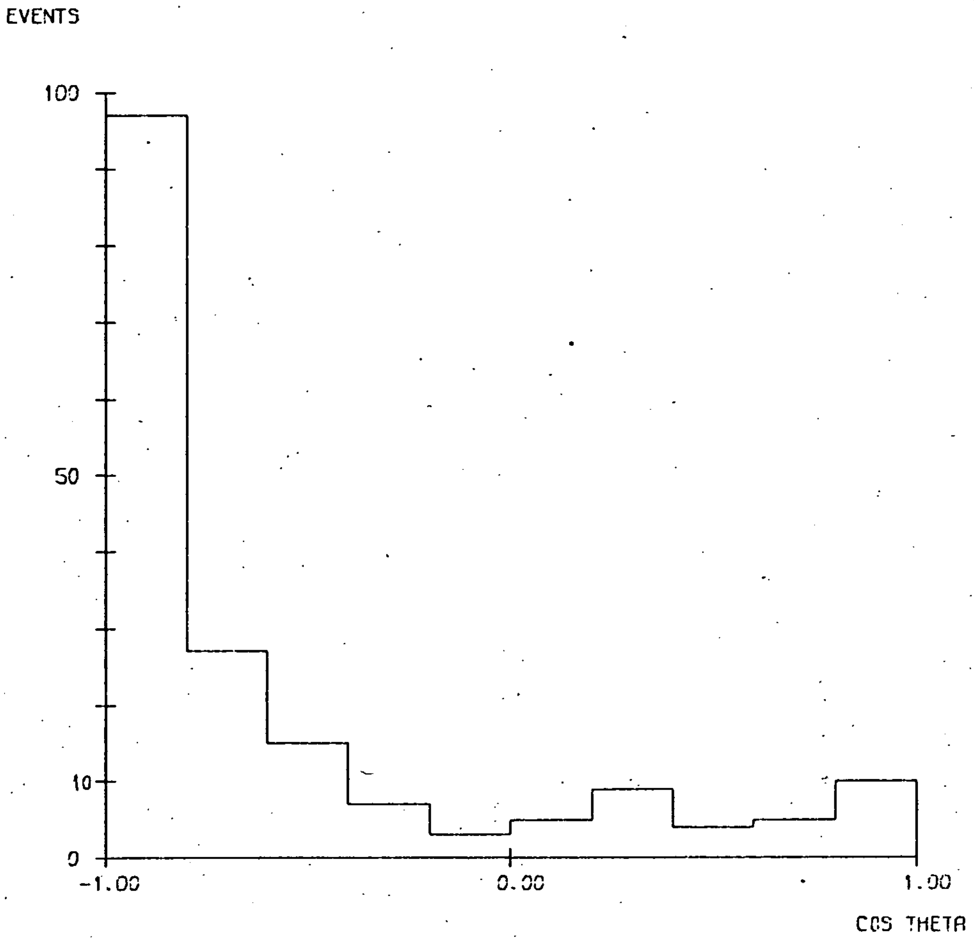

CMS production angle of the Λ^0 from,

$K^+P \; K^0 \Lambda^0 (K^0)$

and $\pi^+\pi^+K^0 \Lambda^0 (K^0)$

FIG4.5

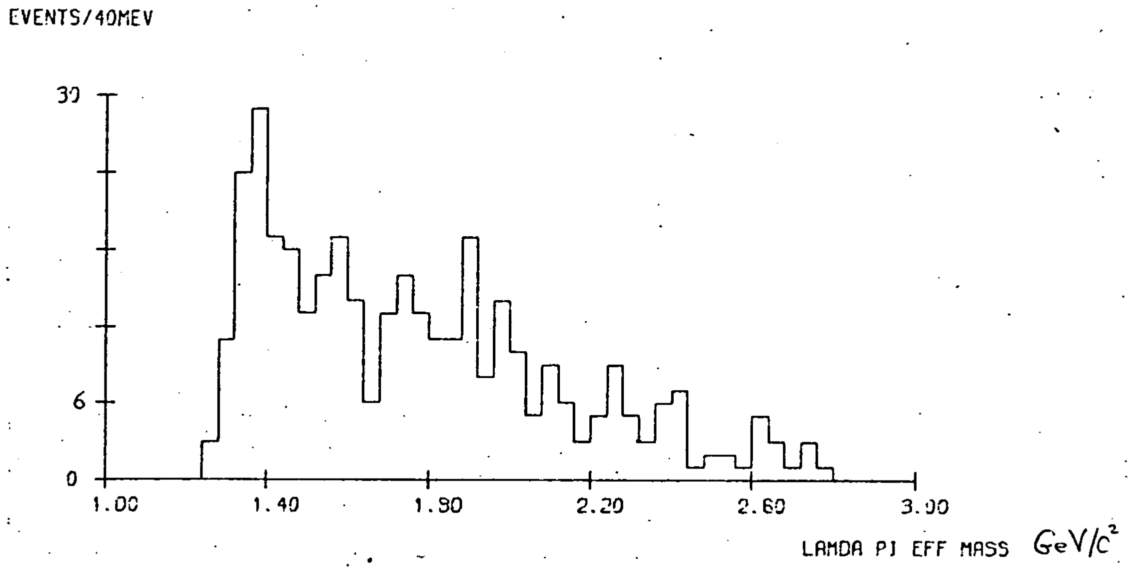

$\Lambda\pi$ effective mass: unique $K^+\pi^+K^0\ \Lambda^0(\pi^0)$

all $\pi^+\pi^+K^0\ \Lambda^0(K^0)$.

FIG4.6

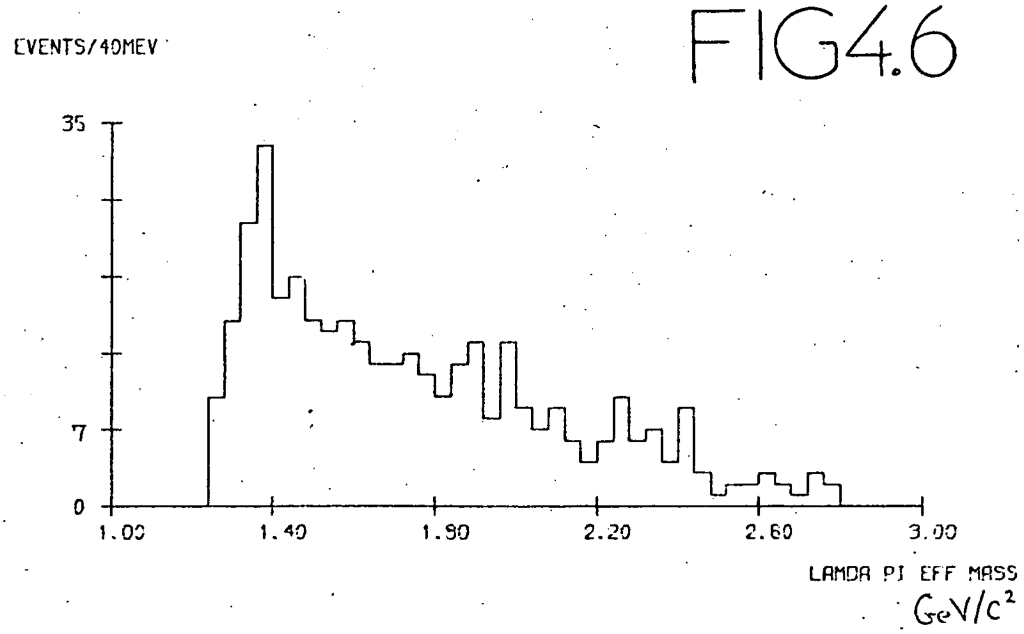

$\Lambda\pi$ effective mass: unique $\pi^+\pi^+K^0\Lambda^0(K^0)$

all $K^+\pi^+K^0\Lambda^0(\pi^0)$.

neutral from the interaction and the MMS distributions were examined.

Fig. 4.7 shows the distribution in MMS for the K^o from

$$K^+p \longrightarrow \pi^+\pi^+K^o\,\Lambda^o(K^o)\ .$$

The true value for the MMS of a K^o is 0.248 GeV^2 and the central bin in Fig. 4.7 is 0.22 ⟶ 0.30 GeV^2. The average error on these values is ~ 0.06 GeV^2 and it was decided to select only those events where the MMS of the K^o lay in,

$$(0.15 \leqslant MMS \leqslant 0.35)\ GeV^2.$$

Similarly, Fig. 4.8 shows the MMS distribution for the π^o from,

$$K^+p \longrightarrow K^+\pi^+K^o\,\Lambda^o(\pi^o).$$

The true value for the MMS of a π^o is 0.0182 GeV^2, and the centre of the distribution shown has a broad centre from 0.0 ⟶ 0.04 GeV^2. The average error on these values is ~0.03 GeV^2, and it was decided to select only those events where the MMS of the π^o lay in,

$$(-0.02 \leqslant MMS \leqslant 0.06)\ GeV^2\ .$$

The effect of applying these cuts to the events shown in Fig. 4.6 is shown in Fig. 4.9, where the distribution has not been improved and the general shape is worse, due to the smaller statistics.

It was felt that little more could be done to make the possible presence of a $\Lambda\pi$ resonance more clear, and simply concluded that there is reasonable evidence for some $\Sigma(1385)$ production.

FIG4.7

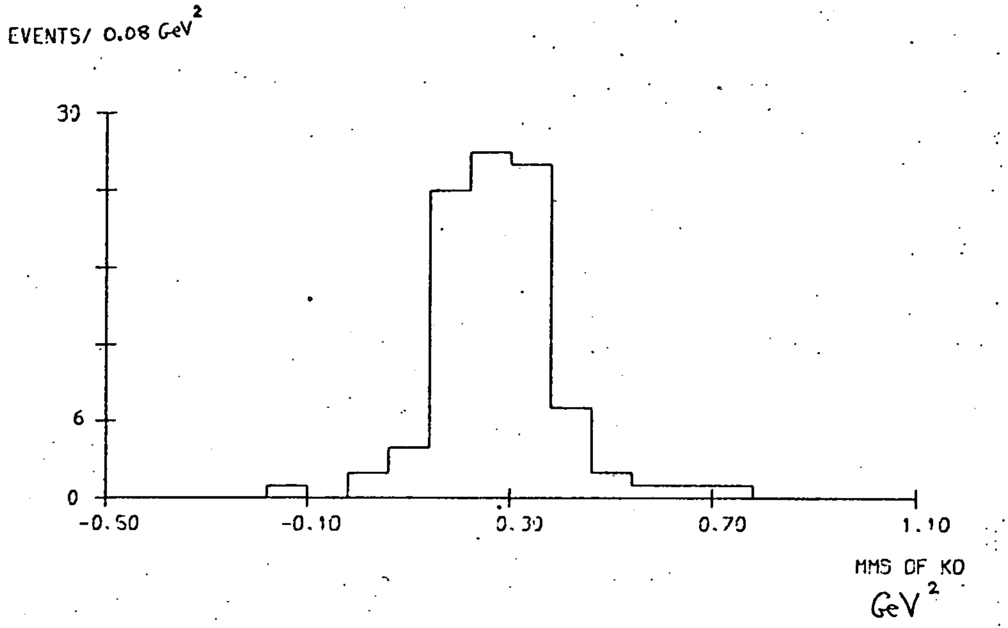

Missing-mass squared for $\pi^+\pi^+K^0\ \Lambda^0(K^0)$.

FIG4.8

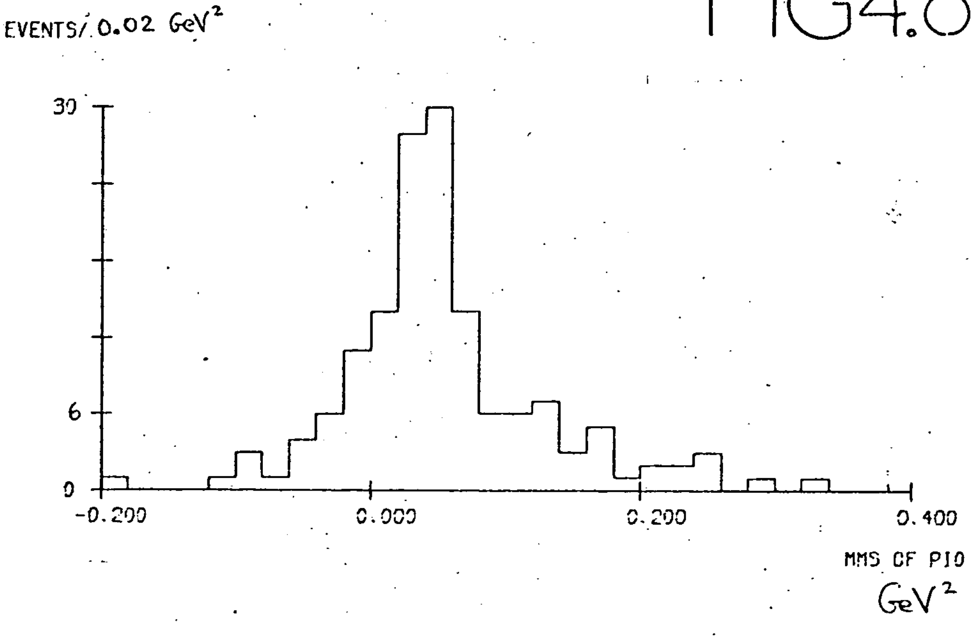

Missing-mass squared for $K^+\pi^+K^0\ \Lambda^0(\pi^0)$.

FIG 4.9

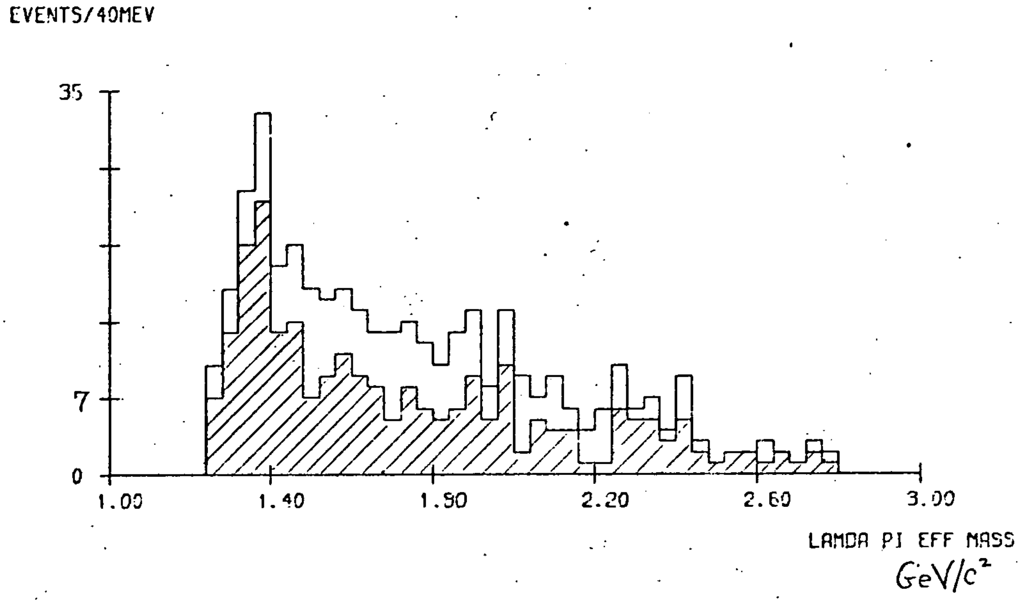

$\Lambda\pi$ effective mass: unique $\pi^+\pi^+K^o\Lambda^o(K^o)$
all $K^+\pi^+K^o\Lambda^o(\pi^o)$

The hatched histogram shows the effect of MMS cuts.

4.3.1.2 The Kπ Mass Enhancements

It is well known that the 3 and 4 body final states from K^+P interactions at various momenta are dominated by production of the $K^*(890)$ and to a lesser extent, of the $K_N(1420)$ resonances.

Again, reactions between hypotheses (1) and (2) were initially assigned to hypothesis (2). The effective mass distribution of the Kπ states in the 182 events is shown in Fig. 4.10. There are 3 possible combinations of K and π in hypothesis (1), and 4 possible Kπ combinations in hypothesis (2). There is a clear enhancement in the mass distribution in the region, $860 \longrightarrow 940$ MeV/c^2, due to $K^*(890)$ production and a suggestion of an enhancement in the region, $1420 \longrightarrow 1460$ MeV/c^2, which is presumably due to $K_N(1420)$ production.

If all ambiguities are now assigned to hypothesis (1), this gives the distribution shown in Fig. 4.11. The two distributions, 4.10 and 4.11 are strikingly similar and both show evidence for $K^*(890)$ production as well as possible $K_N(1420)$ production.

If one applies the MMS cuts described in Section 4.3.1.1, to the events in Fig. 4.11, this gives the distribution shown in Fig. 4.12 where, although the $K^*(890)$ is still clear and there is still a slight bump in the $K_N(1420)$ region, the background is large, due to the number of Kπ combinations to be taken into account.

It was thought that a Kπ resonance might be seen more clearly by choosing only those Kπ combinations where both

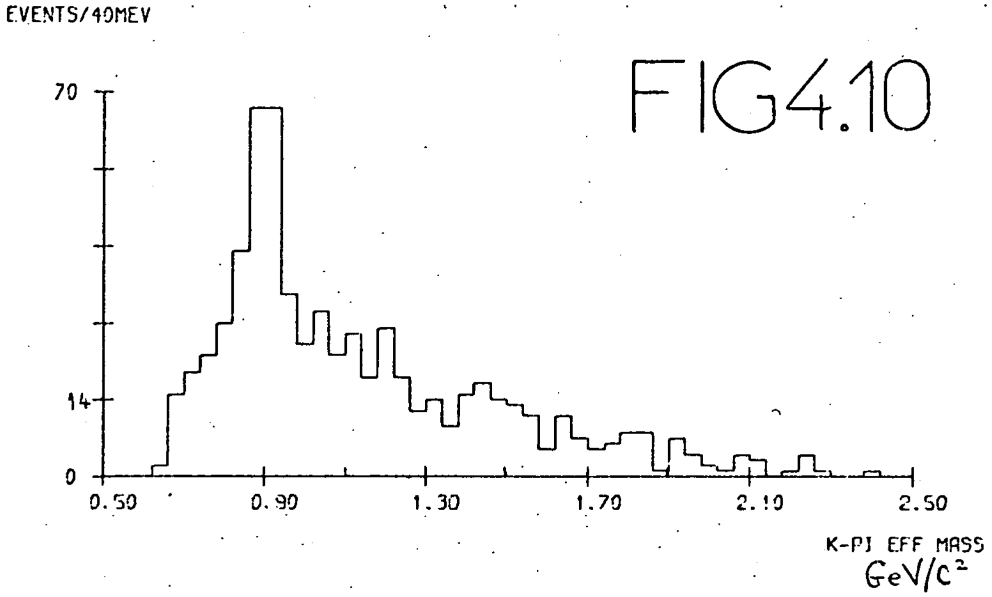

FIG4.10

Kπ effective mass: unique $K^+\pi^+K^0\,\Lambda^0(\pi^0)$
all $\pi^+\pi^+K^0\,\Lambda^0(K^0)$

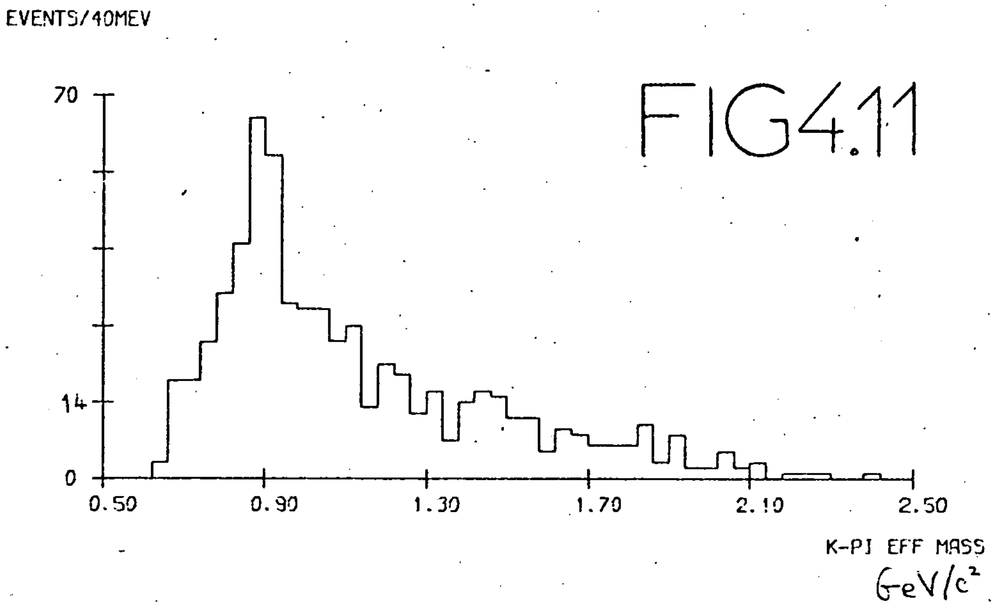

FIG4.11

Kπ effective mass: unique $\pi^+\pi^+K^0\,\Lambda^0(K^0)$
all $K^+\pi^+K^0\,\Lambda^0(\pi^0)$

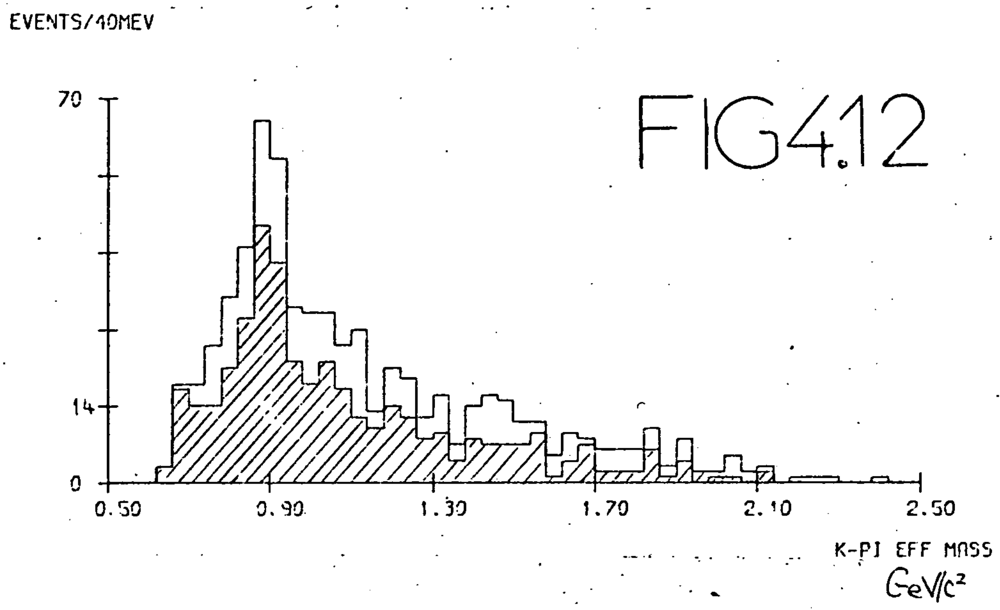

FIG 4.12

Kπ effective mass: unique $\pi^+\pi^+K^0\,\Lambda^0(K^0)$

all $K^+\pi^+K^0\,\Lambda^0(\pi^0)$.

The hatched histogram shows the effect of MMS cuts.

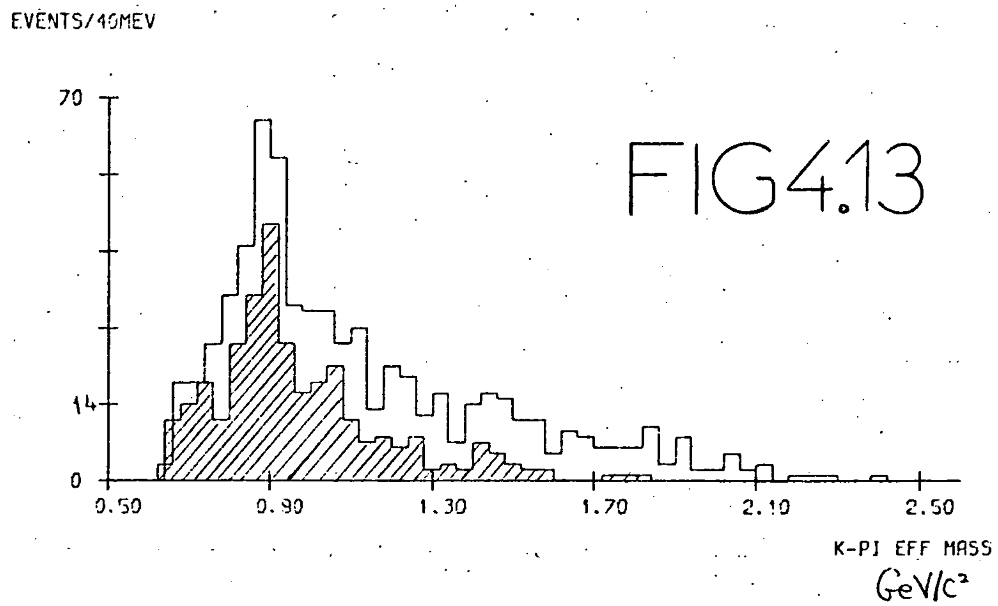

FIG 4.13

Kπ effective mass as above. The hatched histogram shows the effect of selecting K and π travelling in the same direction.

K and π travel either backwards or forwards together, in the C.M.S. The result of this selection on the events in Fig. 4.11) is shown in Fig. 4.13. There are still signs of the $K_N(1420)$, and the $K^*(890)$ peak is very sharp. It was felt that little more could be done to improve these distributions, given the low statistics and high background. No enhancements were found in the effective mass distributions of $K\pi\pi$ states.

4.3.2 The $K\bar{K}$ System

Enhancements in both neutral and charged $K\bar{K}$ effective mass spectra have often been observed, and their quantum numbers determined, enabling them to be successfully included in an SU(3) framework.

The enhancements ascribed to neutral singlet resonant states include such well established resonances as:

a) The $\phi(1019)$ meson,

a member of the vector nonet $(J^P = 1^-)$ of mesons, which also includes the K (890), the ρ and ω mesons. The $\phi(1019)$ may decay to K^+K^-, or to $K_1^o\ K_2^o$, but not to $K_1^o\ K_1^o$ or $K_2^o\ K_2^o$, because its C-parity is odd.

b) The f(1270) meson,

a member of the tensor nonet $(J^P = 2^+)$ of mesons, which also includes the $A_2(1310)$, the $K_N(1420)$ and the f'(1514) mesons. The f(1270) decays mainly to $\pi\pi$ but may also decay to K^+K^-, or to $K_1^oK_1^o$ or $K_2^oK_2^o$, but not to $K_1^oK_2^o$, because its C-parity is even.

c) The f'(1514) meson,
whose only observed decay mode is via $K\bar{K}$, and which is also even under C-parity.

The best known member of the I = 1 resonances which may decay to $K\bar{K}$ is the $A_2(1310)$, whose main decay mode is via $\rho\pi$. The $A_2(1310)$ is also even under C-parity.

4.3.2.1 Reactions Studied

The most convenient $K\bar{K}$ system to study in the rare final states is the $K_1^{\,o}K_1^{\,o}$ system, and to accumulate meaningful statistics, it is necessary to combine several different channels. Those selected were as follows:

$K^+P \longrightarrow K^+PK^o\bar{K}^o$	(1)	39 fits	(all unique)
$K^+P \longrightarrow K^+PK^o\bar{K}^o(\pi^o)$	(2)	59 fits	(25 unique)
$K^+P \longrightarrow K^+\pi^+K^o\bar{K}^o(n)$	(3)	53 fits	(9 unique)
$K^+P \longrightarrow K^+P\pi^+\pi^-K^o\bar{K}^o$	(4)	31 fits	(19 unique)
$K^+P \longrightarrow K^+P\,\pi^+\pi^-K^o\bar{K}^o(\pi^o)$	(5)	48 fits	(15 unique)

The only reaction of the above which was always uniquely identifiable was the first. A photograph of one example of the reaction,

$$\begin{array}{l} K^+P \longrightarrow K^+P\; K^o\bar{K}^o \\ \qquad\qquad\qquad\quad\; | \;\; \bar{K}^o \hookrightarrow \pi^+\pi^- \\ \qquad\qquad\qquad\quad\; K^o \hookrightarrow \pi^+\pi^- \end{array}$$

is shown in Plate I. Details of the momenta of the tracks involved are given in Table 4.1.

In reaction (3), only the unique fits were accepted, because of the severity of the ambiguity involved (e.g. see

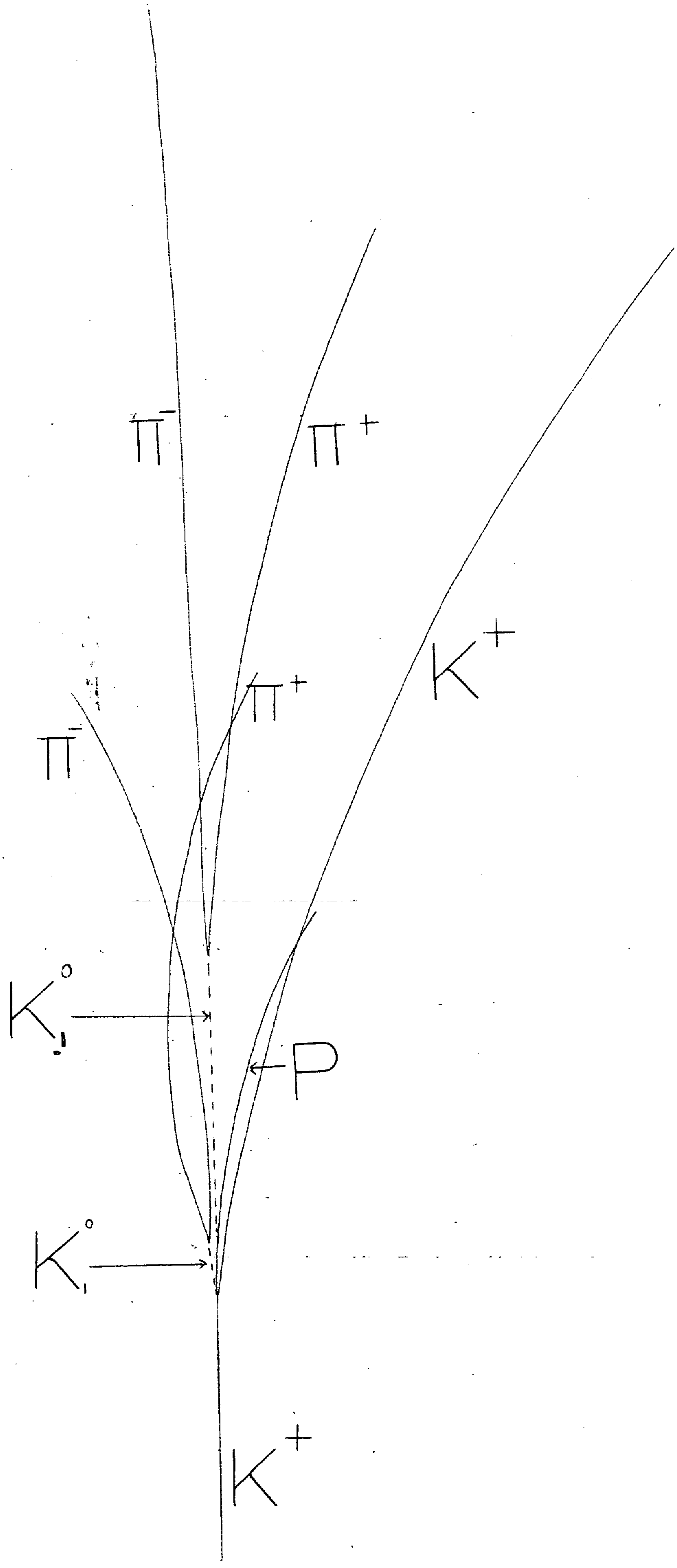
π^-
π^+
K^+
π^+
π^-
K_1^0
P
K_1^0
K^+

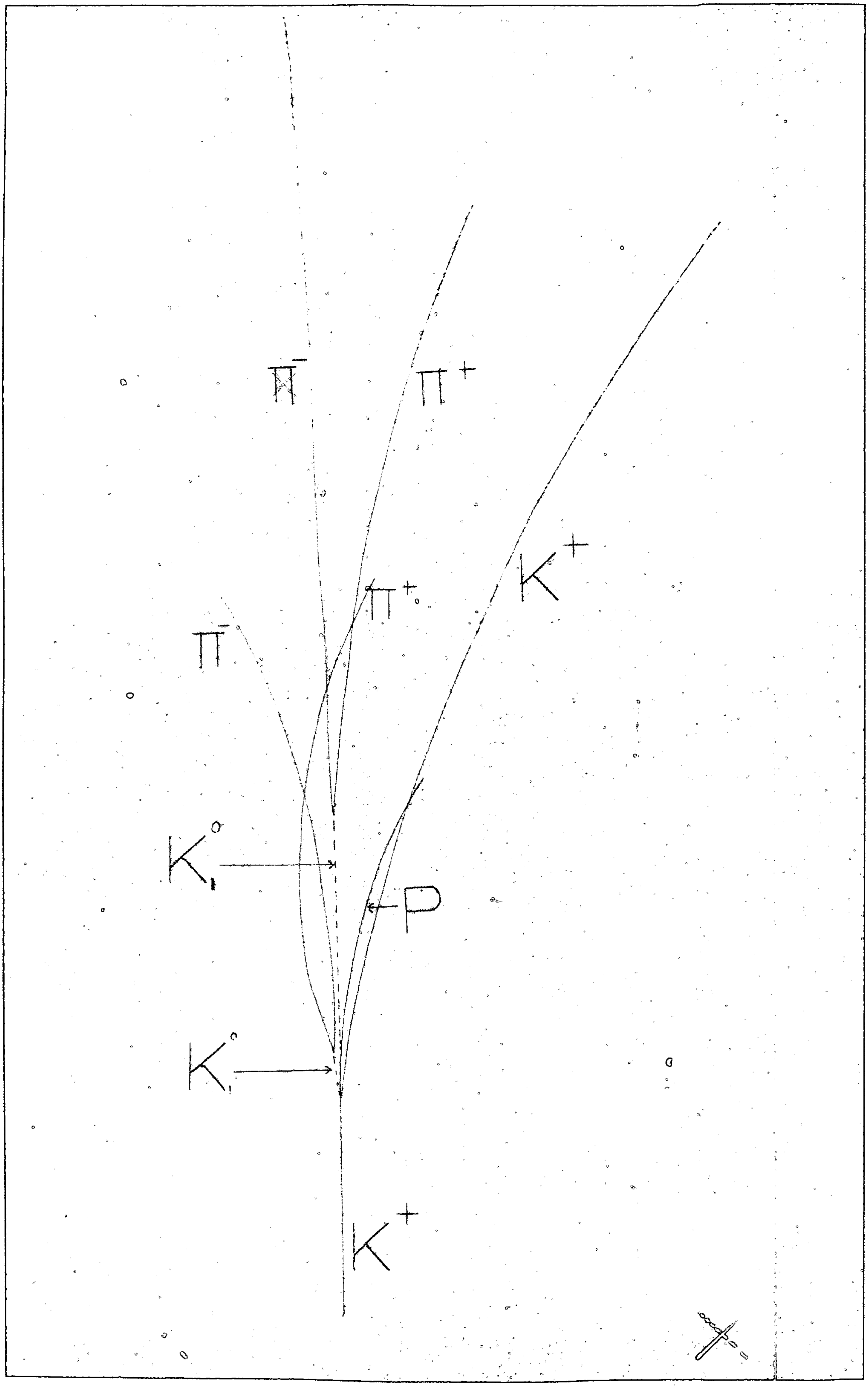

PLATE I

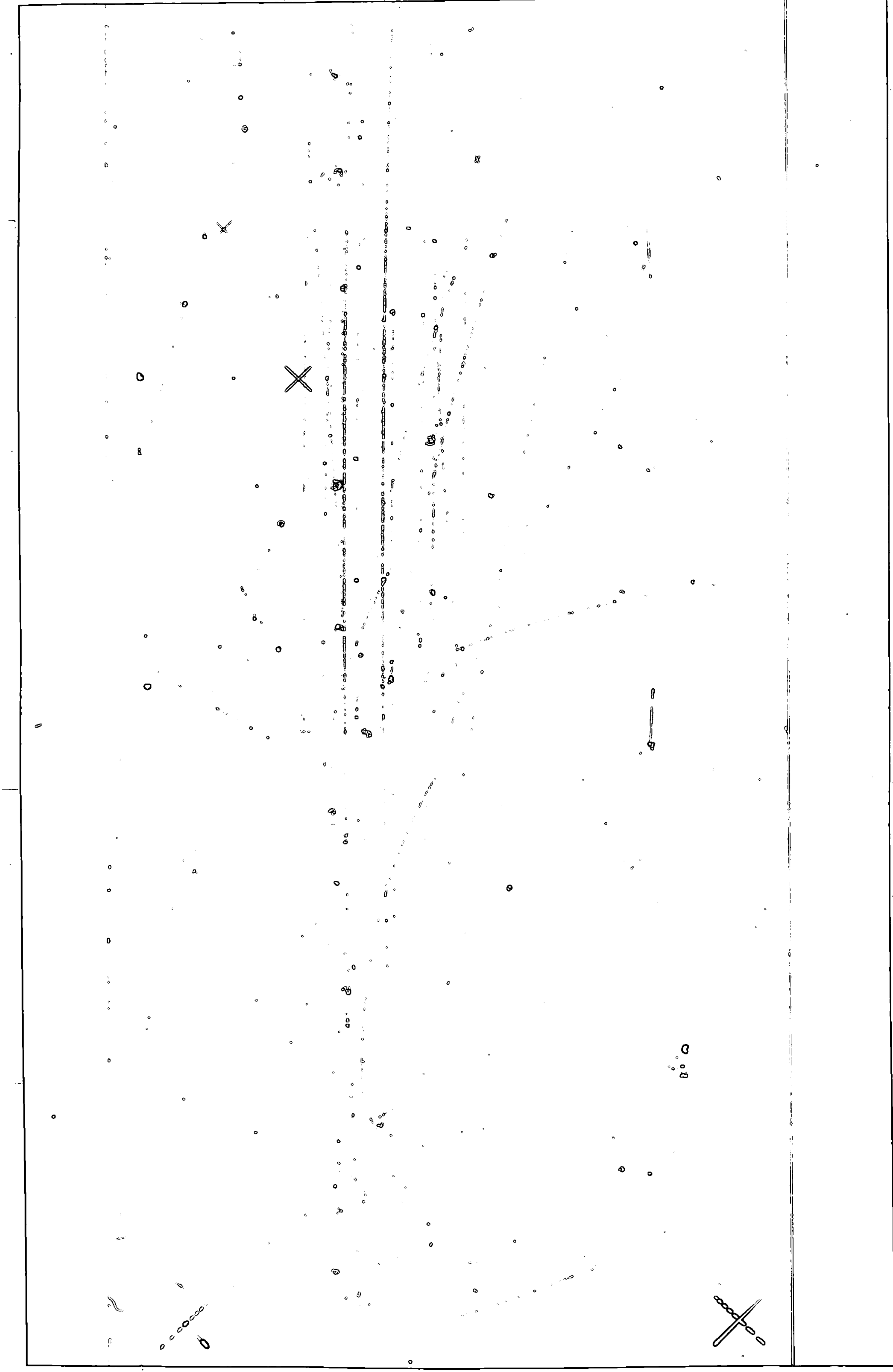

PLATE I

Chapter 3, Fig. 3.16). This leaves 186 examples of $K_1^o K_1^o$ production to be examined.

4.3.2.2 The $K_1^oK_1^o$ Effective Mass Spectrum

The distribution in effective mass of the $K_1^oK_1^o$ system in the 186 events is shown in Fig. 4.14. That due to the unique events only, is shown hatched.

There is a clear peak in the region, 1500 → 1540 MeV/c^2 more striking in the unique events, and presumably due to $K\overline{K}$ decay modes of the f'(1514) meson. There is also a small bump in the region of 1300 MeV/c^2, which might be due to $K\overline{K}$ decay modes of the f(1270) and/or the A_2(1310) mesons.

Table 4.1

Momentum of Tracks shown in Plate I

Track	Momentum (GeV/c)
K^+ (beam)	10.086 ± 0.100
From Interaction	
K^+	0.927 ± 0.009
P	0.298 ± 0.008
Lower K_1^o	
π^+	0.357 ± 0.005
π^-	0.463 ± 0.006
Upper K_1^o	
π^+	0.873 ± 0.007
π^-	7.267 ± 0.090

FIG 4.14

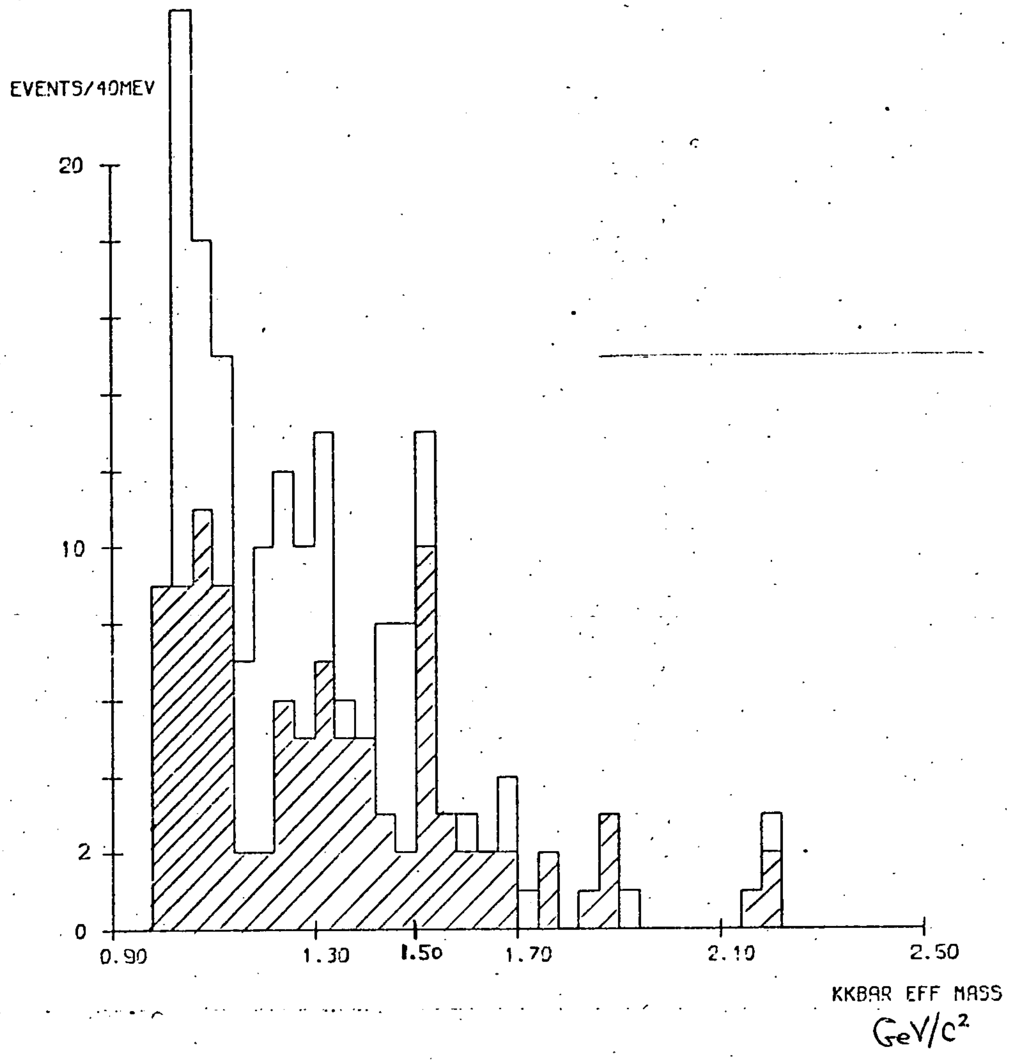

The $K_1^0 K_1^0$ effective mass.

The hatched histogram shows the contribution of the unique events.

There also appears to be some enhancement in the region of 1050 MeV/c^2, perhaps due to the $S^*(1000)$, an S-wave $K\bar{K}$ interaction often found near the threshold of $K\bar{K}$ effective mass spectra. Enhancements in the $K_1^oK_1^o$ effective mass in this region have been reported elsewhere, e.g. by Crennell et al.(5), at a mass of 1068 ± 10 MeV/c^2, with a width, of 80 ± 15 MeV/c^2, and by Alitti et al.(6) at a mass of 1030 ± 10 MeV/c^2, with a width, Γ of 45^{+35}_{-15} MeV/c^2. The effect is attributed to the I = 0 state, since no corresponding effect is found in $K_1^oK^\pm$ states.

4.3.2.3 The f'(1514) meson

The f'(1514) meson was first seen by Barnes et al.(7) in 1965, in the reaction,

$$K^- p \longrightarrow \Lambda^o K^o \bar{K}^o \quad .$$

The mass was reported as ≈ 1500 MeV/c^2, and the width as ≈ 85 MeV/c^2. Furthermore, the absence of any $K_1^oK_2^o$ decay modes limited possible J^P values to 0^+, 2^+, ... etc.

Although there has been little doubt about the mass value of the f', there has been some uncertainty about its width. In 1967, Barnes et al.(8) reported the width as 87 ± 15 MeV/c^2, and Ammar et al.(9) reported a width of only 35 ± 25 MeV/c^2. In 1972, Aguilar-Benitez et al.(10) reported the width as 69 ± 22 MeV/c^2, and Videau et al.(11) reported the width as 40 ± 10 MeV/c^2. The Birmingham-Glasgow collaboration also studied the f'(1514), using mainly K^+K^- states, and estimated the width as 28 ± 15 MeV/c^2 (12).

Looking at the f'(1514) enhancement in Fig. 4.14, for the unique events, the width certainly appears to correspond with that found by the Collaboration from a study of the K^+K^- states.

4.3.2.4 Production Characteristics of the $K_1^oK_1^o$ System

To examine more closely the enhancement in the f'(1514) region, a selection was made on those events where the $K_1^oK_1^o$ effective mass lay in the region,

$$1460 \text{ MeV/c}^2 \leqslant M \leqslant 1580 \text{ MeV/c}^2.$$

The C.M.S. production angle, $\cos\theta^*$, distribution for the $K_1^oK_1^o$ system in the 186 events is shown in Fig. 4.15, with the f'-selected events shown hatched, but there is no striking difference between the two sets of data. This is perhaps not surprising, since the six and seven body final states included naturally give rise to less peripheral distributions of the final state particles.

4.4 Conclusion

There is ample evidence for $K^*(890)$ production and some evidence for $K_N(1420)$ production in the final states,

$$K^+ \pi^+ K^o \Lambda^o \pi^o$$

and $$\pi^+ \pi^+ K^o \Lambda^o K^o$$

as well as evidence for a small amount of $\Sigma(1385)$ production.

In the final states which involve production of a $K_1^oK_1^o$ pair, the effective mass spectrum of this system shows enhancements, indicating production of the f'(1514) meson, and possible production of other meson resonances.

FIG 4.15

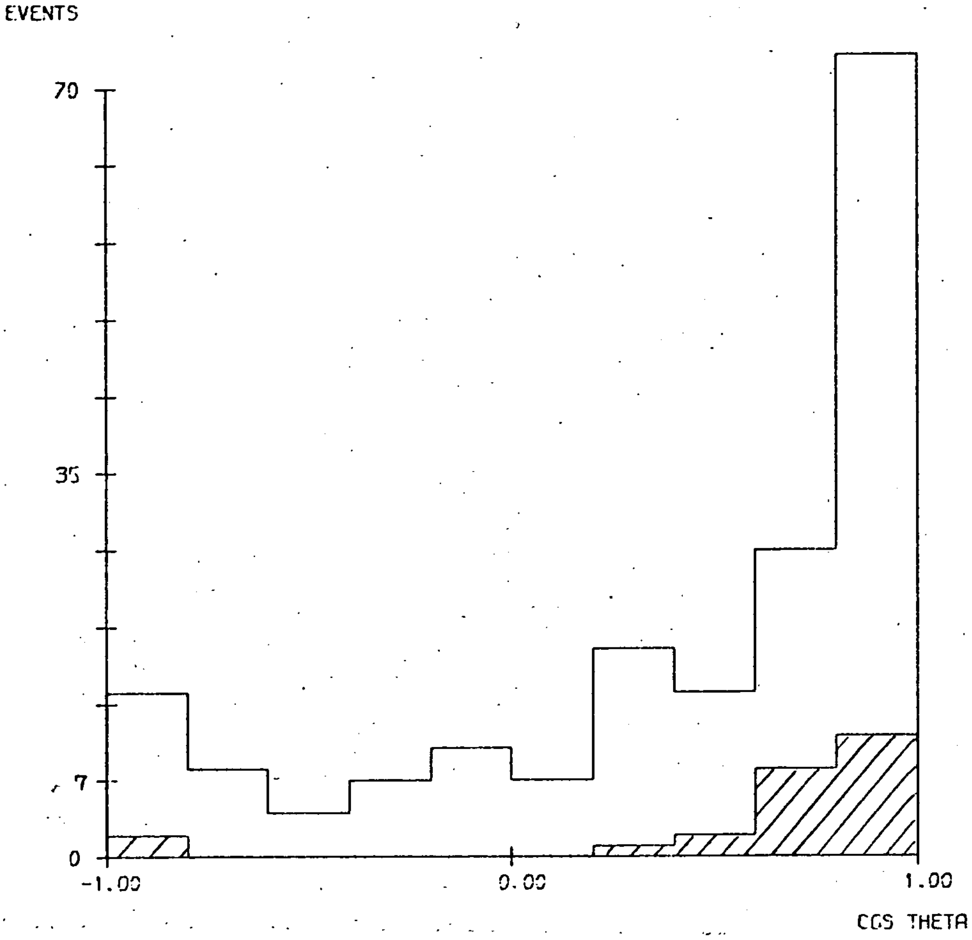

The CMS production angle of the $K_1^o K_1^o$ states (186 events).

The hatched area shows the contribution from events in the f'(1514) region.

4.5 REFERENCES FOR CHAPTER IV

(1) Copley, G., Thesis, Edinburgh University, 1971.

(2) Candlin, D.J., Program 'WEED'. See Ref. (1).

(3) Copley, G., Program 'SEEWEED'. See Ref. (1).

(4) Hemingway, R.J., Thesis, Oxford University, 1968.

(5) Crennell, D.J. et al., Physical Review Letters 16 (1966) 1025.

(6) Alitti, J. et al., Physical Review Letters 21 (1968) 1705.

(7) Barnes, V.E. et al., Physical Review Letters 15 (1965) 322.

(8) Barnes, V.E. et al., Physical Review Letters 19 (1967) 964.

(9) Ammar, R. et al., Physical Review Letters 19 (1967) 1071.

(10) Aguilar-Benitez, M. et al., Physical Review D6 (1972) 29.

(11) Videau, I. et al., Physics Letters 41 B (1972) 213.

(12) Colley, D.C. et al., Nuclear Physics B 50 (1972) 1.

CHAPTER V

'ANTI-HYPERON PRODUCTION'

5.1 Introduction

5.2 Decay Modes of the Anti-Cascade and Anti-Omega Particles

- 5.2.1 The Anti-Cascade Particle,
- 5.2.2 The Anti-Omega Particle

5.3 Anti-Omega Production

- 5.3.1 The First Anti-Omega Candidate
- 5.3.2 Bubble Density
- 5.3.3 Results of Bubble Density Measurements
- 5.3.4 Lifetime of the First Anti-Omega Candidate
- 5.3.5 Conclusions regarding the First Anti-Omega Candidate
- 5.3.6 The Second Anti-Omega Candidate
- 5.3.7 Conclusions regarding the Second Anti-Omega Candidate
- 5.3.8 First Observation of the Anti-Omega

5.4 Anti-Cascade Production

- 5.4.1 Lifetime of the Anti-Cascade States
- 5.4.2.1 Centre of Mass quantities of the Anti-Cascade
- 5.4.2.2 Centre of Mass Production Angle
- 5.4.3 Production Characteristics of the Anti-Cascade in Three-Body Final States
- 5.4.4 The Hexagonal Plot
- 5.4.5 The C.L.A. Parametrisation
- 5.4.6 The Triangular t-Plot

5.5 Conclusions

5.6 References for Chapter V.

CHAPTER V

'ANTI HYPERON PRODUCTION'

5.1 Introduction

The anti-hyperons of major interest were the antiparticles of the cascade particle, Ξ^-, and of the omega minus particle, Ω^-.

Ξ^-, mass = 1321.29 ± 0.14 MeV/c^2

mean lifetime = $(1.672 \pm 0.032) \times 10^{-10}$ S

Ω^-, mass = 1672.5 ± 0.5 MeV/c^2

mean lifetime = $(1.3 \, {}^{+0.4}_{-0.3}) \times 10^{-10}$ S (28 events seen).

The anti-omega, $\overline{\Omega}^+$, had not been detected when the author started this work in 1968, and a certain interest lay in detecting the first occurrence. The $\overline{\Omega}^+$ was in fact first seen in December 1970, in a deuterium experiment(1), and its observation is described later in this chapter.

The reaction requiring the least energy to produce the anti-cascade, $\overline{\Xi}^+$, in K^+P interactions is,

$$K^+P \longrightarrow \overline{\Xi}^+ \, P \, \Lambda^0$$

which requires a C.M.S. energy of 3.375 GeV.

The corresponding reaction for production of the $\overline{\Omega}^+$ is,

$$K^+ \, P \longrightarrow \overline{\Omega}^+ P \, \Xi^0$$

which requires a C.M.S. energy of 3.925 GeV. The total C.M.S. energy available = 4.46 GeV.

5.2 Decay Modes of the Anti-Cascade and Anti-Omega Particles

5.2.1 The Anti-Cascade Particle

The main ($\sim 100^{\circ}/\text{o}$) decay mode of the $\overline{\Xi}^+$ is,

$$\overline{\Xi}^+ \longrightarrow \overline{\Lambda}^0 \pi^+ \qquad P_{Max} = 139 \text{ MeV/c}$$

where P_{Max} gives the maximum momentum of either particle in the $\overline{\Xi}^+$ centre of mass.

The $\overline{\Lambda}^0$ may decay to $\bar{P}\pi^+$ or $\bar{n}\pi^0$, and if the $\overline{\Lambda}^0$ decay is seen in the chamber, it is often possible to say at the scanning stage whether the $\overline{\Lambda}^0$ originated at the charged decay vertex, since the antiproton, $\bar{P}$, follows very closely the line of flight of the $\overline{\Lambda}^0$, in the same way that the $\overline{\Lambda}^0$ follows very closely the line of flight of the $\overline{\Xi}^+$. A good example of this is shown in Plate II, a photograph of one example of the reaction,

$$K^+P \longrightarrow \overline{\Xi}^+ X^+ \text{ (MMS)}$$
$$\hookrightarrow \overline{\Lambda}^0 \pi^+$$
$$\hookrightarrow \bar{P}\pi^+$$

where the anti-proton clearly points directly at the charged decay vertex. A summary of the parameters of the tracks involved is given in Table 5.1. If the charged prong from the interaction is assumed to be a proton then the calculated value of the missing mass is 1.966 GeV/c^2.

The lifetime of the $\overline{\Xi}^+$ state shown is

$$\tau = (2.16 \pm 0.29) \times 10^{-10} \text{ s.}$$

TABLE 5.1

Parameters of Tracks shown in Plate II

Track Number		Momentum (GeV/c)	Length (cm)	Dip (degrees)
1.	(Beam)	10.084 ± 0.100	17	- 0.2
2.		3.196 ± 0.030	109	0.9
3.	($\bar{\Xi}^+$)	3.224 ± 0.435	15.8	- 3.4
4.	(π^+)	0.532 ± 0.010	65	-14.6
5.	($\bar{\Lambda}^0$)	2.81	12.7	- 1.2
6	($\bar{P}$)	2.435 ± 0.030	66	- 2.2
7	(π^+)	0.377 ± 0.004	55	5.3

5.2.2 The Anti-Omega Particle

The three decay modes of the $\bar{\Omega}^+$, corresponding to known decay modes of the Ω^- are,

(i) $\bar{\Omega}^+ \longrightarrow \bar{\Xi}^0 \pi^+$, $\bar{\Xi}^0 \longrightarrow \bar{\Lambda}^0 \pi^0$ $\qquad$ P_{Max} = 294 MeV/c

(ii) $\bar{\Omega}^+ \longrightarrow \bar{\Xi}^+ \pi^0$, $\bar{\Xi}^+ \longrightarrow \bar{\Lambda}^0 \pi^+$ $\qquad$ P_{Max} = 290 MeV/c

(iii) $\bar{\Omega}^+ \longrightarrow \bar{\Lambda}^0 K^+$ $\qquad$ P_{Max} = 211 MeV/c

In decay (i) above, the neutral decay of the $\bar{\Xi}^0$ means that such a decay mode would be difficult to fit kinematically, since the position of the neutral decay vertex is unknown. (The mean lifetime of the $\bar{\Xi}^0$ is $\sim$ 3×10^{-10} S).
In decay (ii) above, for an $\bar{\Omega}^+$ produced with a momentum $\approx$ 3 GeV/c, the maximum decay angle $\approx$ 6°. For an $\bar{\Omega}^+$

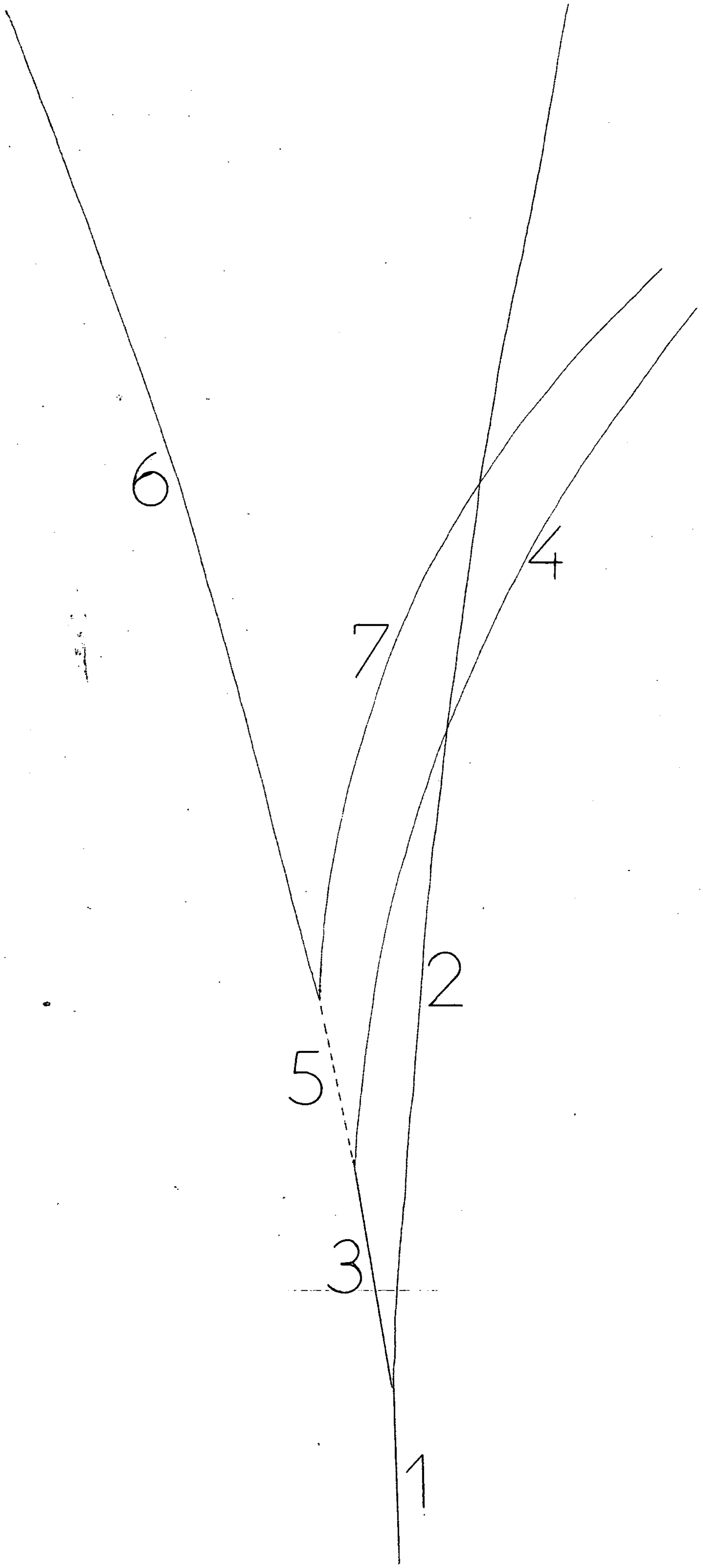
6
4
7
2
5
3
1

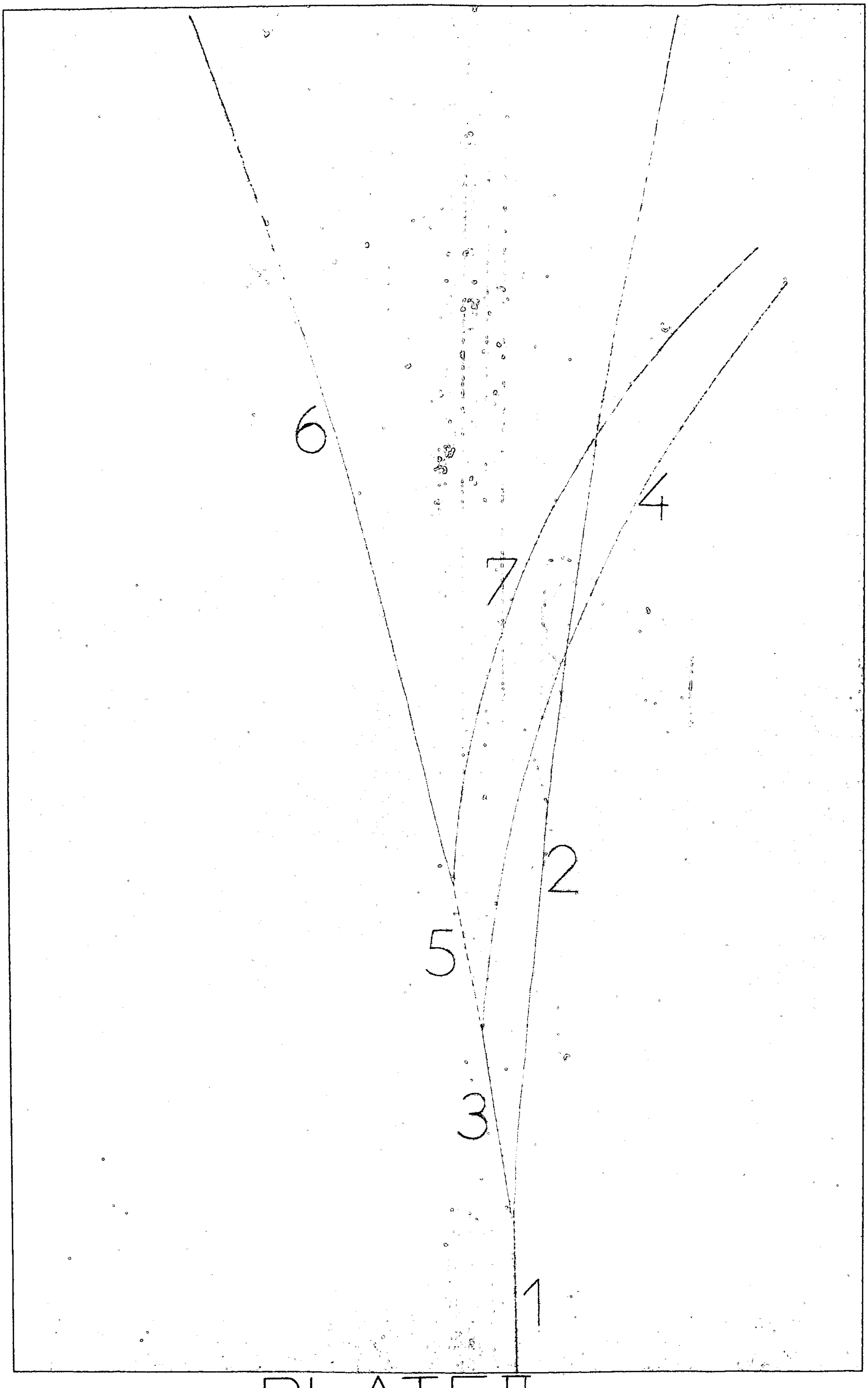

PLATE II

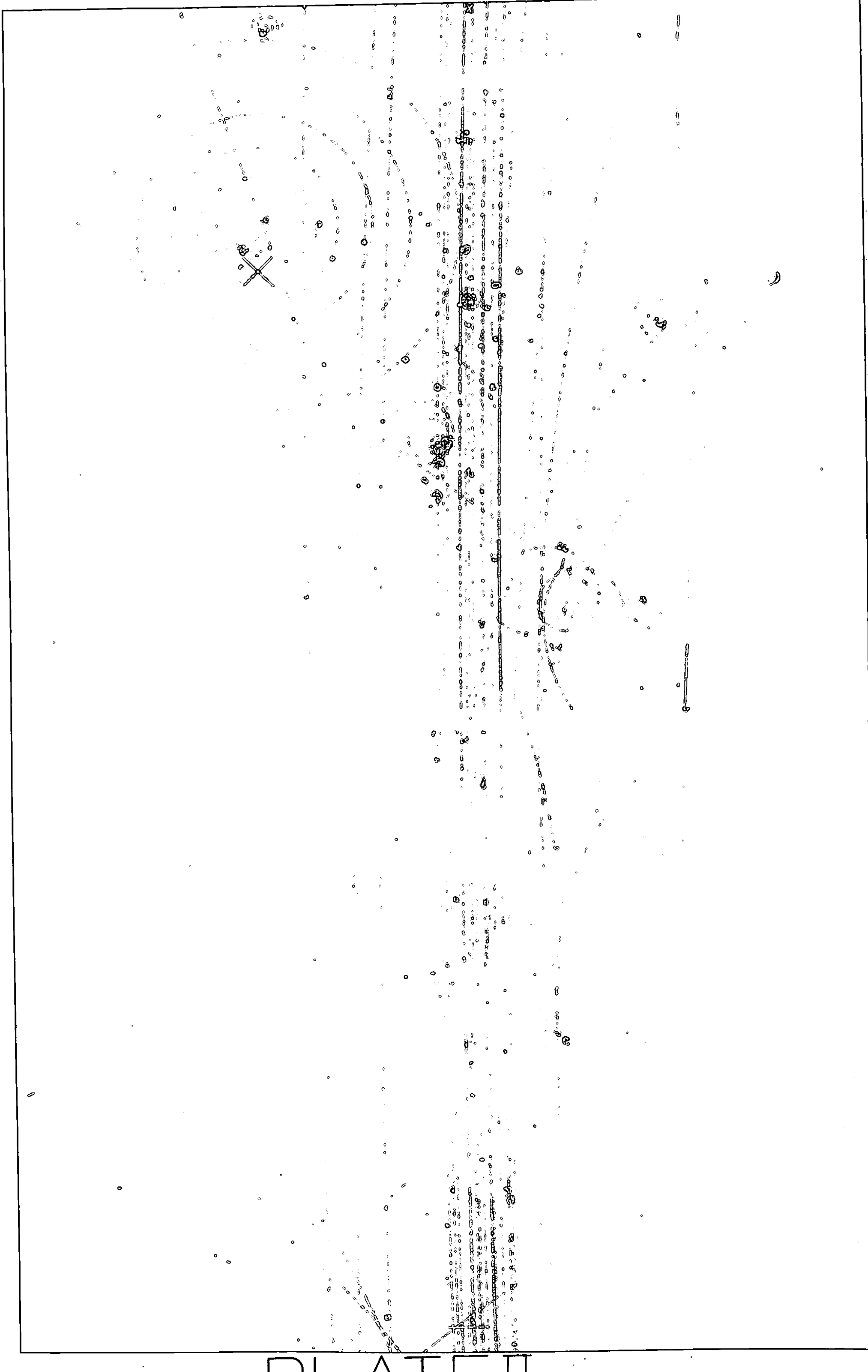

PLATE II

produced with a momentum $\approx$ 5 GeV/c, the maximum decay angle $\approx 4^\circ$.

5.3 Anti-Omega Production

The cross-section for $\overline{\Omega}^+$ production in K^+D interactions at 12 GeV/c was estimated from the observation of one event$^{(1)}$ as 0.1 μb. If the K^+P cross-section at 10 GeV/c for $\overline{\Omega}^+$ production is of the same order, then the Edinburgh-Birmingham-Oxford film sample, with a combined total cross-section of 16 events/μb, might be expected to contain one or two $\overline{\Omega}^+$ events. However, there are many ways in which such events may be lost, or may fail to be unambiguously identifiable.

No event was found in this experiment which could be uniquely interpreted as involving the production of the $\overline{\Omega}^+$ particle. However, two events which were considered to be possible candidates for $\overline{\Omega}^+$ production will now be described.

5.3.1 The First Anti-Omega Candidate

A photograph of this event is shown in Plate III and details of the tracks involved are given in Table 5.2. The topology is of the 211-type, and when this event was first processed, two kinematic fits giving good chi-squared probabilities were obtained, viz.

$$\begin{array}{l} K^+ P \longrightarrow \overline{\Omega}^+ \pi^+ \Lambda^o \ (\Lambda^o) \qquad\qquad (1) \\ \qquad\qquad\qquad\quad \hookrightarrow P\pi^- \\ \qquad\qquad\quad \hookrightarrow K^+ (\overline{\Lambda}^o) \end{array}$$

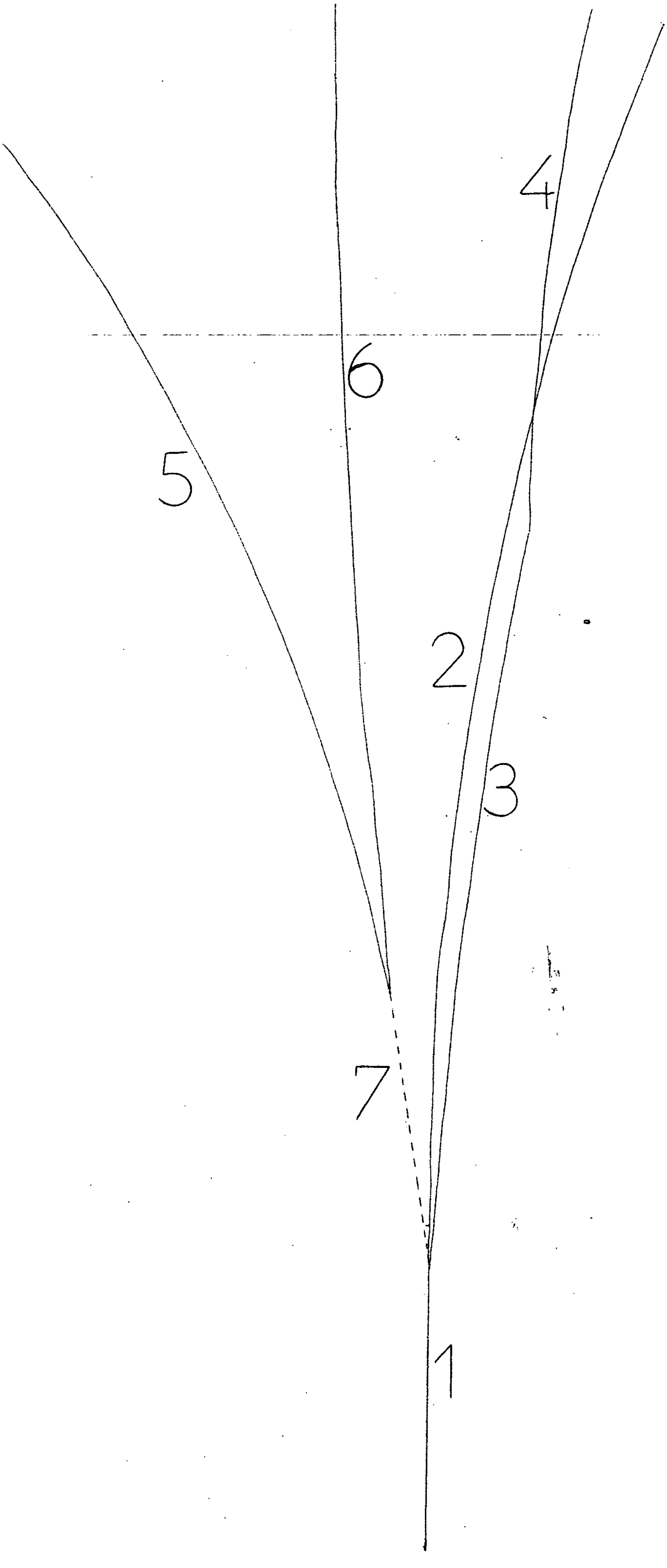
4
6
5
2
3
7
1

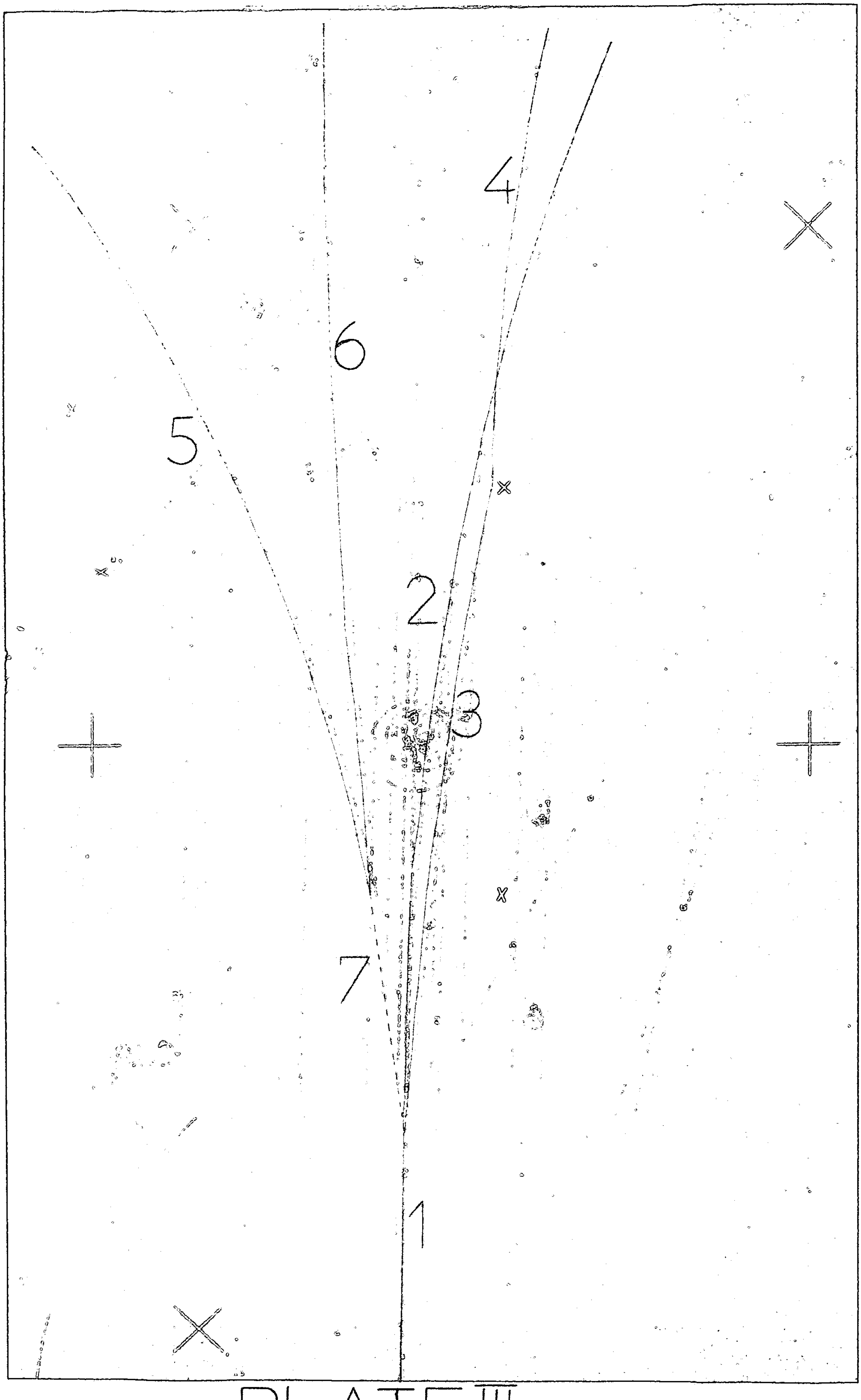

PLATE III

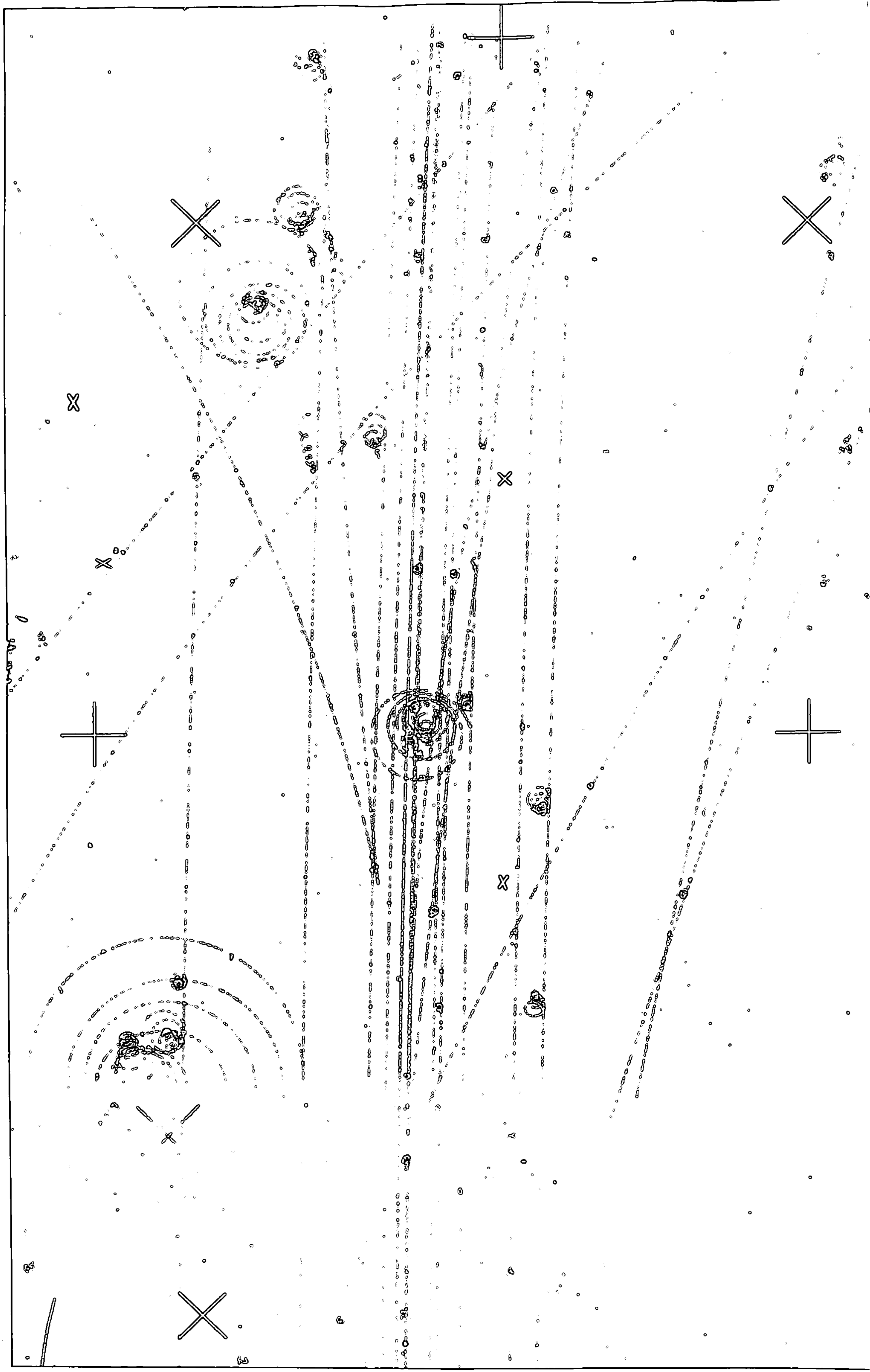

PLATE III

$$\begin{array}{l} K^+P \longrightarrow \overline{\Omega}^+\pi^+\Lambda^0\,(\Lambda^0) \\ \qquad\qquad\quad \llcorner\!\!\longrightarrow P\pi^- \\ \qquad\quad \llcorner\!\!\longrightarrow \pi^+(\overline{\Xi}^0) \end{array} \qquad (2)$$

The calculated value for the missing mass of the unseen Λ^0 was low, i.e.

$$1.061 \pm 0.043 \text{ GeV/c}^2 \quad \text{for fit (1)}$$

$$1.030 \pm 0.052 \text{ GeV/c}^2 \quad \text{for fit (2)}$$

The event had failed to fit any other hypothesis tried in the kinematics decks, and the 1C fit at the charged decay vertex would not fit the decay of Σ^+, $\overline{\Sigma}^+$, or $\overline{\Xi}^+$. The fitted momentum of the decaying track was 3.186 ± 0.114 GeV/c, corresponding to a bubble density of 1.29 ± 0.02, if the track was made by an $\overline{\Omega}^+$ particle. The event was remeasured in Glasgow University, by eleven different operators, to test if the same hypothesis would fit the new measurements. In all eleven subsequent measurements, very poor fits were obtained to hypotheses (1) and (2), and no other fits were obtained. (The values given in Table 5.2 are the averages of these measurements). At a later stage, the event was measured four times in Edinburgh on the 'Vanguard' measuring machine, with the same results.

Closer examination revealed that the original measurement had been a poor one, the measurement errors being more than double those of subsequent measures. This also gave rise to large errors on the momenta of the tracks, and it is reasonable to suppose that it was these large errors which gave rise to the low values of χ^2 obtained for hypotheses (1) and (2) on the first measurement.

TABLE 5.2

Parameters of Tracks shown in Plate III

Track Number	Momentum (GeV/c)	Length (cm)	Dip (degrees)
1 (beam)	10.076 ± 0.100	45	0.3
2 (π^+)	0.857 ± 0.1	51	1.9
3	3.012 ± 0.090	36.8	6.9
4	1.147 ± 0.033	24	-1.2
5 (π^-)	0.453 ± 0.009	29	-23.8
6 (P)	2.727 ± 0.058	39	-10.2
7 (Λ^0)	3.095 ± 0.048	13	-12.8

However, it was also true that if one considered the charged decay vertex alone, the only decay sequences which could give a fit were,

$\overline{\Omega}^+ \rightarrow \overline{\Lambda}^0 K^+$ $\quad P_{Max} = 211$ MeV/c

$\overline{\Omega}^+ \rightarrow \overline{\Xi}^0 \pi^+$ $\quad P_{Max} = 290$ MeV/c

$K^+ \longrightarrow \pi^+\pi^0$ $\quad P_{Max} = 205$ MeV/c

$K^+ \longrightarrow \mu^+\nu$ $\quad P_{Max} = 236$ MeV/c

The transverse momentum at the decay vertex was 135 ± 3 MeV/c.

If the decaying track was an $\overline{\Omega}^+$, its expected bubble density = 1.29 ± 0.02 and if it was a K^+, its expected bubble density = 1.03.

For the track leaving the charged decay vertex, if it was a K^+, its bubble density would be 1.21 ± 0.01 and for a π^+ or μ^+, 1.01.

Since the decaying track was ~ 37 cm long in the chamber, and its decay product was ~ 25 cm long, it seemed that it might be possible to use bubble density estimation as a means of establishing the identity of the tracks involved.

5.3.2 Bubble Density

The term 'bubble density' is usually understood to refer to the number of bubbles created by a track, per unit length, expressed as a ratio of the number created by a minimum ionising track, such as a beam track. In this experiment, a beam track created ~ 15 bubbles/cm. The number of bubbles created per unit length depends only on the charge and velocity, $\beta = v/c$, of the particle, and not on its mass. If g_o = number of bubbles created per unit length, then

$$g_o \propto \frac{1}{\beta^n}$$

where $n \approx 2.0$(2,3). Usually n is taken $= 2.0$, and since for the beam tracks, $\beta \approx 1.0$, then the relative bubble density of a track, g_R say, is

$$g_R = \frac{1}{\beta^2}$$

where $\beta = v/c$ for the ionising particle. This quantity, g_R is the one printed in the Kinematics output, under the column headed, 'ION'. If the track has a dip angle, δ, then the bubble density becomes

$$g_R' = g_R \sec \delta$$

although this assumption may be unreliable for angles of dip $\gtrsim 30^\circ$.

Values of $^1/\beta^2$ at different momenta for the pion, kaon and proton, are shown plotted in Fig. 5.1. Normally the lower limit for visual estimates of bubble density is taken as 1.5, corresponding to a momentum of 200 MeV/c for $\pi^\pm$, 700 MeV/c for $K^\pm$, and 1.3 GeV/c for a proton.

There are normally gaps between the bubbles, and the number of gaps = number of bubbles. It is expected theoretically, and has been verified experimentally(3,4) that the distribution of gaps in a track is exponential. i.e. if x = gap length, from bubble centre to bubble centre, greater than some minimum length, 'a' say,

and if ℓ = length of track,

and if g_o = mean number of bubbles/unit length,

then(5) the number of gaps greater than x,

$$n\,(>x) = g_o\,\ell\, e^{-g_o x} .$$

If the gap is measured between the circumferences of the 'bubbles' on film then the gap becomes x', where

$$x = x' + a_o$$

and a_o = one bubble diameter,

$$\text{and} \quad n\,(>x) = g_o\,\ell\, e^{-g_o x'} \cdot e^{-g_o a}$$

$$= \text{constant} \times e^{-g_o x'} .$$

Thus, if one uses a travelling microscope to measure the gaps on film, and sorts the gaps into bins of length ℓ_o (i.e. the

FIG 5.1

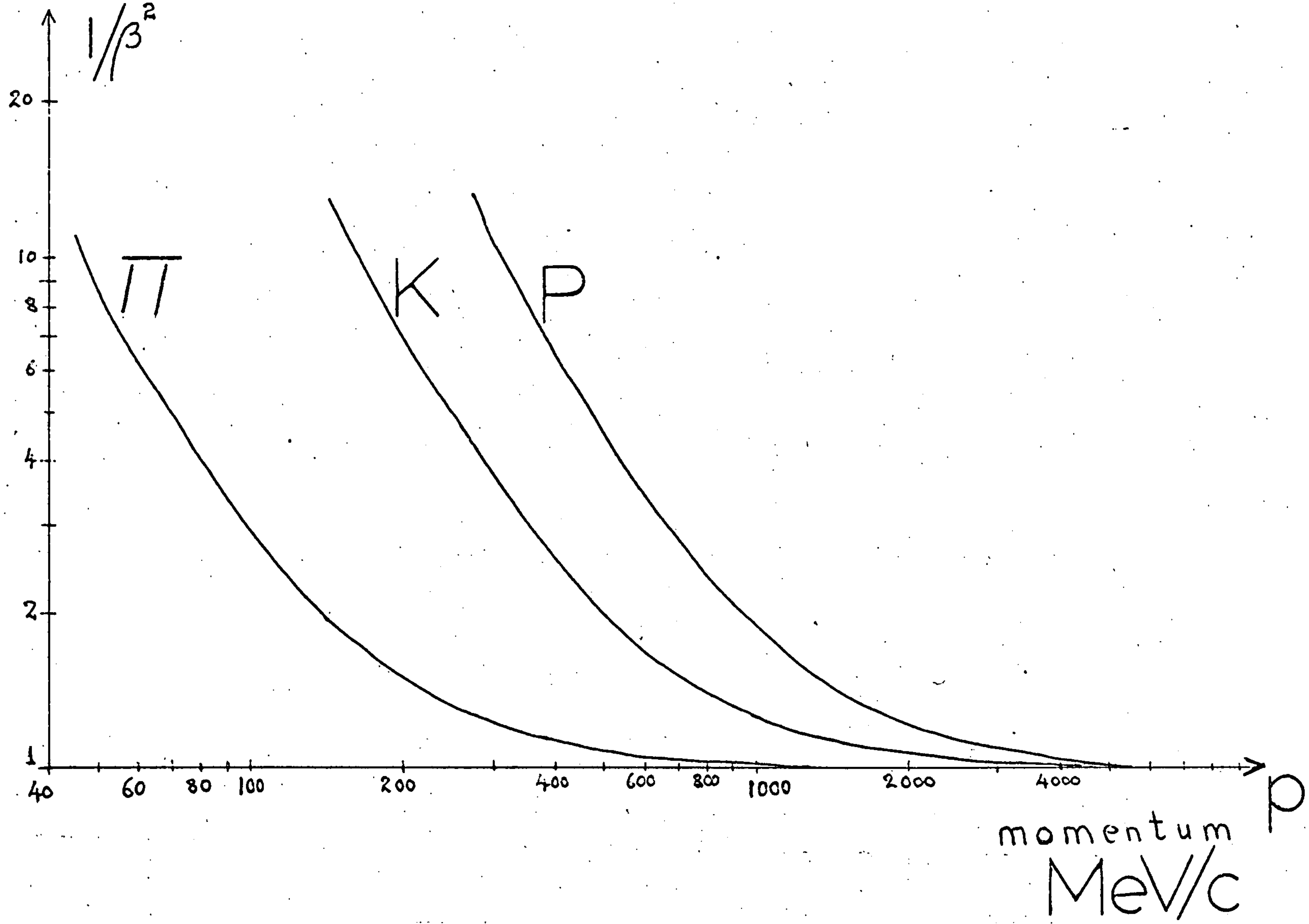
$1/\beta^2$
20
10
8
6
4
2
1
40
60
80
100
200
400
600
800
1000
2000
4000
π
K
P
p
momentum
MeV/c

bins are $(a, a + \ell_o)$, $(a + \ell_o, a + 2\ell_o)$, ... etc.) one can plot log n against gap size, x', and the gradient of the straight line will give a value for g_o. By comparing the gradient of this line with that of the beam tracks, a value for g_R may be deduced. This was the method used by the author to measure g_R for the decaying track.

5.3.3 Results of Bubble Density Measurements

The unit chosen for bin size in sorting the gaps was 25 μm on film (~ one 'bubble' diameter) and the gaps were sorted into bins of size $2 \longrightarrow 8$ units. A least-squares fit was made to each set of points, and the error was taken as $^1/\sqrt{N}$ where N = total number of gaps measured (~ 100 on each measure). The decaying track was measured seven times by different workers, giving a mean gradient, m_1, of

$$m_1 = -0.672 \pm 0.075 .$$

The mean value of the gradient for four beam tracks in the vicinity of the decaying track was m_2 where

$$m_2 = -0.636 \pm 0.08,$$

giving a relative bubble density, g_R, for the decaying track of

$$g_R = 1.06 \pm 0.19 .$$

Obviously, the error is large enough to allow the ionisation to correspond to a K^+ meson or an $\overline{\Omega}^+$. Fig. 5.2 shows the results of a single measurement on the decaying track, together with the results of a single measurement on a nearby beam track.

At a later stage, the tracks were remeasured, using a different objective and values of g_R were obtained ranging from

FIG 5.2

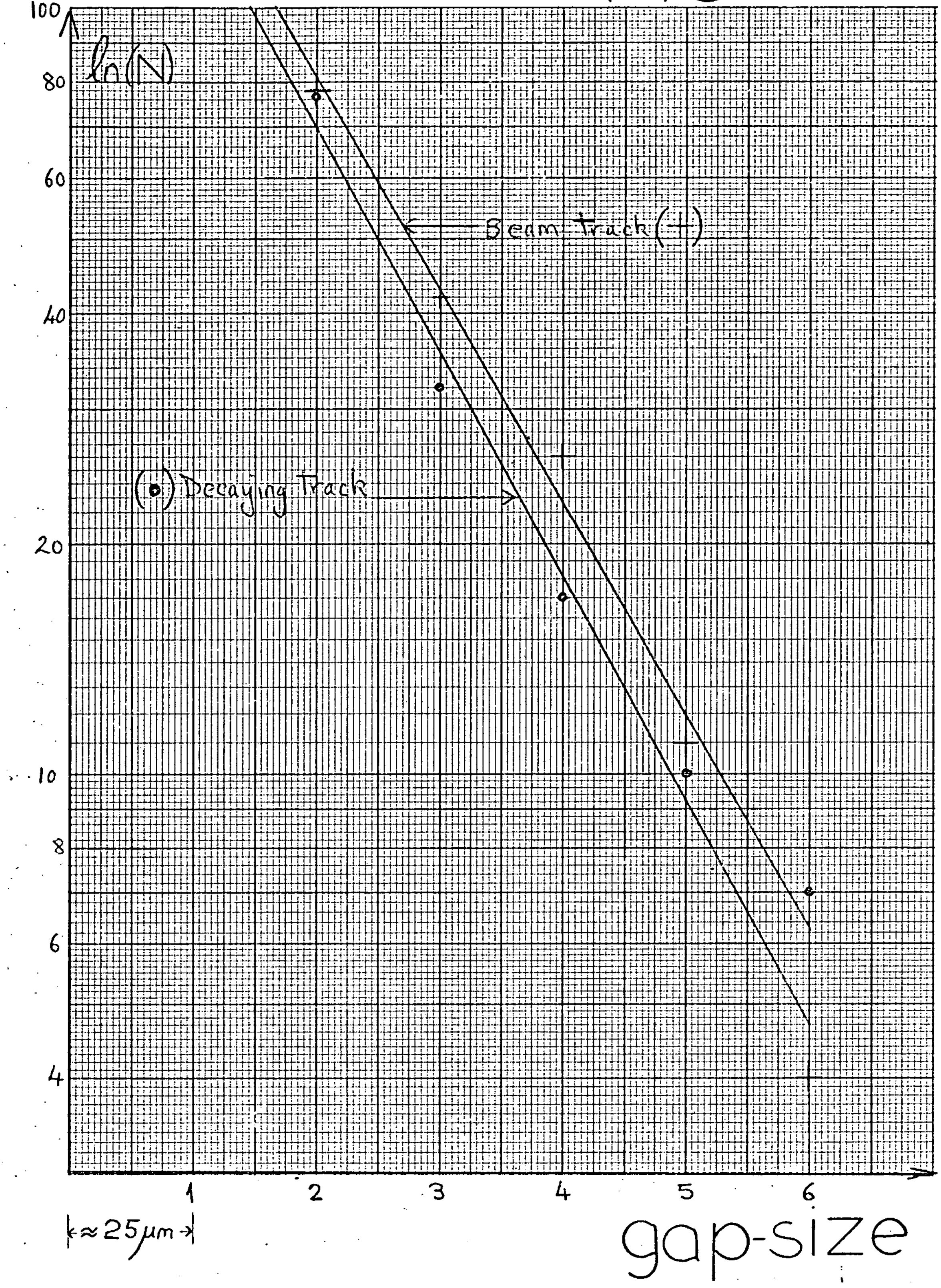

Results of bubble-density measurements on the first anti-omega candidate. The lines shown have a relative gradient of 1.06.

$$g_R = 1.47 \pm 0.21$$

to $$g_R = 1.08 \pm 0.16 .$$

Since the error on estimated bubble density was too large to allow any distinction between meson and hyperon for the decaying track, and since it was found difficult to obtain a consistent value for g_R, the bubble density measurements were not pursued further.

5.3.4 Lifetime of the First Anti-Omega Candidate

Using the decaying-track length of 36.80 cm, and fitted momentum of 3.200 ± 0.075 GeV/c, the decay time of the state was estimated, assuming the particle to be an $\overline{\Omega}^+$, as

$$\tau = (6.42 \pm 0.15) \times 10^{-10}\ \mathrm{s}$$

compared with the Ω^- mean lifetime of

$$\tau = (1.3 \begin{smallmatrix} +\ 0.4 \\ -\ 0.3 \end{smallmatrix}) \times 10^{-10}\ \mathrm{s} .$$

If one assumes that the particle is actually a K^+ meson, then the decay time is

$$\tau = (1.89 \pm 0.04) \times 10^{-10}\ \mathrm{s}$$

compared with the mean lifetime of the K^+ meson of

$$\tau = (1.24 \times 10^{-8}\ \mathrm{s}.$$

This implies that if the decaying particle is in fact an $\overline{\Omega}^+$, its decay time is unusually long.

It is also true that any hypothesis of $\overline{\Omega}^+$ production in this event requires that both the Λ° from the interaction and the $\overline{\Lambda}^\circ$ from the decay vertex (or from the $\overline{\Xi}^\circ$ decay), be unseen, which by itself is not excessively improbable, but together with other factors, is evidence against anti-hyperon production.

5.3.5 Conclusions Regarding the First Anti-Omega Candidate

This event was discarded as a likely candidate for $\overline{\Omega}^+$ production for the following reasons:

(i) Remeasurement gave high values of χ^2 for the hypotheses.

(ii) The calculated value of the missing mass of the Λ^o from the interaction was very low (mean value from the eleven measurements = 1048 ± 27 MeV/c^2).

(iii) It was not possible to establish the identity of the tracks by bubble density measurements.

(iv) From lifetime considerations, the $\overline{\Omega}^+$ interpretation is less likely.

(v) The $\overline{\Omega}^+$ interpretation requires both Λ^o and $\overline{\Lambda}^o$ to be unseen.

(vi) There are other possible interpretations of the event, allowing multi-neutral production at the primary vertex. It was found impossible to fit any reaction to the event, and the author considers that the most likely interpretation is due to the reaction,

$$\begin{tikzcd} K^+P \arrow[r] & K^+ \arrow[d] & K^+ & \Lambda^o \arrow[d] & (n \times \pi^o) \\ & \mu^+\nu & & P\pi^- & \end{tikzcd} .$$

The calculated missing mass for this reaction is ≈ 1.7 GeV/c^2.

5.3.6 The Second Anti-Omega Candidate

This event is of the 211-type topology, and a sketch of the event is shown in Fig. 5.3. The length and momentum of the tracks involved are given in Table 5.3.

FIG 5.3

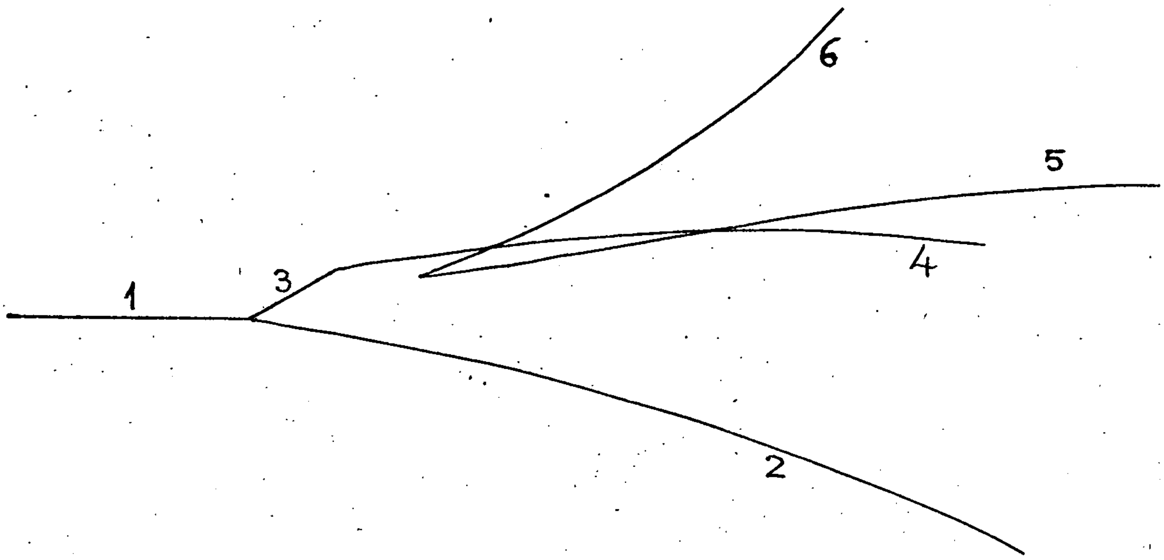

Sketch of the tracks of the second anti-omega candidate.

The decaying track was only 0.98 cm long, so its momentum was unknown. The V^0 gave a good fit to,

$$\Lambda^0 \longrightarrow P\,\pi^-$$

and four fits were obtained at the interaction vertex, viz.

$$\begin{array}{l} K^+P \longrightarrow \Lambda^0\ \overline{\Sigma}^+ K^+\ (n) \\ \qquad\qquad\quad \llcorner\!\!\rightarrow \bar{n}\ \pi^+ \end{array}$$

$$\begin{array}{l} K^+P \longrightarrow \Lambda^0\ \overline{\Sigma}^+ P\ (K^0) \\ \qquad\qquad\quad \llcorner\!\!\rightarrow \bar{n}\ \pi^+ \end{array}$$

$$\begin{array}{l} K^+P \longrightarrow \Lambda^0\ \overline{\Omega}^+ \pi^+\ (\Lambda^0) \\ \qquad\qquad\quad \llcorner\!\!\longrightarrow \pi^+\ (\overline{\Xi}^0) \end{array}$$

$$\begin{array}{l} K^+P \longrightarrow \Lambda^0\ \overline{\Omega}^+ \pi^+\ (\Lambda^0) \\ \qquad\qquad\quad \llcorner\!\!\longrightarrow K^+\ (\overline{\Lambda}^0)\ . \end{array}$$

The same results were obtained on remeasurement. If track 2 is a proton, its bubble density would be 1.34, at the limit for measurement.

TABLE 5.3

Parameters of Tracks shown in Fig. 5.3

Track Number	Momentum (GeV/c)	Length (cm)
1	10.076 ± 0.100	9
2	1.615 ± 0.021	63
3	-	0.98
4	1.272 ± 0.018	55
5	2.090 ± 0.039	51
6	0.529 ± 0.008	43

The transverse momentum at the charged decay vertex is $\approx$ 160 MeV/c.

Assuming that the decaying particle is a $\overline{\Sigma}^+$, the decay time is,

$$\tau = 0.075 \times 10^{-10}\ \mathrm{s}$$

compared with the Σ^- mean lifetime of

$$\tau = 1.48 \times 10^{-10}\ \mathrm{s}\ .$$

If one assumes that the decaying particle is an $\overline{\Omega}^+$, the decay time is,

$$\tau = 0.17 \times 10^{-10}\ \mathrm{s}\ .$$

Both of these decay times are acceptable.

5.3.7 Conclusions Regarding the Second Anti-Omega Candidate

As with the previous event, if one interprets this event as being due to the production of an $\overline{\Omega}^+$ particle, one has to assume that both the Λ^0 from the interaction and the $\overline{\Lambda}^0$, are unseen.

However, in the absence of other evidence, it is possible that this event is an example of the production and decay of the $\overline{\Omega}^+$ particle.

5.3.8 First Observation of the Anti-Omega

The $\overline{\Omega}^+$ was first observed in December 1970, in a K^+D experiment, by A. Firestone et al.(1), at the Lawrence Radiation Laboratory.

The reaction was,

$$\begin{tikzcd}[column sep=small]
K^+D \arrow[r] & \overline{\Omega}^+ \arrow[ddr] & \Lambda^0 \arrow[dr] & \Lambda^0 p\, \pi^+ \pi^- \\
 & & & p\pi^- \\
 & & \overline{\Lambda}^0 \arrow[dr] & K^+ \\
 & & & \bar{p}\, \pi^+
\end{tikzcd}$$

where one Λ^0 was unseen. The attempt to fit the $\overline{\Lambda}^0$ to the charged decay vertex as

$$\overline{\Xi}^+ \longrightarrow \overline{\Lambda}^0 \pi^+$$

failed completely, giving an unconstrained mass value for the $\overline{\Xi}^+$ of 1430.4 ± 2.6 MeV/c^2, far removed from its true value of 1321 MeV/c^2. Interpreting the decay as

$$\overline{\Omega}^+ \longrightarrow \overline{\Lambda}^0 K^+$$

resulted in a fitted mass value for the decaying particle of 1673.1 ± 1.0 MeV/c^2, which is in excellent agreement with the known mass of the Ω^-, 1672.5 ± 0.5 MeV/c^2. The track from the decay had a momentum of 866 ± 8 MeV/c which should have a bubble density for a K^+, of 1.3, i.e. at the limit of identification and being consistent with the observed ionisation.

The certainty with which this event was established as the decay of an anti-omega particle was due largely to the transverse momentum of the decay, viz. $\approx$ 210 MeV/c, compared with the maximum transverse momentum for the decay, $\overline{\Xi}^+ \longrightarrow \overline{\Lambda}^0 \pi^+$ of 139 MeV/c. The length of the decaying track was too short to allow an estimate of momentum by measurement.

The cross-section for anti-omega production at this momentum was estimated by the authors to be $\approx$ 0.1 μb. It is interesting to note that this result was based on 500,000 pictures in which 45 $\overline{\Xi}^+$ events were observed, very similar to the combined

Edinburgh-Birmingham data.

5.4 Anti-Cascade Production

The results presented in the following sections involve a total of 34 final states containing an $\overline{\Xi}^+$ particle from the combined Edinburgh-Birmingham data, and part of these results has already been published$^{(6)}$, along with the cross-sections calculated in Chapter III. Because of the mass and strangeness of the $\overline{\Xi}^+$, and the fact that it must be produced along with two other baryons, its production cross-section is low, and the data published from this experiment represent a significant contribution to the world data on $\overline{\Xi}^+$ production characteristics. The total $\overline{\Xi}^+$ production cross-section was estimated as $(21 {}^{+6}_{-4})$ μb.

5.4.1 Lifetime of the Anti-Cascade States

Using the method of Maximum Likelihood as described in Chapter III, the mean lifetime of thirteen $\overline{\Xi}^+$ events found in the Edinburgh data was estimated as,

$$\tau = (1.64 {}^{+\,0.4}_{-\,0.3}) \times 10^{-10}\ \mathrm{s}$$

and when these events were combined with the Birmingham events, the lifetime was estimated as

$$\tau = (1.55 {}^{+\,0.35}_{-\,0.20}) \times 10^{-10}\ \mathrm{s}.$$

The 1973 Particle Data Tables give the lifetime of the Ξ^- as

$$\tau = (1.672 \pm 0.032) \times 10^{-10}\ \mathrm{s}$$

in good agreement.

The Likelihood Function, $\mathcal{L}$, for the Edinburgh $\overline{\Xi}^+$

FIG 5.4

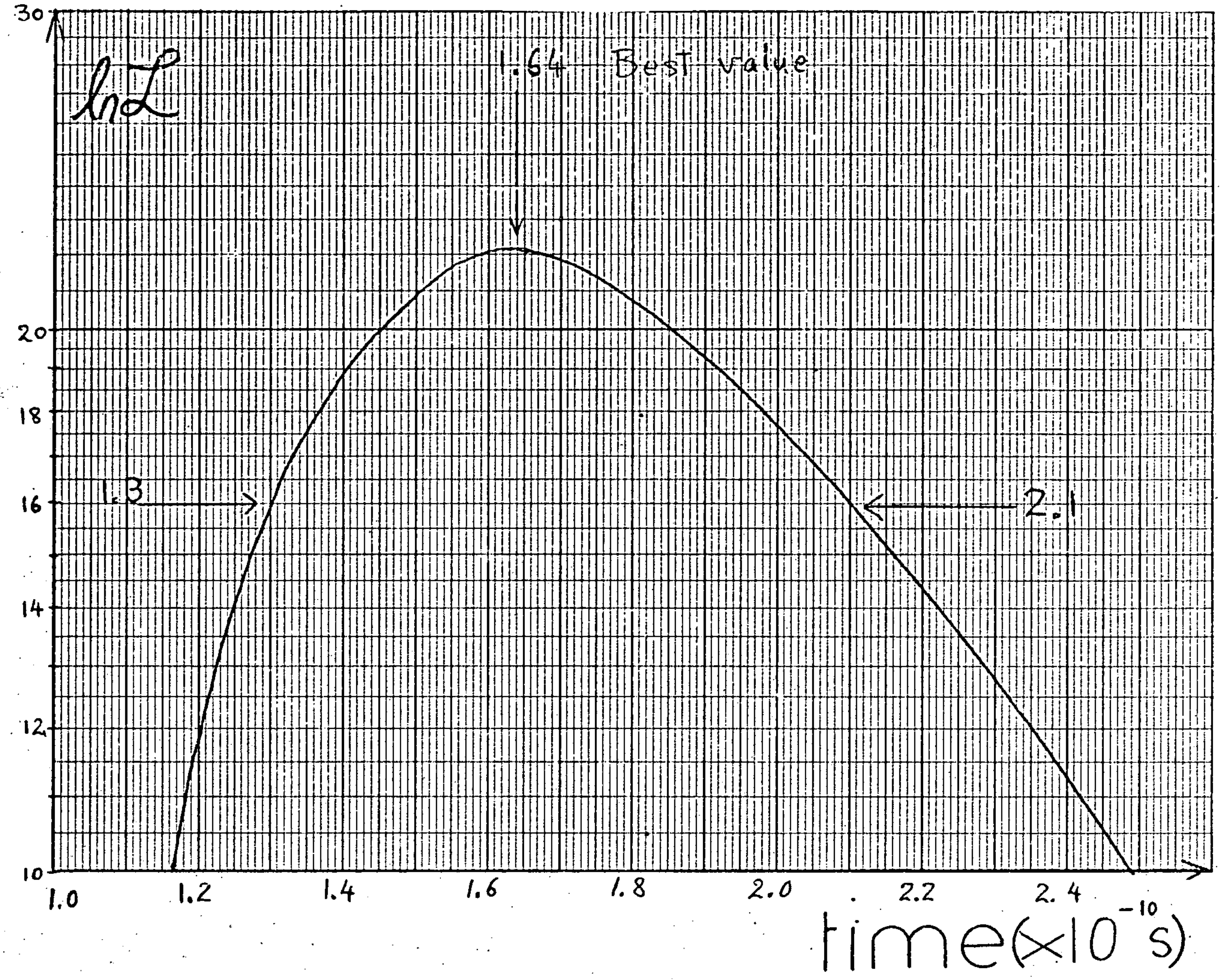

Likelihood function for the lifetime of the anti-cascade events found in the Edinburgh data.

events is shown plotted in Fig. 5.4. The asymmetric nature of the uncertainty is clear.

5.4.2 Centre of Mass Quantities of the Anti-Cascade

5.4.2.1 Centre of Mass Momentum

In Figs. 5.5, 5.6, 5.7 and 5.8 respectively are shown the Peyrou Plots for the 37 Ξ^+ states on the DST, in the 3-, 4- and 5-body final states, and the sum of these. The Peyrou Plot gives the C.M.S. longitudinal momentum, $P^*_{\parallel}$, along the x-axis, and the transverse momentum, $P^*_{\perp}$, along the y-axis.

It is clear from these figures that the Ξ^+ states produced in the 3-body final states are more sharply peaked forwards than are those in the 4- and 5-body final states.

5.4.2.2 Centre of Mass Production Angle

Fig. 5.9 shows the distribution in cos θ^*, the C.M.S. production angle, for the Ξ^+ states, defined with respect to the incident K^+ meson. Naturally, these distributions contain much the same information as the Peyron Plots. Fig. 5.10 shows the angular correlations between the nucleon and hyperon produced in 3 body final states of the type,

$\Xi^+ PY$, where Y is a Λ^0 or Σ^0 hyperon.

The Y-hyperon is clearly peaked backwards in the C.M.S. and the proton peaked backwards and forwards. The peaked nature of the angular distributions leads one to suppose that some sort of peripheral process may be active in 3-body production, and it was decided to investigate further the possible production mechanisms in these states.

FIG 5.5

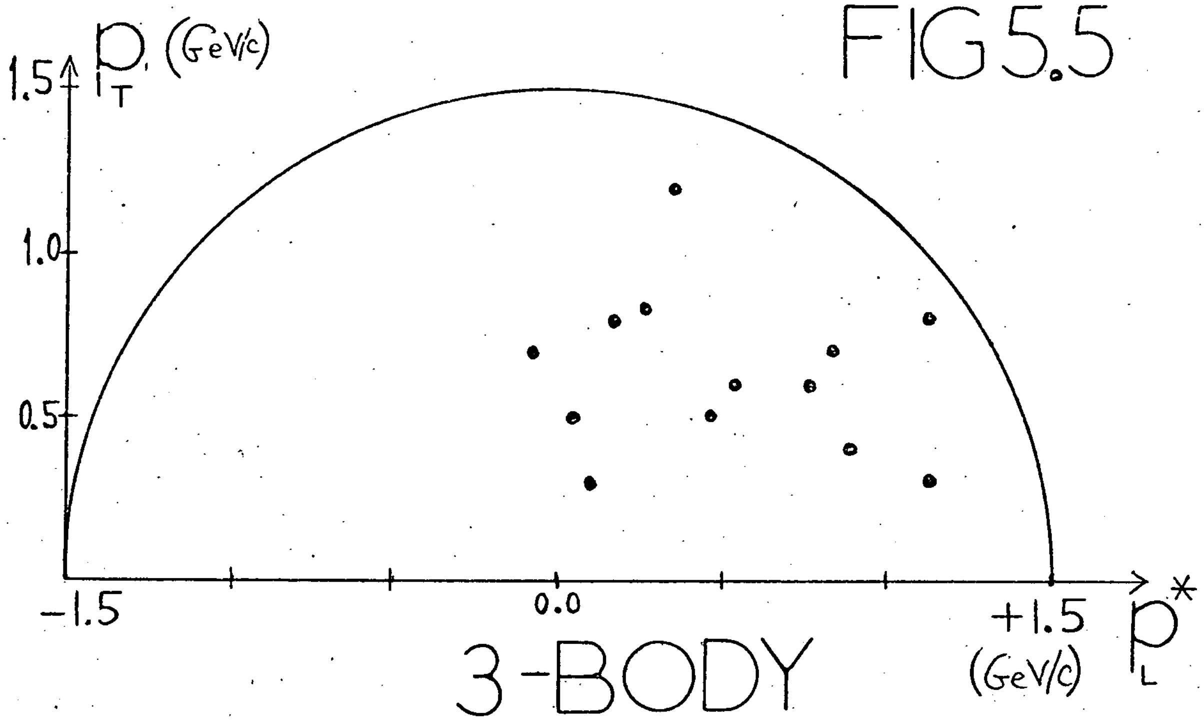

FIG 5.6

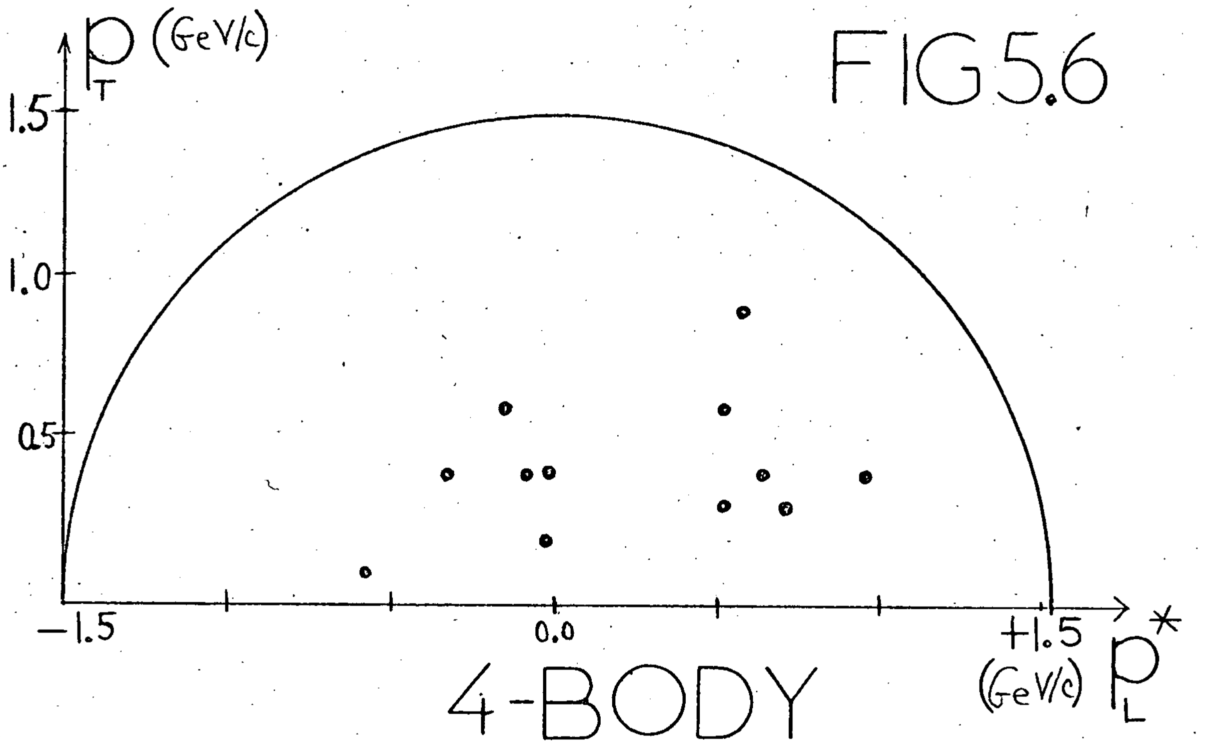

Peyrou plots of $\bar{\Xi}^{\pm}$ final states.

FIG 5.7

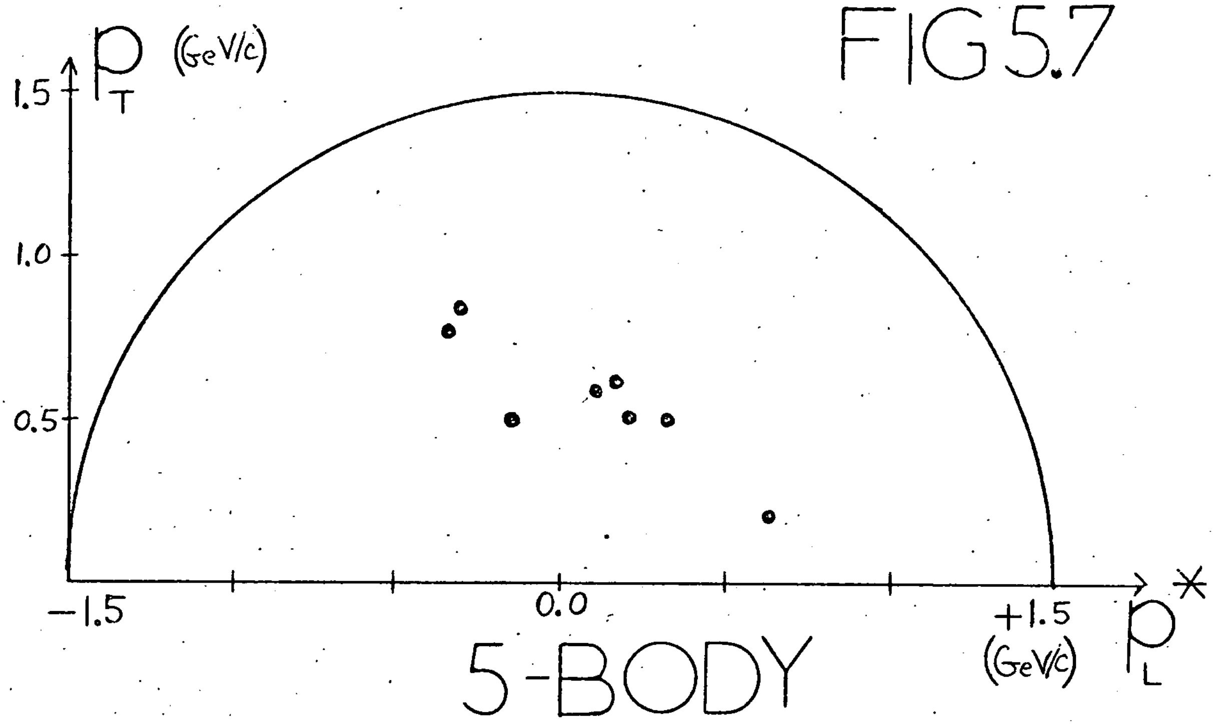

FIG 5.8

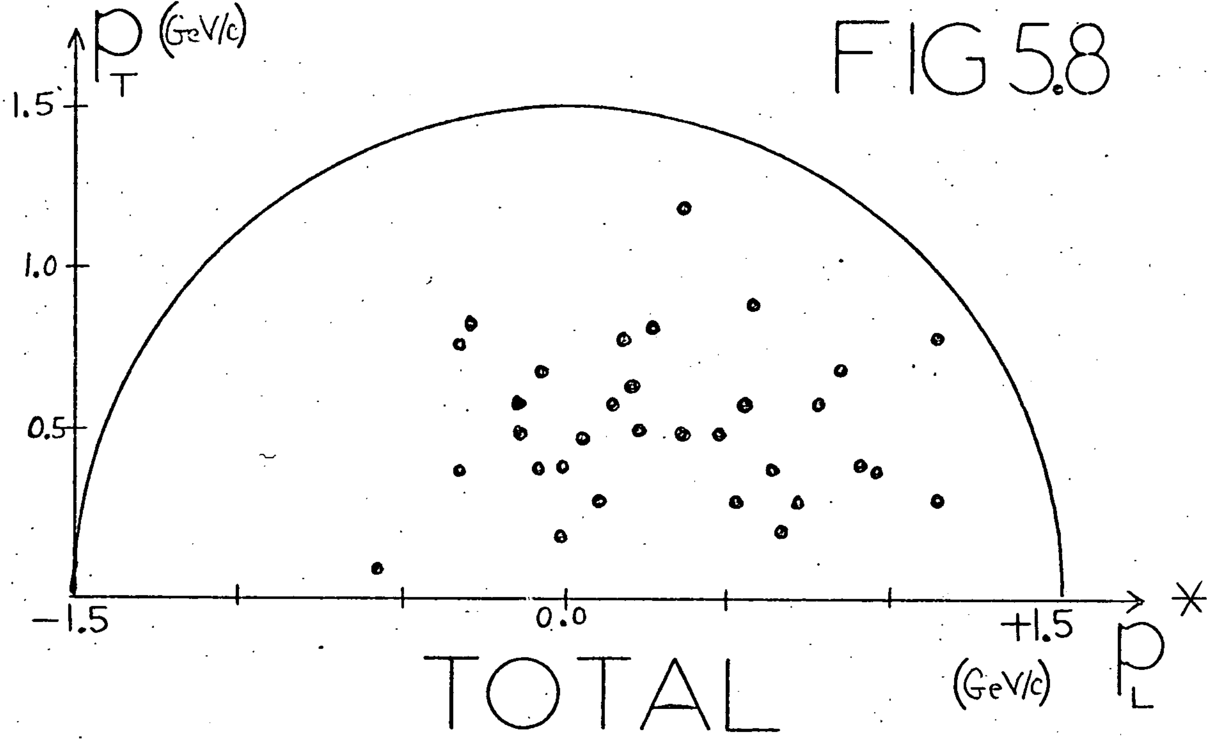

Peyrou Plots of $\overline{\Xi}^{+}$ final states.

FIG 5.9

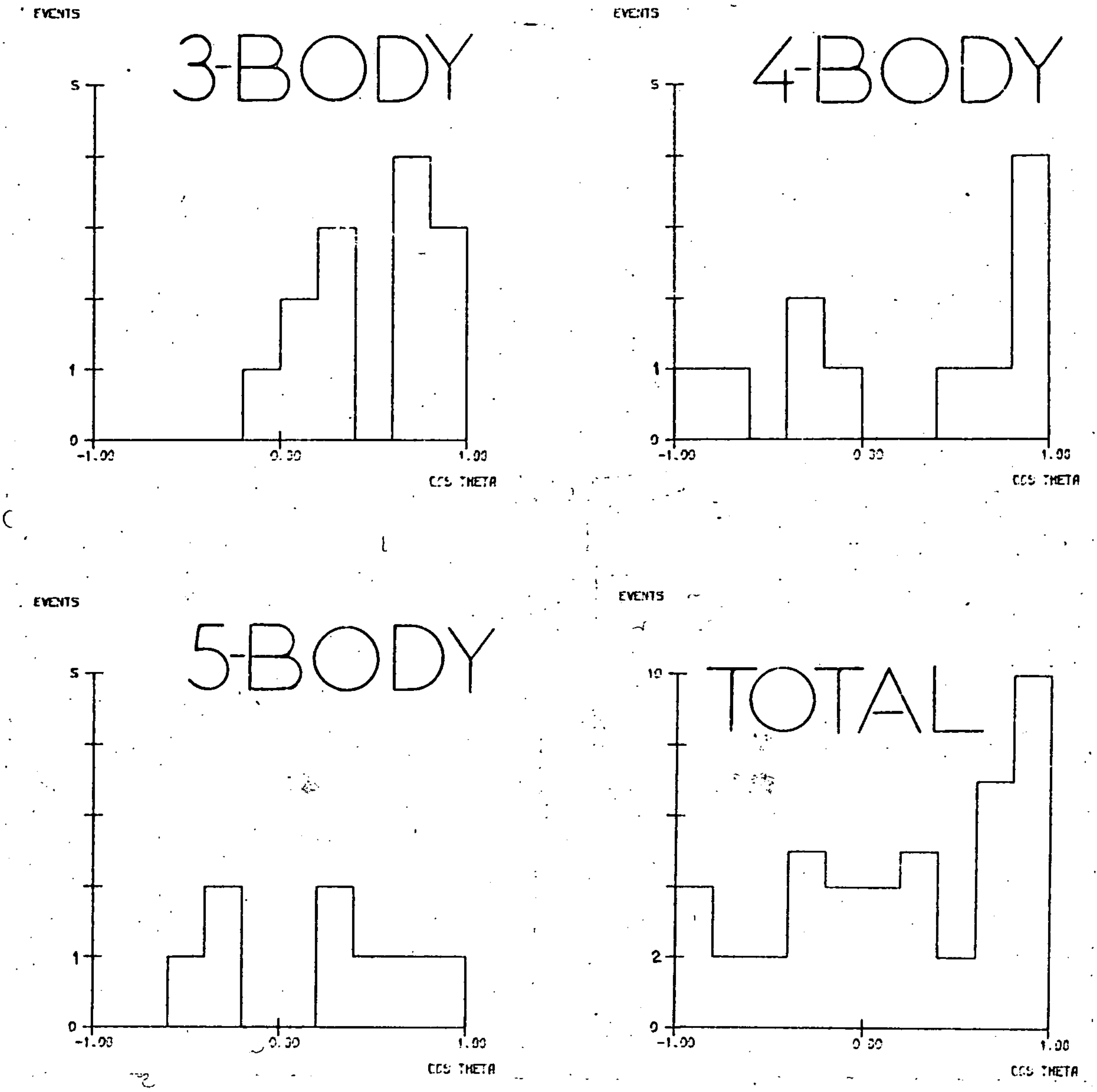

CMS Production angles of the $\overline{\Xi}^{+}$.

FIG 5.10

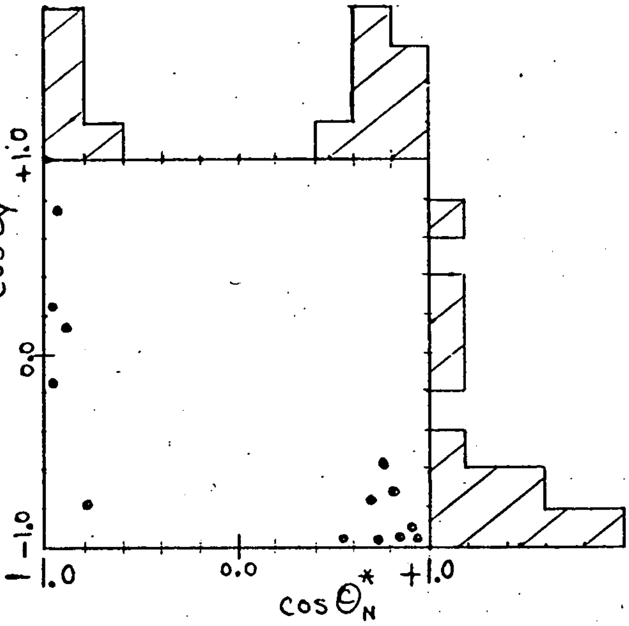

3-BODY Ξ^+

Hyperon-nucleon angular correlation in the CMS.

FIG 5.11

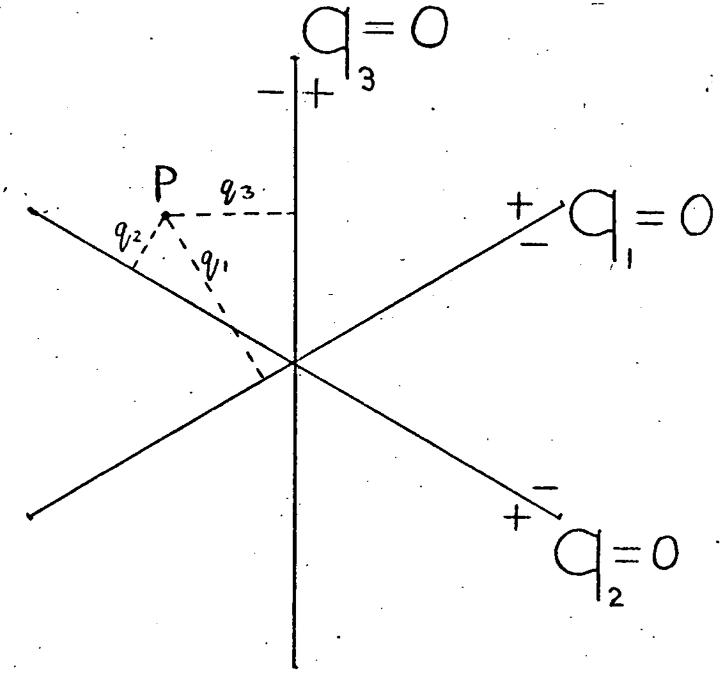

The Hexagonal Plot.

5.4.3 Production Characteristics of the Anti-Cascade in 3-Body Final States

The simplest $\overline{\Xi}^{+}$ final states are the 3-body states,

$$\overline{\Xi}^{+}\text{PY} \quad .$$

One useful method of examining the C.M.S. distributions of these particles is to use a longitudinal phase space plot (LPS plot), first suggested by L. Van Hove(7). The usefulness of LPS plots stems from the well-known empirical fact that the transverse momenta of outgoing particles are restricted to small values, the average being $\approx$ 0.3 GeV/c to 0.4 GeV/c for pions and protons respectively, and are largely independent of incident energy. Consequently, when the latter is large, the phase space distribution extends mainly in the directions corresponding to large longitudinal momenta, and many of its characteristic features can be read from analysis of its projection on longitudinal phase space.

5.4.4 The Hexagonal Plot

In the case of a 3-body final state, where the C.M.S. longitudinal momentum of the final particles is q_1, q_2, q_3, each event is represented by a point, P, in the plane of Fig. 5.11, with distances, q_i, to the three lines $q_i = 0$ (these lines cut each other at 60°). This is known as a 'hexagonal plot'. Events with q_i positive (negative) are plotted on the side of the $q_i = 0$ lines marked +(-). Here, q_i is taken positive(negative) for a particle moving in the forward(backward) hemisphere of the C.M.S., the forward direction being that of the incident beam particle.

If the transverse momentum of all the particles is small, one will have a concentration of events near the kinematical border of the plot, and if the final state particles are non-identical, the kinematical boundary intercepts the three axes at different points and has an irregular shape. The Hexagonal plot for the 13 3-body Ξ^+PY states from this experiment is shown in Fig. 5.12, where it is seen that the majority of events fall into that sector where both the proton and the Ξ^+ are emitted forward in the C.M.S., and the hyperon is emitted fast backwards. Since the points are fairly near the boundary of the plot, and considering that the average longitudinal momentum of the proton is higher than that of the Ξ^+, one could construct a double-peripheral exchange diagram to represent such a process, viz.

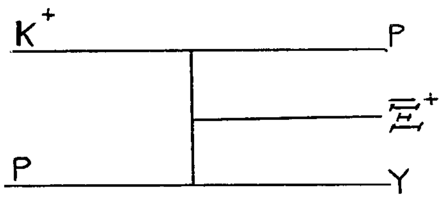

It is known that at high energies, meson-nucleon collisions take place not as 'head-on' collisions, but more as 'glancing' collisions, where particle-like systems are imagined to be exchanged, which carry the quantum numbers required to produce the final state. Thus, the above graph represents a reaction in which there are two exchanges of particles, from the upper to the middle vertex, and from the lower to the middle vertex, e.g. possible exchanges might be $\overline{\Lambda}^0$ and K^+ respectively.

FIG 5.12

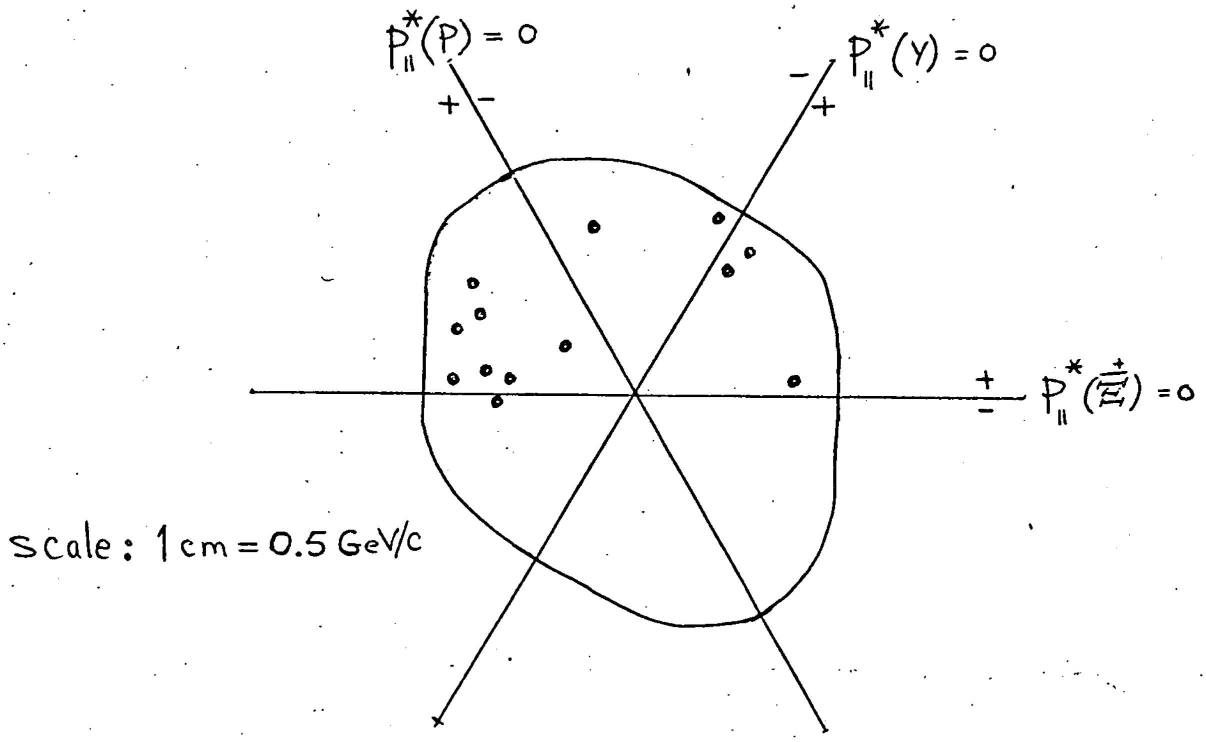

Hexagonal Plot for $\overset{+}{\bar{\Xi}}$PY final states.

FIG 5.13

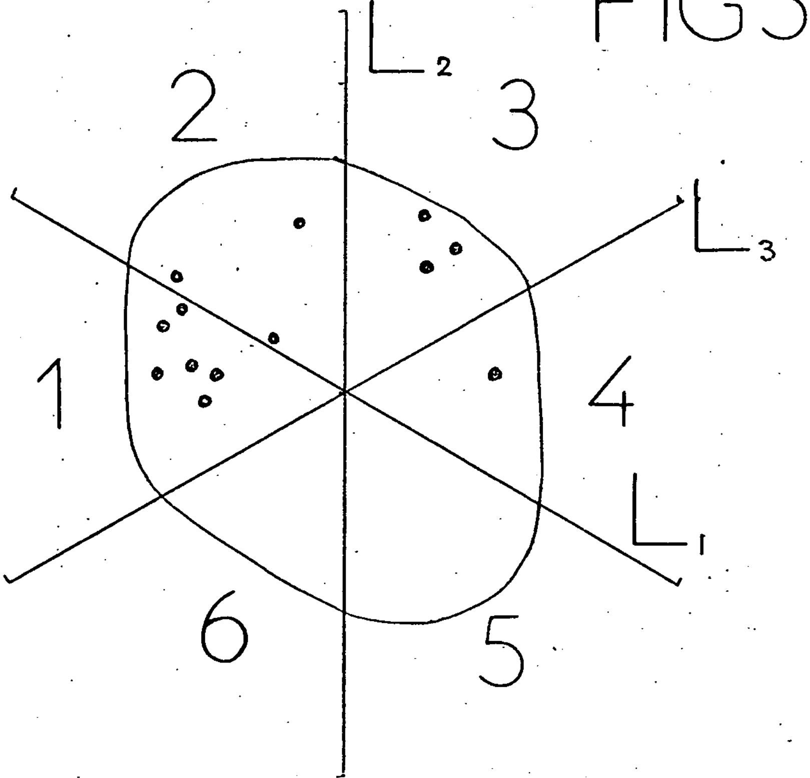

Definition of sectors 1 → 6 in the Hexagonal plot.

Since in any sector of the Hexagonal plot, the identity of the leading particle is ambiguous, one may create new sectors to correspond to the double-peripheral graphs, by constructing the lines L_1, L_2 and L_3, respectively, where $P_{\parallel}^{*}(\Xi^{+}) = P_{\parallel}^{*}(P)$, $P_{\parallel}^{*}(P) = P_{\parallel}^{*}(Y)$, and $P_{\parallel}^{*}(\Xi^{+}) = P_{\parallel}^{*}(Y)$ as shown in Fig. 5.13. One may number these sectors 1 to 6, starting with sector L_1L_3 on the L.H.S. of the diagram. Thus sector 1 corresponds to the graph just considered, and there are six events in this region.

Sector 2 corresponds to

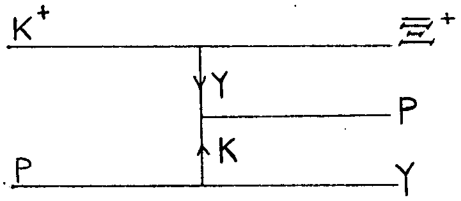

with possible Y^0 and K^+ exchange. There are three events in this region.

Sector 3 corresponds to

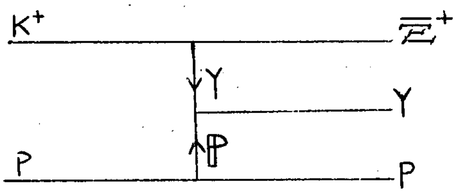

i.e. Possible Y^0 and Pomeron exchange. (The Pomeron carries the quantum numbers of the vacuum.) There are three events in this region which is perhaps surprising since one might expect this process to contribute most.

Sector 4 corresponds to

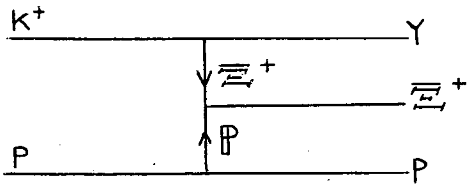

i.e. Ξ^+ exchange, which must be rare, due to the mass and strangeness of the exchanged particle. There is only one event in this region.

Sector 5 corresponds to

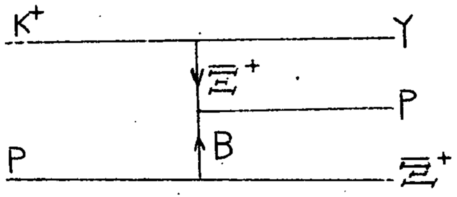

This involves the exchange, at the lower vertex, of a di-baryon state with strangeness, -2. No such state is known to exist, nor is predicted theoretically. This sector contains no events.

Sector 6 corresponds to

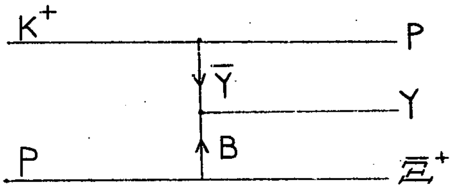

which again involves the exchange of an exotic (i.e. non SU(3)) state. Once again, there are no events in this region.

Thus, the population of the sectors of the Hexagonal plot, as defined above, is in complete accordance with present theoretical predictions about the existence or otherwise of particle states.

5.4.5 The C.L.A. Parametrisation

Amplitudes have been constructed to represent such processes as have just been considered, e.g. in the Chan, Loskiewicz and Allison model (C.L.A. model)$^{(8)}$. The physicists at Birmingham University used those amplitudes which describe the graphs for sectors 1, 2 and 3 in the Hexagonal plot, together with events generated by a Monte Carlo program, and calculated the effect of these amplitudes on the final state, in terms of the angular distribution of the three final state particles. Modest success was achieved in the correspondence between the experimental distributions and those predicted by the C.L.A. 'double Regge model'. Much greater statistics would be required before any firm conclusions could be drawn, regarding such $\overline{\Xi}^+$ production.

5.4.6 The Triangular t-Plot

Another (related) method of looking at possible production mechanisms of 3-body final states is the so-called, 'triangular t-plot', whose boundary is an equilateral triangle, and the perpendicular distances of a point within this boundary to one of the sides, represents 't', i.e. minus the four-momentum transfer squared from the beam particle to each of the outgoing particles in the final state, and since the sum of the momentum transfers is a constant, this gives rise to the equilateral boundary.

If t_{KP} represents minus the four-momentum transfer squared from the incoming beam particle to the final state proton, etc., then the equations of the sides of the triangle are,

$$t_{KP} = 0$$

$$t_{K} = 0$$

$$t_{KY} = 0 \quad .$$

The relevant quantities for the 3-body Ξ^+PY states are shown plotted in Fig. 5.14.

Phase space within this plot is known to be fairly uniform$^{(9)}$, and any concentration of events near the edges of the plot implies a peripheral process.

Examination of Fig. 5.14 revels that the dominant process is one in which the smallest momentum transfers (~ 1.5 (GeV/c)^2) are between K^+ and P, then between K^+ and Ξ^+ (~ 3 (GeV/c)^2), and the largest (~ 10 (GeV/c)^2) between K^+ and Y. This may be represented by the graph,

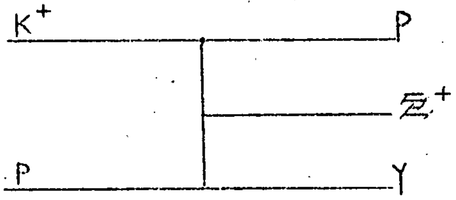

i.e. the triangular t-plot leads to the same general conclusions as the Hexagonal plot, regarding possible production mechanisms, and serves as a useful guide to the extent of the peripheral nature of the reactions.

5.5 Conclusion

The production mechanism of the three-body Ξ^+PY final states can be broadly interpreted by means of a double-Regge model, involving exchanges of known SU(3) states. The Hexagonal plot and the Triangular t-plot were found to be

FIG 5.14

The Triangular t-plot.

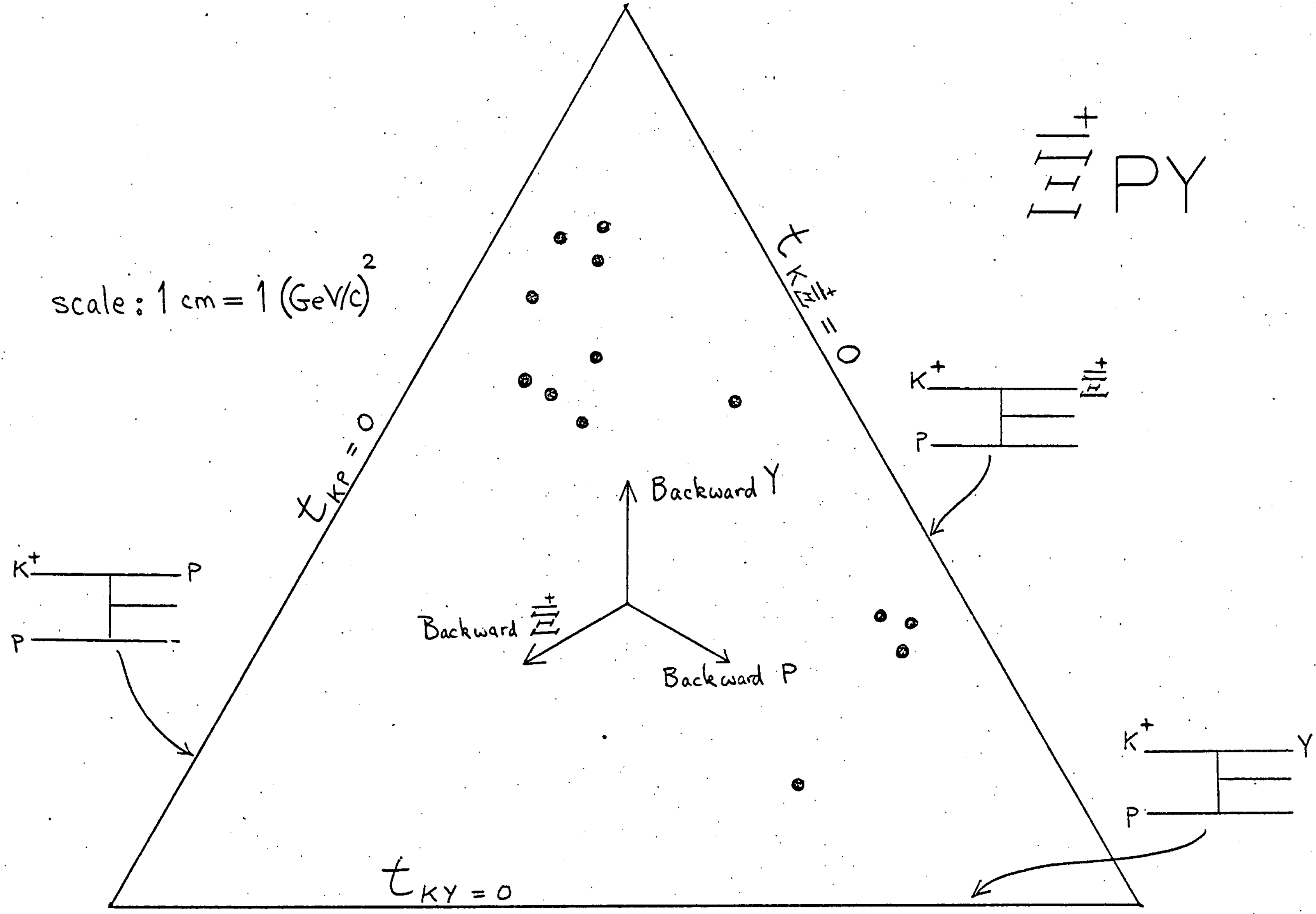

useful aids for the simultaneous examination of the C.M.S. distributions of the three final state particles.

No event was found, whose interpretation could be uniquely assigned to $\overline{\Omega}^+$ production.

5.6 REFERENCES FOR CHAPTER V

(1) Firestone, A. et al, Physical Review Letters 26 (1971) 410-413.

(2) Ahmadzadeh, A. and Biswas, N.N., Nuovo Cimento 19 (1961),958.

(3) Sechi Zorn, B. and Zorn, G.T. Supplement to Nuovo Cimento 26 (1962) 197.

(4) Peyrou, C. 'Proceedings of an International Conference on High Energy Physics, Berkeley' (1960), 157.

(5) Barkas, W.H., Physical Review 124 (1961), 897.

(6) Votruba, M.F. et al., Nuclear Physics B45 (1972) 77-87.

(7) Van Hove, L., Nuclear Physics B9 (1969), 331.

(8) Chan Hong-Mo et al., Nuovo Cimento 57A (1968) 93.

(9) Beusch, W. et al., Physics Letters 28B (1968) 211.

GENERAL CONCLUSIONS

The analysis of the rare events from this experiment has provided useful information on the part played by resonance production in such complicated final states, although the $K\pi$ ambiguities, the small number of constraints, and the low statistics makes detailed investigation difficult.

It would be interesting to study more closely the $K_1^o K_1^o$ state, although collection of the necessary statistics is a daunting task. The data presented in this thesis is derived from the analysis of 500,000 pictures and to obtain more significant statistics would require huge efforts in time and computing.

Useful and interesting information has also been obtained on the anti-cascade final states, in terms of the distribution of final state particles and possible production mechanisms. More sophisticated analysis would again require far greater quantities of data.

APPENDIX 2A

A Justification of the Use of the χ^2 Method of Fitting

After an event has passed through the kinematical fitting program, one has to decide if the tested hypothesis is correct or not. All measured variables are forced to fulfil the constraint equations and the magnitude of " χ^2" is dependent on the difference between fitted and measured values.

Let there exist a set of variables, $v = (v_1, v_2, \ldots, v_n)$ for which one has independent estimates, m, assumed to belong to normal distributions with variances, $\sigma_1^2, \sigma_2^2, \ldots, \sigma_n^2$. Let there also be a set of functions (constraints) $f(v) = 0$, which the variables obey but which are not satisfied by the estimates. One hopes to find an improved set, $m+c$, such that $f(m+c) = 0$, and the most probable set.

The probability of c_i lying in $c_i, c_i + dc_i$ is

$$P(c_i)dc_i = \frac{1}{\sigma_i \sqrt{2\pi}} e^{-\frac{1}{2}(c_i/\sigma_i)^2} dc_i$$

and for all independent elements,

$$P(c) = \prod_i P(c_i)$$

$$= \text{const.} \times e^{-\frac{1}{2}\sum(c_i/\sigma_i)^2}$$

- which probability one wishes to maximise, i.e. one should minimise

$$\chi^2 = \sum (c_i/\sigma_i)^2 .$$

The distribution of χ^2 is predictable, if one knows how many elements, c_i and f_i exist.

One can convert the χ^2 value and the number of degrees of freedom (number of constraints minus the number of parameters) into a probability by using the theoretical χ^2 distribution, which gives the probability that χ^2 is greater than or equal to a given value. i.e. the calculated one.

A probability of $< 5^o/o$ is doubtful and one $< 1^o/o$ implies a very unlikely interpretation of the event. However, a single value of χ^2 does not tell too much, unless it happens to be rather large, and the most significant interpretations of χ^2 testing require large numbers of events.

APPENDIX 2B

This appendix gives a list of the hypotheses tried in the two laboratories, Birmingham and Edinburgh, together with the hypothesis numbers. The number of fits obtained from the Run 4 and Run 5 film is listed, with the number of unique fits in brackets, and there is a separate column for the fits obtained from the 'Oxford' Run 1 and Run 3 film, analysed in Edinburgh. The 'F_B' column gives the number of fits obtained in the Birmingham Laboratory.

The 'F_E' column gives the number of fits obtained in the Edinburgh Laboratory.

The 'F_O' column gives the number of fits obtained in the Edinburgh Laboratory, from the Run 1 and Run 3 only.

The 'NHYP' column gives the hypothesis number, and an asterisk denotes a hypothesis which was not attempted in the Edinburgh Laboratory. Only successful hypotheses are listed.

TOPOLOGY 202

NHYP	F_B	F_E	F_o	Final State
093	36(16)	21(9)	8(4)	$\pi^+ p K^0 K^0 (\bar{K}^0)$
103	35(2)	10(5)	7(1)	$K^+ \pi^+ K^0 \bar{K}^0 (n)$
123	21(0)	5(1)	5(1)	$\pi^+ \pi^+ K^0 K^0 (\Sigma^0)$
133	48(23)	22(12)	10(2)	$\pi^+ \pi^+ \Lambda^0 K^0 (K^0)$
143	25(2)	3(0)	4(0)	$\pi^+ \pi^+ K^0 K^0 (\Lambda^0)$
153	41(9)	10(1)	5(1)	$K^+ \pi^+ K^0 \Sigma^0$
173	25(4)	14(7)	4(1)	$K^+ \pi^+ K^0 \Lambda^0$
183	78(41)	34(22)	20(9)	$K^+ \pi^+ K^0 \Lambda^0 (\pi^0)$
193	22(22)	7(7)	3(3)	$K^+ p K^0 \bar{K}^0$
203	27(9)	16(8)	9(3)	$K^+ p K^0 \bar{K}^0 (\pi^0)$
213	1(0)	1(0)	-	$K^+ p \Lambda^0 K^0 (\bar{n})$
234	1(1)	1(0)	1(1)	$K^+ K^+ K^0 \Xi^0$
244	35(12)	10(3)	11(3)	$K^+ \pi^+ K^0 K^0 (\Xi^0)$
453	1(1)	1(1)	-	$\pi^+ p \Lambda^0 \bar{\Lambda}^0 (K^0)$
463	2(1)	-	-	$\pi^+ p \bar{\Lambda}^0 K^0 (\Lambda^0)$
473	3(1)	2(1)	-	$\pi^+ p \Lambda^0 K^0 (\bar{\Lambda}^0)$
493	-	1(0)	-	$\pi^+ p \Lambda^0 K^0 (\bar{\Sigma}^0)$
665	18(12)	7(4)	2(2)	$K^+ K^+ \Lambda^0 K^0 (\bar{K}^0)$
675	7(0)	8(1)	5(0)	$K^+ K^+ K^0 \bar{K}^0 (\Sigma^0)$
685	5(0)	4(0)	3(0)	$K^+ K^+ K^0 \bar{K}^0 (\Lambda^0)$

Topology 402

NHYP	F_B	F_E	F_o	Final State
013	22(10)	15(9)	3(2)	$K^+\pi^+\pi^+\pi^- K^\circ\Lambda^\circ$
023	60(14)	18(10)	14(4)	$K^+\pi^+\pi^+\pi^- K^\circ\Lambda^\circ(\pi^\circ)$
033	14(1)	9(4)	6(1)	$K^+\pi^+\pi^+\pi^- K^\circ\Sigma^\circ$
043	31(12)	11(4)	6(0)	$\pi^+\pi^+\pi^+\pi^- K^\circ\Lambda^\circ(K^\circ)$
053	12(0)	6(0)	1(0)	$\pi^+\pi^+\pi^+\pi^- K^\circ K^\circ(\Lambda^\circ)$
063	9(2)	6(1)	1(0)	$\pi^+\pi^+\pi^+\pi^- K^\circ K^\circ(\Sigma^\circ)$
073	20(10)	8(6)	2(2)	$K^+ p\pi^+\pi^- K^\circ\bar{K}^\circ$
083	25(6)	14(5)	2(1)	$K^+ p\pi^+\pi^- K^\circ\bar{K}^\circ(\pi^\circ)$
093	22(6)	7(2)	2(0)	$K^+\pi^+\pi^+\pi^- K^\circ\bar{K}^\circ(n)$
103	19(7)	7(1)	4(2)	$p\pi^+\pi^+\pi^- K^\circ\bar{K}^\circ(K^\circ)$
113	10(4)	6(4)	1(1)	$p\pi^+\pi^+K^- K^\circ K^\circ$
123	17(5)	4(0)	3(1)	$p\pi^+\pi^+K^- K^\circ K^\circ(\pi^\circ)$
133	-	2(0)	1(1)	$\pi^+\pi^+\pi^+K^- K^\circ K^\circ(n)$
144	2(0)	2(2)	-	$K^+K^+\pi^+\pi^- K^\circ\Xi^\circ$
154	9(2)	2(2)	-	$K^+\pi^+\pi^+\pi^- K^\circ K^\circ(\Xi^\circ)$
195	-	-	1(0)	$K^+K^+\pi^+K^- K^\circ\bar{K}^\circ(n)$
205	2(1)	-	-	$K^+ pK^+\pi^- K^\circ\bar{K}^\circ(\bar{K}^\circ)$
245	5(4)	3(2)	1(1)	$K^+\pi^+\pi^+K^- K^\circ\Lambda^\circ(K^\circ)$
255	2(0)	2(1)	-	$K^+\pi^+\pi^+K^- K^\circ K^\circ(\Lambda^\circ)$
265	3(1)	1(0)	-	$K^+\pi^+\pi^+K^- K^\circ K^\circ(\Sigma^\circ)$
275	1(1)	5(1)	1(1)	$K^+K^+\pi^+\pi^- K^\circ\Lambda^\circ(\bar{K}^\circ)$
295	4(0)	-	2(0)	$K^+K^+\pi^+\pi^- K^\circ\bar{K}^\circ(\Sigma^\circ)$
603	-	1(1)	-	$K^+ p\pi^+\pi^- \Lambda^\circ\bar{\Lambda}^\circ$
905	-	1(0)	-	$K^+ pK^-\pi^+ K^\circ\bar{K}^\circ(K^\circ)$
966	-	1(1)	-	$K^+K^+K^-\pi^+ K^\circ K^\circ(\Xi^\circ)$

Topology 211

NHYP	F_B	F_E	F_0	Final State
013	5(5)	2(2)	-	$\Sigma_p^+ K^+ K^\circ$
023	8(8)	2(2)	2(2)	$\Sigma_\pi^+ K^+ K^\circ$
033	19(6)	12(7)	5(2)	$\Sigma_p^+ K^+ K^\circ(\pi^\circ)$
043	28(11)	20(9)	5(2)	$\Sigma_\pi^+ K^+ K^\circ(\pi^\circ)$
053	15(4)	8(3)	3(0)	$\Sigma_p^+ \pi^+ K^\circ(K^\circ)$
063	33(15)	18(6)	6(3)	$\Sigma_\pi^+ \pi^+ K^\circ(K^\circ)$
072	1(0)	-	-	$\overline{\Xi}^+ p(\Lambda^\circ)$
082	3(2)	-	-	$\overline{\Xi}^+ p \Lambda^\circ$
092	1(1)	-	-	$\overline{\Xi}^+ p \Lambda^\circ(\pi^\circ)$
102	2(2)	2(2)	-	$\overline{\Xi}^+ \pi^+ \Lambda^\circ(n)$
112	3(2)	-	-	$\overline{\Xi}^+ p \Sigma^\circ$
122	1(0)	2(2)	1(1)	$\overline{\Xi}^+ p(\Sigma^\circ)$
163	-	4(0)	-	$\overline{\Sigma}^+ p K^\circ(\Sigma^\circ)$
183	2(0)	4(0)	-	$\overline{\Sigma}^+ p K^\circ(\Lambda^\circ)$
203	1(1)	1(0)	-	$\overline{\Sigma}^+ p \Lambda^\circ(K^\circ)$
223	-	2(0)	-	$\overline{\Sigma}^+ K^+ \Lambda^\circ(n)$
243	2(0)	-	-	$\Sigma_p^+ p K^\circ(\overline{\Sigma}^\circ)$
253	-	2(0)	-	$\Sigma_\pi^+ p K^\circ(\overline{\Sigma}^\circ)$
263	3(1)	-	-	$\Sigma_p^+ p K^\circ(\overline{\Lambda}^\circ)$
273	3(0)	5(0)	-	$\Sigma_\pi^+ p K^\circ(\overline{\Lambda}^\circ)$
293	1(1)	-	-	$\Sigma_\pi^+ p \overline{\Lambda}^\circ(K^\circ)$
333	1(0)	-	-	$\Sigma_\pi^+ K^+ \overline{\Lambda}^\circ(n)$
463	-	1(0)	-	$\overline{\Omega}_K^+ \pi^+ \Lambda^\circ(\Lambda^\circ)$
473	-	1(0)	-	$\overline{\Omega}_\pi^+ \pi^+ \Lambda^\circ(\Lambda^\circ)$
482	1(1)	-	-	$\Sigma_p^+ p \overline{\Xi}^\circ$
492	1(1)	1(1)	-	$\Sigma_\pi^+ p \overline{\Xi}^\circ$
502	1(0)	-	-	$\overline{\Xi}^+ p \overline{K}^\circ(n)$

Topology 212

NHYP	F_B	F_E	F_o	Final State
012	3(1)	1(1)	-	$\overline{\Xi}^+ p \Sigma^\circ$
022	2(0)	-	-	$\overline{\Xi}^+ p \Lambda^\circ$
032	-	1(1)	-	$\overline{\Xi}^+ p \Lambda^\circ (\pi^\circ)$
062	-	1(1)	-	$\overline{\Xi}^+ p \overline{K}^\circ (n)$
074	1(1)	-	-	$\overline{\Xi}^+ K^+ \Lambda^\circ (\Sigma^\circ)$
172	3(3)	-	-	$\overline{\Xi}^+ \pi^+ \Lambda^\circ (n)$
224	1(1)	1(1)	-	$\overline{\Sigma}^+ p K^\circ \Lambda^\circ$
314	1(1)	2(2)	-	$\Sigma^+_p \pi^+ K^\circ K^\circ$
324	1(1)	2(2)	-	$\Sigma^+_\pi \pi^+ K^\circ K^\circ$
364	-	1(1)	-	$\Sigma^+_\pi p K^\circ \overline{\Lambda}^\circ$
x 585	2(2)	-	-	$\Sigma^+_\pi K^+ K^\circ K^\circ (\overline{K}^\circ)$
x 613	2(2)	-	-	$\Sigma^+_p \pi^+ K^\circ K^\circ (\pi^\circ)$
x 623	3(3)	-	-	$\Sigma^+_\pi \pi^+ K^\circ K^\circ (\pi^\circ)$

Topology 203

NHYP	F_B	F_E	F_o	Final State
x 055	2(1)	-	-	$K^+ p K^\circ K^\circ \overline{K}^\circ (\overline{K}^\circ)$
083	2(2)	2(2)	-	$\pi^+ p K^\circ K^\circ \overline{K}^\circ$
093	1(1)	2(2)	-	$\pi^+ p K^\circ K^\circ \overline{K}^\circ (\pi^\circ)$
135	-	1(1)	-	$K^+ K^+ \Lambda^\circ K^\circ \overline{K}^\circ$
x 155	1(0)	-	-	$K^+ K^+ K^\circ \overline{K}^\circ \overline{K}^\circ (n)$
x 185	1(1)	-	-	$K^+ \pi^+ K^\circ K^\circ \overline{K}^\circ (\Sigma^\circ)$
x 195	1(1)	-	-	$K^+ \pi^+ K^\circ K^\circ \Lambda^\circ (\overline{K}^\circ)$
213	6(3)	2(0)	-	$\pi^+ \pi^+ K^\circ K^\circ \Sigma^\circ$
223	4(1)	4(2)	-	$\pi^+ \pi^+ K^\circ K^\circ \Lambda^\circ$
233	8(8)	4(4)	-	$\pi^+ \pi^+ K^\circ K^\circ \Lambda^\circ (\pi^\circ)$
x 253	2(2)	-	-	$\pi^+ \pi^+ K^\circ K^\circ \overline{K}^\circ (n)$

Topology 411

	NHYP	F_B	F_E	F_o	Final State
	232	1(1)	1(1)	-	$\overline{\Xi}^+ p p \pi^- (\overline{K}^0)$
	262	-	1(1)	-	$\overline{\Xi}^+ p \pi^+ \pi^- (\Sigma^0)$
	272	3(2)	1(1)	-	$\overline{\Xi}^+ p \pi^+ \pi^- (\Lambda^0)$
*	299	1(0)	--	-	$\Sigma_p^+ K^+ K^+ K^- K^0 (\pi^0)$
*	309	2(0)	-	-	$\Sigma_\pi^+ K^+ K^+ K^- K^0 (\pi^0)$
	319	9(5)	4(4)	2(2)	$\Sigma_p^+ K^+ \pi^+ \pi^- K^0$
	329	19(13)	13(11)	2(2)	$\Sigma_\pi^+ K^+ \pi^+ \pi^- K^0$
	332	1(0)	-	-	$\overline{\Xi}^+ p \pi^+ K^- (n)$
*	339	9(1)	-	-	$\Sigma_p^+ K^+ \pi^+ \pi^- K^0 (\pi^0)$
*	349	47(15)	-	-	$\Sigma_\pi^+ K^+ \pi^+ \pi^- K^0 (\pi^0)$
*	359	1(1)	-	-	$\Sigma_p^+ K^+ K^+ \pi^- K^0 (\overline{K}^0)$
*	419	6(2)	-	-	$\Sigma_p^+ \pi^+ \pi^+ \pi^- K^0 (K^0)$
*	429	25(7)	-	-	$\Sigma_\pi^+ \pi^+ \pi^+ \pi^- K^0 (K^0)$
*	469	1(1)	-	-	$\overline{\Sigma}^+ p K^+ \pi^- \Sigma^0$
	504	2(0)	-	2(2)	$\Xi^- K^+ K^+ \pi^- (K^0)$
*	735	4(1)	-	-	$\Sigma^- K^+ K^+ \pi^+ K^0 (\overline{K}^0)$
	743	14(3)	5(5)	3(3)	$\Sigma^- K^+ \pi^+ \pi^+ K^0$
*	753	25(9)	-	-	$\Sigma^- K^+ \pi^+ \pi^+ K^0 (\pi^0)$
*	783	13(5)	-	-	$\Sigma^- \pi^+ \pi^+ \pi^+ K^0 (K^0)$

Topology 412

NHYP	F_B	F_E	F_o	Final State
384	-	-	1(1)	$\Xi^- K^+ K^+ \pi^+ K^0 (\pi^0)$
484	-	-	1(1)	$\Xi^- K^+ \pi^+ \pi^+ K^0 (K^0)$
373	-	1(1)	1(1)	$\Sigma^- \pi^+ \pi^+ \pi^+ K^0 K^0$
463	-	1(1)	-	$\Sigma_\pi^+ \pi^+ \pi^+ \pi^- K^0 K^0$

Topology 421

NHYP	F_B	F_E	F_o	Final State
003	-	1(1)	-	$\overline{\Xi}^+ \Sigma_p^+ \pi^+ \pi^- (n)$
182	-	1(1)	-	$\overline{\Xi}^+ \Sigma_\pi^+ p \pi^-$
073	-	1(0)	-	$\Sigma^- \overline{\Sigma}^+ p \pi^+ K^0$
063	-	1(0)	-	$\Sigma_\pi^+ \overline{\Sigma}_\pi^- p \pi^+ K^0$

APPENDIX 3A

Scanning Efficiency

For each event, let p, q, r, s respectively be the probabilities of the event being recognized by neither scanner, scanner A, scanner B, or both.

Then $p + q + r + s = 1$ (1)

Assuming no correlation between the scanning,

$$p = (1 - E_1)(1 - E_2)$$

$$q = E_1(1 - E_2)$$

$$r = E_2(1 - E_1)$$

$$s = E_1E_2$$

where E_1, E_2 are the scanning efficiencies .

Then $ps = qr$ (2)

Let there be a sample of N events (N is of course unknown) of which a, b, c events are detected by scanner A, scanner B, or both. The probability of this happening, for a particular sample is

$$P_N = \frac{N!}{a!b!c!(N-a-b-c)!} \times p^{N-a-b-c} \times q^a \times r^b \times s^c$$

- the powers of p, q, r, s, being the probability of a particular pattern of detection, or non-detection, and the multinomial coefficient being the number of patterns leading to the totals a, b, c.

The expected value of 'a' is

$$\bar{a} = \sum_a \sum_b \sum_c a\, P_N(a)$$

$$= Nq \qquad \text{(after manipulation).}$$

Similarly,

$$\bar{b} = Nr$$

$$\bar{c} = Ns \quad .$$

One then obtains the 'most likely' values of the unknowns N, E_1, E_2 by equating $\bar{a}$, $\bar{b}$, $\bar{c}$ to the observed values of a, b, c. From equations (1) and (2) and using the results just derived, one obtains

$$N = \bar{a} + \bar{b} + \bar{c} + \frac{\bar{a} \times \bar{b}}{\bar{c}}$$

and E, the overall efficiency,

$$E = \frac{\bar{a} + \bar{b} + \bar{c}}{N} \quad .$$

One now requires the standard errors:

$$(\Delta a)^2 = \overline{(a - \bar{a})^2} = \overline{a^2} - \bar{a}^2 \quad .$$

Now $$\overline{a(a-1)} = \sum_a \sum_b \sum_c a(a-1) P_N(a,b,c)$$

$$= q^2 N(N-1) \qquad \text{(after manipulation)} \quad .$$

So that,

$$\overline{(a - \bar{a})^2} = q^2 N(N-1) + qN - (qN)^2$$

$$= a(1-q)N \quad .$$

Similarly,

$$(\Delta b)^2 = r(1-r)N$$

$$(\Delta c)^2 = s(1-s)N \quad .$$

The off-diagonal terms of the error matrix are given by, e.g.

$$\overline{(a - \bar{a})(b - \bar{b})} = \overline{ab} - \bar{a}\,\bar{b}$$

and $$\overline{ab} = \sum_a \sum_b \sum_c ab\, P_N(a,b,c)$$

$$= N(N-1)qr \quad .$$

So that $$(a - \bar{a})(b - \bar{b}) = - Nqr$$

and similarly for the other off-diagonal terms. The standard error on any function, f, of the observed variables, a, b, c is given by

$$(\Delta f)^2 = \left(\frac{\partial f}{\partial a}\right)^2 \overline{(a - \bar{a})^2} + \left(\frac{\partial f}{\partial b}\right)^2 \overline{(b - \bar{b})^2} + \left(\frac{\partial f}{\partial c}\right)^2 \overline{(c - \bar{c})^2}$$

$$+ 2\frac{\partial f}{\partial b}\,\frac{\partial f}{\partial c}\,\overline{(b-\bar{b})(c-\bar{c})} + 2\frac{\partial f}{\partial c}\,\frac{\partial f}{\partial a}\,\overline{(c-\bar{c})(a-\bar{a})} +$$

$$+ 2\frac{\partial f}{\partial a}.\frac{\partial f}{\partial b}\,\overline{(a - \bar{a})(b - \bar{b})}$$

i.e. $$\frac{(\Delta f)^2}{N} = q\left(\frac{\partial f}{\partial a}\right)^2 + r\left(\frac{\partial f}{\partial b}\right)^2 + s\left(\frac{\partial f}{\partial c}\right)^2 -$$

$$- \left(q\,\frac{\partial f}{\partial a} + r\,\frac{\partial f}{\partial b} + s\,\frac{\partial f}{\partial c}\right)^2$$

e.g. for $$N = a + b + c + \frac{ab}{c}$$

$$\frac{(\Delta N)^2}{N} = \frac{1 - E}{s}$$

i.e. $$\frac{\Delta N}{N} = \sqrt{\frac{1 - E}{c}} \quad .$$

For a single scan efficiency, E_a.

$$\frac{(\Delta E_a)^2}{N} \approx \frac{E_a(1 - E_a)}{N^2}$$

i.e. $$\frac{\Delta E_a}{E_a} = \sqrt{\frac{1 - E_a}{c}} .$$

For the overall efficiency, E, let $N_s = a + b + c$.

Then $E = \frac{N_s}{N}$ then $E \pm \Delta E = \frac{N_s}{N \pm \Delta N}$

$$= \frac{N_s}{N} \times \frac{1}{(1 \pm \frac{\Delta N}{N})} \approx \frac{N_s}{N} \times (1 \mp \frac{\Delta N}{N}) = E \mp E.\frac{\Delta N}{N}$$

i.e. $\Delta E = \frac{E \Delta N}{N}$ or $\frac{\Delta E}{E} = \frac{\Delta N}{N}$.

APPENDIX 3B

This appendix gives details of cross-sections calculated from the Birmingham and Edinburgh samples, using the program 'FT' as described in Section 3.4. The cross-sections for events containing a Σ^+ have been calculated from the decay mode, $\Sigma^+ \rightarrow n\pi^+$, only.

σ_E = cross-section calculated from the Edinburgh Sample
σ_B = cross-section calculated from the Birmingham Sample
σ_c = combined cross-section.

Final State	$\sigma_E(\mu b)$	$\sigma_B(\mu b)$	$\sigma_c(\mu b)$
$K^+ P K^\circ \overline{K}^\circ$	14 ± 3	11 ± 4	13 ± 3
$K^+ P K^\circ \overline{K}^\circ (\pi^\circ)$	19 ± 6	9 ± 2	10 ± 4
$K^+ \pi^+ K^\circ \Lambda^\circ$	18 ± 6	9 ± 3	10.5 ± 3
$K^+ \pi^+ K^\circ \Sigma^\circ$	5^{+3}_{-2}	12 ± 3	9 ± 2
$K^+ \pi^+ K^\circ \overline{K}^\circ (n)$	9 ± 3	9 ± 2	9 ± 2
$K^+ \pi^+ K^\circ \Lambda^\circ (\pi^\circ)$	43 ± 10	37 ± 6	39 ± 5
$K^+ \pi^+ K^\circ K^\circ (\Xi^\circ)$	18 ± 7	24 ± 5	22 ± 4
$\pi^+ \pi^+ K^\circ K^\circ \Lambda^\circ$	mean of six values		17 ± 3
$\pi^+ \pi^+ K^\circ K^\circ (\Sigma^\circ)$	25 ± 12	26 ± 7	26 ± 6
$\pi^+ \pi^+ K^\circ K^\circ \Lambda^\circ (\pi^\circ)$	10 ± 8	15 ± 6	13 ± 5
$K^+ \pi^+ \pi^+ \pi^- K^\circ \Lambda^\circ$	20 ± 5	12 ± 2	13 ± 3
$K^+ \pi^+ \pi^+ \pi^- K^\circ \Lambda^\circ (\pi^\circ)$	26 ± 7	22 ± 4	23 ± 3
$K^+ \pi^+ \pi^+ \pi^- K^\circ \Sigma^\circ$	7 ± 3	3 ± 1.5	3.5 ± 2
$K^+ P \pi^+ \pi^- K^\circ \overline{K}^\circ$	12 ± 5	9 ± 2.5	10 ± 2
$K^+ P \pi^+ \pi^- K^\circ \overline{K}^\circ (\pi^\circ)$	14 ± 4	8 ± 2	9 ± 2
$K^+ \pi^+ \pi^+ \pi^- K^\circ \overline{K}^\circ (n)$	5 ± 2	6 ± 2	6 ± 1.5
$K^- P \pi^+ \pi^+ K^\circ K^\circ$	17 ± 8	7 ± 3	8 ± 3
$K^- P \pi^+ \pi^+ K^\circ K^\circ (\pi^\circ)$	6 ± 3	13 ± 4	9 ± 4

Final State	$\sigma_E(\mu b)$	$\sigma_B(\mu b)$	$\sigma_c(\mu b)$
$\pi^+\pi^+\pi^+\pi^-K^\circ K^\circ\Lambda^\circ$	mean of four values		8 ± 2
$\pi^+\pi^+\pi^+\pi^-K^\circ K^\circ(\Sigma^\circ)$	21 ± 9	16 ± 7	18 ± 5
$\Sigma^+K^+K^\circ$	6 ± 4	10 ± 4	8 ± 3
$\Sigma^+K^+K^\circ(\pi^\circ)$	34 ± 10	27 ± 6	29 ± 5
$\Sigma^+\pi^+K^\circ K^\circ$	22 ± 7	23 ± 5	23 ± 4
$\Sigma^+K^+\pi^+\pi^-K^\circ$	41 ± 13	18 ± 5	21 ± 7
$\Sigma^+K^+\pi^+\pi^-K^\circ(\pi^\circ)$	-	34 ± 6	34 ± 6
$\Sigma^+\pi^+\pi^+\pi^-K^\circ(K^\circ)$	-	14 ± 3	14 ± 3
$\Sigma^-K^+K^\circ\pi^+\pi^+$	4 ± 2	3 ± 1	3 ± 1
$\Sigma^-K^+K^\circ\pi^+\pi^+(\pi^\circ)$	-	6 ± 2	6 ± 2
$\Sigma^-\pi^+\pi^+\pi^+K^\circ(K^\circ)$	-	2 ± 1	2 ± 1
$\overline{\Xi}^+P\Lambda^\circ$	mean of three values		0.7 ± 0.5
$\overline{\Xi}^+P\Sigma^\circ$	mean of five values		1.8 ± 0.7
$\overline{\Xi}^+P\Lambda^\circ(\pi^\circ)$	-	$0.5\ ^{+0.7}_{-0.3}$	$0.5\ ^{+0.7}_{-0.3}$)
$\overline{\Xi}^+\pi^+\Lambda^\circ(n)$	mean of three values		$1.9\ ^{+0.8}_{-1.1}$)
$\overline{\Xi}^+K^+\Lambda^\circ(\Sigma^\circ)$	-	$0.5\ ^{+0.7}_{-0.3}$	$0.5\ ^{+0.7}_{-0.3}$)
$\overline{\Xi}^+P\pi^+\pi^-(\Sigma^\circ)$	$1\ ^{+1.3}_{-0.6}$	-	$1\ ^{+1.3}_{-0.6}$)
$\overline{\Xi}^+P\pi^+\pi^-(\Lambda^\circ)$	$0.9\ ^{+1.2}_{-0.6}$	1.0 ± 0.6	$0.9\ ^{+0.6}_{-0.4}$)
$\overline{\Xi}^+P\pi^+K^-(n)$	-	$0.2\ ^{+0.3}_{-0.1}$	$0.2\ ^{+0.3}_{-0.1}$)
$\overline{\Xi}^+PP\pi^-(\overline{K}^\circ)$	$1\ ^{+1.2}_{-0.6}$	$0.3\ ^{+0.4}_{-0.2}$	$0.4\ ^{+0.4}_{-0.2}$)
$\overline{\Xi}^+\Sigma^+(n)$	$5\ ^{+7}_{-3}$	-	$5\ ^{+7}_{-3}$)
$\overline{\Xi}^+\Sigma^+P\pi^-$	$4\ ^{+6}_{-3}$	-	$4\ ^{+6}_{-3}$)
$\overline{\Xi}^+\Sigma^+\pi^+\pi^-(n)$	$3.5\ ^{+4}_{-2}$	-	$3.5\ ^{+4}_{-2}$)
$\Xi^-K^+K^+\pi^+(K^\circ)$		$0.3\ ^{+0.4}_{-0.2}$	$0.3\ ^{+0.4}_{-0.2}$)

APPENDIX 3C

Derivation of the Likelihood Function for N(Observed)

The probability of obtaining 'n' events in a channel with a cross-section, σ, is Poissonian.

i.e. $$P_n = \frac{a^n e^{-a}}{n!}$$

where a is proportional to σ, $a = \lambda\sigma$ say.

In a large number of trials (e.g. runs), the mean number, $\bar{n}$, in that channel, will be

$$\bar{n} = \sum_{n=0}^{\infty} n P_n = a .$$

So $\bar{n} = \lambda\sigma$, i.e. λ is the usual factor of track length × density.

It is required to find the likelihood of a particular value of σ, given an observation of 'n' events. The likelihood is just P_n.

i.e. $$\mathcal{L}(\sigma) = P_n = \text{Likelihood,}$$

then $$\ln\mathcal{L} = n \ln(\lambda\sigma) - \lambda\sigma - \ln(n!) \qquad (1)$$

$$\frac{d}{d\sigma}(\ln\mathcal{L}) = \frac{n}{\sigma} - \lambda = 0 \text{ for max. likelihood}$$

i.e. $$\sigma = \frac{n}{\lambda} \text{ :- usual result.}$$

$$\frac{d^2}{d\sigma^2}(\ln\mathcal{L}) = -\frac{n}{\sigma^2}$$

so, $$\ln\mathcal{L} = \ln\mathcal{L}_o + (\sigma - \sigma_o)\left(\frac{d}{d\sigma}\ln\mathcal{L}\right)_{\sigma=\sigma_o} + $$
$$+ \tfrac{1}{2}(\sigma - \sigma_o)^2\left(\frac{d^2}{d\sigma^2}\ln\mathcal{L}\right)_{\sigma=\sigma_o} + \ldots \text{ (Taylor Expansion)}$$

where σ_o = maximum likelihood value, $\frac{n}{\lambda}$, and

$$\ln\mathcal{L} = \ln\mathcal{L}_o - \frac{n}{2\sigma_o^2}(\sigma - \sigma_o)^2 + \ldots.$$

i.e. $\ln\mathcal{L}$ goes down by $\frac{1}{2}$ (one standard error)

when $(\sigma - \sigma_o)^2 = \frac{\sigma_o^2}{n}$

i.e. $\sigma = \sigma_o\left(1 \pm \frac{1}{\sqrt{n}}\right)$ - usual result.

Higher terms in the Taylor series can be ignored when n is large. To find how large n must be one takes

$$\frac{d}{d\sigma^3}(\ln\mathcal{L}) = \frac{-2n}{\sigma_o^3}.$$

Then $\frac{1}{6}(\sigma - \sigma_o)^3\left(\frac{d^3}{d\sigma^3}\ln\mathcal{L}\right)_{\sigma=\sigma_o} = \frac{-n}{3\sigma_o^3}(\sigma - \sigma_o)^3$

$= \pm\frac{1}{3\sqrt{n}}$ at the standard error limit.

Then choosing $n > 5$ gives a correction $\lesssim \frac{1}{7}$. But if $n = 1$ or 2, say, one has to return to equation (1),

$$\ln\mathcal{L} = n\ln(\lambda\sigma) - \lambda\sigma - \ln(n!)$$

$$\ln\mathcal{L}_o = n\ln n - n - \ln(n!)$$

and $\ln(\mathcal{L}/\mathcal{L}_o) = n\ln\left(\frac{\lambda\sigma}{n}\right) - (\lambda\sigma - n)$

$= -\frac{1}{2}$ at the standard error limit.

Then, $\ln\left(\frac{\lambda\sigma}{n}\right) - \frac{\lambda\sigma}{n} + 1 = -\frac{1}{2n}$.

Let $x = \frac{\lambda\sigma}{n}$

then $\ln x - x + 1 = -\frac{1}{2n}$ at the error limit.

If this function, $f(x) = -\frac{1}{2n}$, is tabulated for n(observed) it has the shape shown in Fig. 3.24. It may be seen that $f(x)$ is very asymmetric for $n = 1,2,\ldots, 5$, but as n increases, the standard error on σ becomes very symmetric.

For $n = 1$, $\sigma = \frac{n}{\lambda}\left(1 \begin{smallmatrix} +1.5 \\ -0.7 \end{smallmatrix}\right)$

For $n = 3$, $\sigma = \frac{n}{\lambda}\left(1 \begin{smallmatrix} +0.7 \\ -0.45 \end{smallmatrix}\right)$ etc.

In general, if x_1 and x_2 are the lower and upper intercepts, respectively, of $f(x)$ with $-\frac{1}{2n}$, then,

$$\sigma = \frac{n}{\lambda}\left(1 \begin{matrix} +(x_2 - 1) \\ -(1 - x_1) \end{matrix}\right) .$$

APPENDIX 4A

'Phase Space'

The two body effective mass spectrum from a final state containing four or more particles is expected to be of the form,

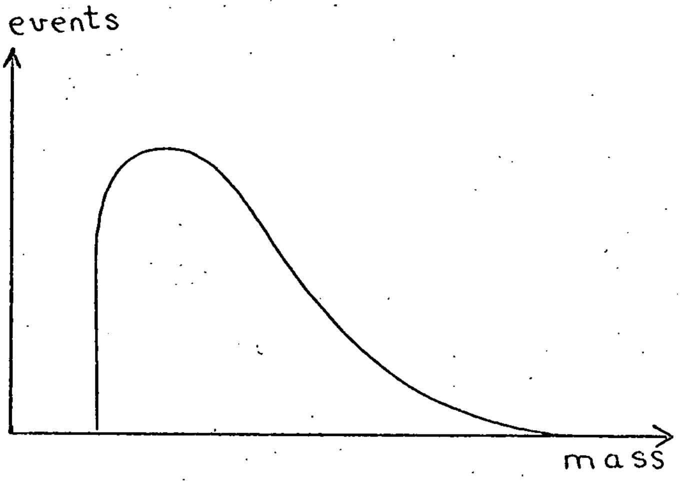

where the tangent to the distribution at the lower mass end is at 90° to the x-axis, and at the upper end, at 0° to the x-axis. The distribution should be smooth without any narrow peaks. If, however, a short-lived resonance exists in the mass combination, then the distribution will show a peak at this mass.

8.A.4

Nuclear Physics B45 (1972) 77–87. North-Holland Publishing Company

MULTIPLE STRANGE - PARTICLE PRODUCTION by 10 GeV/*c* K^+ MESONS in HYDROGEN

M.F. VOTRUBA, ALI SAFDER,
Department of Physics, University of Birmingham

T.M. RATCLIFFE,
Department of Physics, University of Edinburgh

Received 28 February 1972

Abstract: Production cross sections for channels involving $\bar{\Xi}^+$ particles $(20.9 {}^{+6.1}_{-3.4})$ μb, Ξ^- particles (2.3 ± 1.0) μb, $\bar{\Omega}^+$ particles (an upper limit of $\lesssim 1$ μb), and other strange particle channels, are given. An $\bar{\Xi}^+$ production mechanism is suggested, in terms of a double-Regge exchange model, not involving exotic trajectories. The values of the $\bar{\Xi}^+$ mass (1321.6 ± 0.8) MeV/c^2 and lifetime $(1.55 \pm {}^{0.35}_{0.20}) \times 10^{-10}$ sec are in good agreement with those of the Ξ^-.

1. INTRODUCTION

We present results of a study of K^+p interactions at 10 GeV/*c* in which more than one strange particle in the final state is produced. The data were collected from 290 000 stereophotographs forming part of a 500 000 pictures exposure of the 2m HBC to a 10.1 ± 0.1 GeV/*c* K^+ beam at CERN P.S., ref. [1]. The proton contamination of the beam was estimated to be less than 2%. The film was analysed jointly by Birmingham and Edinburgh - Glasgow Universities, and the cross sections calculated using the two independent estimates from the two laboratories. The film was scanned for any events which had a neutral-decay pointing either to a production vertex or to any charged-particle decay vertex. The events recorded were processed using the Rutherford Laboratory series of programs. For the Birmingham sample of film and the accepted fiducial region, the microbarn-equivalent was (0.110 ± 0.010)μb/event (before the efficiency corrections); for the Edinburgh-Glasgow sample, it was (0.216 ± 0.030)μb/event.

The selection criteria in kinematic fitting of hypotheses essentially agree with those of Scotter et al., ref. [2]. All fitted hypotheses were checked for consistency with track ionisation by a physicist. A 1% cut-off level on the probability for accepting a production vertex fit it was used. Four-constraint fits at production vertices were preferred against one-constraint fits, and the hyperon-decay fits were accepted in preference to K-decay fits for decays of fast and short charged particle tracks.

2. THE CROSS SECTIONS

Cross sections for reactions shown in tables 1, 2 and 3 were calculated from the observed number of events (fits) by applying the following multiplicative factors:

(a) Corrections for scanning losses, applied to individual topologies (the average value over all topologies was about 1.04);

(b) Correction factors for the probability cut-off (1.01);

(c) Corrections for loss of events which repeatedly failed to pass through our processing and analysing system (about 1.20);

(d) Correction factors taking into account the neutral decays of Λ^0 hyperons (1.53) and K^0 mesons (2.92);

Table 1
Cross sections for the observed $\bar{\Xi}^+$ final states at 10 GeV/c.

Reaction	No. of fits	Unique events	σ(μb)
$\bar{\Xi}^+ p\Lambda^0$	6	2	0.7 ± 0.5
$\bar{\Xi}^+ p\Sigma^0$	10	6	1.8 ± 0.7
$\bar{\Xi}^+ p\Lambda^0\pi^0$	1	1	$0.5 ^{+0.7}_{-0.3}$
$\bar{\Xi}^+ \pi^+\Lambda^0 n$	6	6	1.9 ± 0.8
$\bar{\Xi}^+ p\bar{K}^0 n$	2	1	$1.7 ^{+2.2}_{-1.1}$
$\bar{\Xi}^+ K^+\Lambda^0(\Sigma^0)$	1	1	$0.5 ^{+0.7}_{-0.3}$
$\bar{\Xi}^+ p\pi^+\pi^-(\Sigma^0)$	1	1	$1.0 ^{+1.3}_{-0.6}$
$\bar{\Xi}^+ p\pi^+\pi^-(\Lambda^0)$	4	3	$0.9 ^{+0.6}_{-0.4}$
$\bar{\Xi}^+ p\pi^+K^-(n)$	1	0	$0.2 ^{+0.3}_{-0.1}$
$\bar{\Xi}^+ pp\pi^-(\bar{K}^0)$	2	2	$0.4 ^{+0.4}_{-0.2}$
$\bar{\Xi}^+ \Sigma^+_n n$	1	1	$2.5 ^{+3.5}_{-1.5}$
$\bar{\Xi}^+ \Sigma^+_p\pi^+\pi^- n$	1	1	$1.7 ^{+2.2}_{-1.1}$
$\bar{\Xi}^+ \Sigma^+_n p\pi^-$	1	1	$2.1 ^{+2.8}_{-1.4}$
$\bar{\Xi}^+$multineutral	14	14	5.0 ± 1.6
$\bar{\Xi}^+$total	51		$20.9 ^{+6.1}_{-3.4}$

Table 2
Cross sections for the observed Ξ^- final states at 10 GeV/*c*.

Reaction	No. of fits	Unique events	$\sigma(\mu b)$
$\Xi^-K^+K^+\pi^+(K^0)$	1	1	$0.3^{+0.4}_{-0.2}$
Ξ^- multineutral	5	5	2.0 ± 0.8
Ξ^- total	6		2.3 ± 1.0

(e) A momentum-dependent correction factor of the form $1/(1-\alpha p)$, with $\alpha \approx 0.1$, to correct for a loss of small-angle, fast kinks (the average weight for reactions involving a charged hyperon was about 1.40);

(f) Momentum-dependent correction factors for the neutral hyperon decay escape probabilities (for the given fiducial volume);

(g) A correction (weighting) factor for events ambiguous between several hypotheses fits, of the form $(1/n)$. No error was allowed for using this method of correction.

Obviously, the product of these correction factors represents a weight attached to each seen event.

The total (overall) $\bar{\Xi}^+$ production cross section, including 14 multi-neutral $\bar{\Xi}^+$ events which gave only (3c and 4c) kink fits, but not complete production and multivertex fits, is $(20.9^{+6.1}_{-3.4})$ μb. In total, we measured 47 events each containing an $\bar{\Xi}^+$ hyperon, out of which in 35 events the $\bar{\Lambda}^0$ visibly pointed to the charged-particle decay vertex. No $\bar{\Omega}^+$ final states decaying via

$$\bar{\Omega}^+ \rightarrow \bar{\Lambda}^0 K^+ ,$$

or

$$\bar{\Omega}^+ \rightarrow \bar{\Xi}^+ \pi^0$$

channels have been reliably detected, thus giving the upper limit of cross section of about $\simeq 0.5$ μb (depending on the assumed mean weight), and the upper limit of the ratio $(\bar{\Omega}^+/\bar{\Xi}^+)$ exp. $\approx 1/47$.

At the same time, altogether 6 cascade Ξ^- final states have been seen (one of a type $\Xi^-K^+K^+\pi^+K^0$, the rest of a multineutral nature with only kink fits complete), giving the overall weighted cross section of (2.3 ± 1.0) μb. Only four Ξ^0 and one $\bar{\Xi}^0$ events were fitted. The values of the overall cross sections for $\bar{\Xi}^+$ and Ξ^- production are in reasonable (2.0 standard deviations) agreement with the values quoted (e.g.) in ref. [3], viz., $\sigma_{\bar{\Xi}^+} = (10.0 \pm 3)\mu$b and $\sigma_{\Xi^-} = (2.5 \pm 1)\mu$b; the same can be said about our estimated upper limits for $\bar{\Omega}^+$ production ($\sigma_{\bar{\Omega}} \simeq 0.5$ μb), see ref. [4].

For tables 1, 2 and 3 the errors quoted on the cross sections are a combination

Table 3

Cross sections of the other strange-particle final states at 10 GeV/c (for * see remarks to table 3)

Reaction	No. of fits	Unique events	$\sigma(\mu b)$
$K^+\pi^+K^0\Lambda^0$	39	11	15.7 ± 2.7
$K^+\pi^+K^0\Lambda^0\pi^0$	112	63	38.6 ± 5.1
$K^+\pi^+K^0\Sigma^0$	51	9	5.1 ± 2.9
$K^+pK^0\bar{K}^0$	29	29	12.9 ± 2.7
$K^+pK^0\bar{K}^0\pi^0$	43	16	9.9 ± 3.4
$K^+\pi^+K^0\bar{K}^0n$	45	8	8.9 ± 1.6
$K^+\pi^+K^0K^0(\Xi^0)$	45	14	21.8 ± 4.0
$K^+K^+\Lambda^0K^0(\bar{K}^0)$	24	16	*
$\pi^+pK^0K^0(\bar{K}^0)$	55	25	*
$\pi^+\pi^+K^0K^0\Lambda^0$	98	36	16.6 ± 2.4
$\pi^+\pi^+K^0K^0\Lambda^0\pi^0$	12	12	13.0 ± 4.6
$\pi^+pK^0K^0\bar{K}^0$	4	4	*
$\pi^+\pi^+K^0K^0(\Sigma^0)$	26	1	26.0 ± 5.8
$K^+\pi^+\pi^+\pi^-K^0\Lambda^0$	37	19	13.1 ± 3.1
$K^+\pi^+\pi^+\pi^-K^0\Lambda^0\pi^0$	78	29	22.5 ± 3.3
$K^+\pi^+\pi^+\pi^-K^0\Sigma^0$	23	6	3.5 ± 1.7
$K^+p\pi^+\pi^-K^0\bar{K}^0$	28	18	9.9 ± 2.1
$K^+p\pi^+\pi^-K^0\bar{K}^0\pi^0$	39	12	9.1 ± 2.1
$K^+\pi^+\pi^+\pi^-K^0\bar{K}^0n$	29	6	5.5 ± 1.3
$K^-p\pi^+\pi^+K^0K^0$	16	7	8.3 ± 3.2
$K^-p\pi^+\pi^+K^0K^0\pi^0$	21	5	8.8 ± 3.5
$\pi^+p\pi^+\pi^-K^0K^0(\bar{K}^0)$	26	8	*
$\pi^+\pi^+\pi^+\pi^-K^0K^0\Lambda^0$	60	16	9.7 ± 2.0
$\pi^+\pi^+\pi^+\pi^-K^0K^0(\Sigma^0)$	15	3	18.0 ± 5.3
$\Sigma_p^+K^+K^0$	7	5	2.6 ± 1.1
$\Sigma_n^+K^+K^0$	10	10	4.2 ± 1.4
$\Sigma_p^+K^+K^0\pi^0$	31	13	8.1 ± 2.6
$\Sigma_n^+K^+K^0\pi^0$	48	18	14.4 ± 2.6
$\Sigma_p^+K^0K^0\pi^+$	23	6	3.9 ± 1.0
$\Sigma_n^+K^0K^0\pi^+$	51	17	11.4 ± 2.0

Table 3 (continued)

Reaction	No. of fits	Unique events	$\sigma(\mu b)$
$\Sigma_p^+K^+K^0\pi^+\pi^-$	13	11	4.6 ± 1.4
$\Sigma_n^+K^+K^0\pi^+\pi^-$	32	25	10.3 ± 3.5
$\Sigma_p^+K^+K^0\pi^+\pi^-\pi^0$	9	1	2.4 ± 0.9
$\Sigma_n^+K^+K^0\pi^+\pi^-\pi^0$	47	17	17.1 ± 3.2
$\Sigma_p^+K^0K^0\pi^+\pi^+\pi^-$	6	2	1.5 ± 0.6
$\Sigma_n^+K^0K^0\pi^+\pi^+\pi^-$	25	7	6.8 ± 1.6
$\Sigma^-K^+K^0\pi^+\pi^+$	19	8	2.8 ± 0.8
$\Sigma^-K^+K^0\pi^+\pi^+\pi^0$	25	10	5.6 ± 1.5
$\Sigma^-K^0K^0\pi^+\pi^+\pi^+$	13	5	1.9 ± 0.7

of the standard errors on (a) scanning efficiency, (b) processing efficiency, (c) number of events observed, $\sqrt{n}$, and the error on the μb-equivalent (~ 12.5%).

2.1 *Remarks on the tables 1, 2, 3*

(a) Events with at least one K^0-meson in the final state have been weighted to take account of the long-lived meson K_L^0.

(b) The cross sections quoted for reactions with a $K^0\bar{K}^0$ pair in the final state (but not those with $K^0K^0\bar{K}^0$) are only for those reactions where the $K^0\bar{K}^0$ is in a state of even angular momentum, since we require both particles to be seen i.e. short-lived, and this is not possible if the $K^0\bar{K}^0$ pair is in the state of odd angular momentum, ref. [13]. Where one K^0 (or $\bar{K}^0$) is seen, and a $\bar{K}^0$ (or K^0) is unseen, we make no attempt to calculate a cross section.

(c) Where a cross section is quoted for a reaction with an unseen K^0 or Λ^0, this means that the reaction has not been observed with the V^0 seen. For other reactions, all V^0's have been seen in one mode or another, e.g., $\Lambda^0K^0K^0\pi^+\pi^+$ may be observed with all three V^0's seen, the Λ^0-unseen, or an K^0-unseen, and these three models were actually used to estimate the cross section.

(d) The 'number of fits' column includes events having multiple ambiguous fits.

(e) The 14 identified $\bar{\Xi}^+$ multineutral events gave only complete kink fits. The same applies to the 5 events identified as Ξ^-.

(f) The cross sections for reactions involving a Σ^+, are quoted separately for $\Sigma^+ \rightarrow p\pi^0$ and $\Sigma^+ \rightarrow n\pi^+$, due to the large difference in detection efficiency.

2.2 *Remarks on kinematical ambiguities*

It may be of interest to summarize some of the kinematical ambiguities we have observed, e.g.,

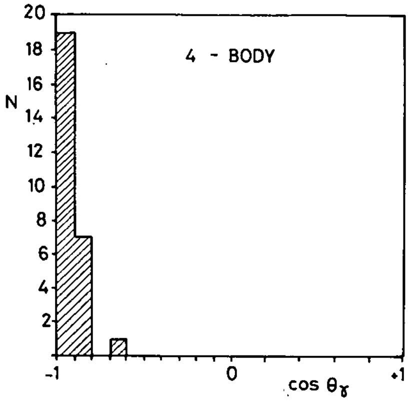

Fig. 1. The Σ^0 -γ angular distribution for 4-body Λ^0/Σ^0 ambiguous events (in c.m.s. of Σ^0).

(a) 26 events were ambiguous between $K^+\pi^+K^0\Lambda^0$ and $K^+\pi^+K^0\Sigma^0$;

(b) 24 events were ambiguous between $K^+\pi^+K^0\Lambda^0(\pi^0)$ and $\pi^+\pi^+K^0\Lambda^0(K^0)$,

(c) 9 events were ambiguous between $K^+pK^0\bar{K}^0(\pi^0)$ and $\pi^+pK^0\bar{K}^0(K^0)$,

(d) The main ambiguity of $K^+\pi^+K^0\bar{K}^0$ (n) was with $\pi^+\pi^+K^0K^0$ (Σ^0) and/or $\pi^+\pi^+K^0K^0(\Lambda^0)$,

(e) 11 events were ambiguous between $K^+\pi^+\pi^+\pi^-K^0\Lambda^0$ and $K^+\pi^+\pi^+\pi^-K^0\Sigma^0$,

(f) 27 events were ambiguous between $K^+\pi^+\pi^+\pi^-K^0\Lambda^0(\pi^0)$ and $\pi^+\pi^+\pi^-\pi^+K^0\Lambda^0(K^0)$,

(g) 32 events were ambiguous between $\Sigma^+K^+K^0(\pi^0)$ and $\Sigma^+\pi^+K^0(K^0)$ (including both Σ^+ decay modes),

(h) 13 events were ambiguous between $\Sigma^+K^+\pi^+\pi^-K^0(\pi^0)$ and $\Sigma^+K^0\pi^+\pi^+\pi^-(K^0)$ (including both Σ^+ decay modes).

Those events ambiguous between Λ^0 and Σ^0 (Λ^0 seen) were apportioned after a study of the Σ^0 -γ decay angle. Although the statistics are limited, we estimate that for the 4-body states, (96 ± 4)% of the ambiguities are genuine Λ^0-events; for the 6-body events, (75 ± 25)% of the ambiguities are genuine Λ^0-events. As an example, the Σ^0 -γ angular distribution for the 4-body events is shown in fig. 1.

3. THE ANTICASCADE FINAL STATES

As seen from table 1, the production of $\bar{\Xi}^+$ occurs in the three, four and five-body final states always containing two other accompanying baryons or hyperons (the Ξ^- events involve 5 and more, bodies). The distributions of $\bar{\Xi}^+$ longitudinal and transverse momenta are shown in fig. 2, with the overall K^+p c.m. angular distributions in fig. 3. These distributions are uncorrected for the hyperon decay and escape probabilities. The mean transverse momentum of our $\bar{\Xi}^+$ sample (all channels) is 0.465 GeV/*c*.

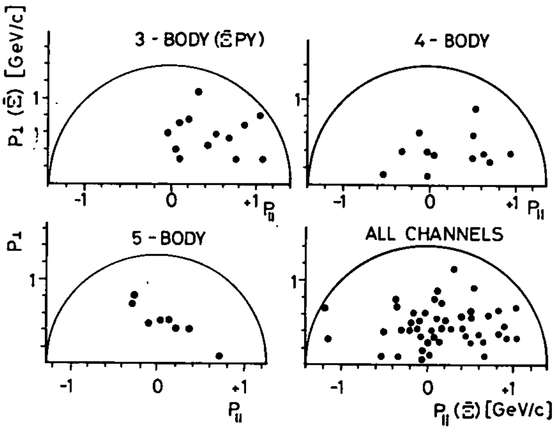

Fig. 2. Peyrou plots for $\bar{\Xi}^+$ produced in various channels (momenta in the overall K^+p c.m.s.).

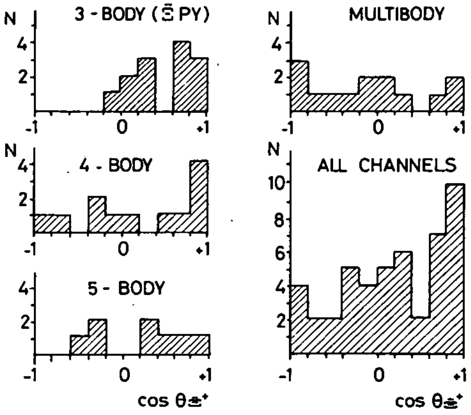

Fig. 3. Angular distributions of $\bar{\Xi}^+$ in the overall K^+p c.m.s.

It can clearly be seen that the fraction of $\bar{\Xi}^+$ emitted forward decreases with increasing number of particles in the reaction. The $\bar{\Xi}^+$'s in the 3-body channels are produced mainly forward. This trend agrees well with that observed by Stone et al., ref. [3] at 12.7 GeV/*c*, while Shen et al., ref. [4] find an essentially isotropic distribution (at 9 GeV/*c* K^+ momentum). Generally, the flattening of angular spectra with increasing number of particles in final states has been found in other high energy interactions, see e.g., a systematic analysis of multibody strange particle final states in proton-proton collisions at 8 GeV/*c*, ref. [5]. It has been known for some time [6], see also a recent paper [3] that, in heavy hyperon production, the accompanying baryons/hyperons show some degree of a forward-backward anisotropy in the overall c.m.s. This effect is present also in our data.

Several production mechanisms may almost certainly be involved; we limit our-

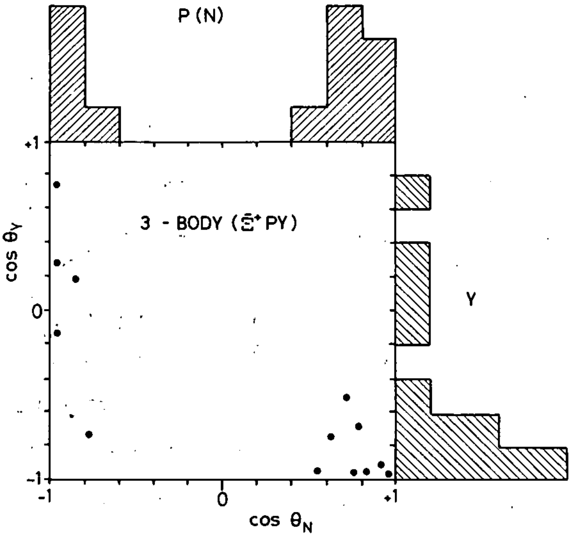

Fig. 4. The hyperon-nucleon angular correlation in Ξ^+ pY states in the K^+p system.

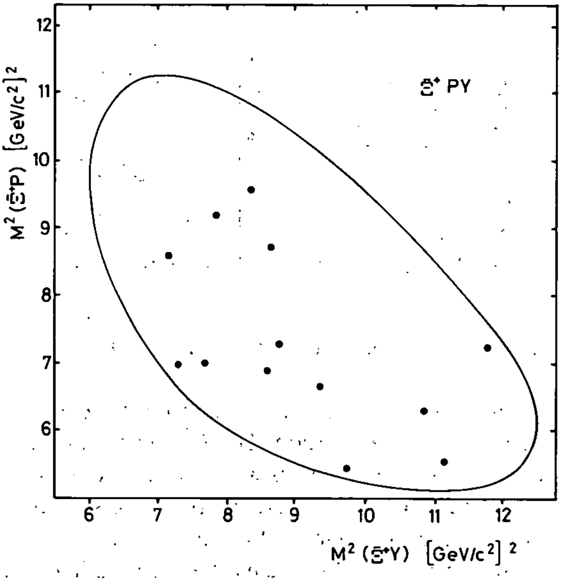

Fig. 5. Dalitz plot for Ξ^+ pY final states.

selves to a more detailed discussion of the 3-body reactions †, $K^+p \to \Xi^+ pY$, for which we present the hyperon-nucleon angular correlations in fig. 4, and the Dalitz plot in fig. 5. Finally, fig. 6 is the Van Hove plot. It is only natural with the low sta-

---

† Both neutral hyperons, Λ^0 and Σ^0, behave very similarly for the present purpose.

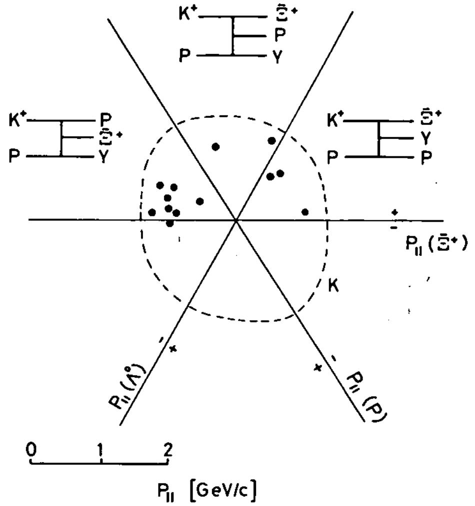

Fig. 6. Van Hove plot for $\bar{\Xi}^+$ pY final states. Curve K calculated for $P_{\perp} \approx 0.4$ GeV/c.

tistics involved that we could not have indications for any mass enhancements. The calculated phase-space distributions for M^2 ($\bar{\Xi}^+$p) combinations has a maximum at about 8(GeV/c^2)^2. The Van Hove plot, on the other hand, has some quite interesting features.

As distinct from the results of Shen et al., ref [4] suggesting possible peripheral single boson or hyperon exchange graphs, Van Hove plot indicates the possibility of (peripheral) double Regge exchange processes [7], viz., that achieved through an incoherent sum of the amplitudes corresponding to graphs in fig. 6. These involve only exchanges of the K$^+$, $\bar{\Lambda}^0$, $\bar{\Xi}^+$ and of the pomeron trajectories. Thus no exotic trajectories seem necessary to explain the data viz., the suggested [4] intermediate boson states with $S = +1$ and the baryon states with $B = 2$ and $S = -1$.

The non-resonant model predictions from the C.L.A. parametrization [8] for all the $\bar{\Xi}^+$ pY final states have been calculated using the FOWL programme [9]; for our case the most relevant angular distributions are given in fig. 7. Although a direct comparison with actual data is difficult due their scarcity, it appears possible to say that, for the three-body (as well as for the quasi-three-body) reaction, the double Regge pole models may naturally represent the basic qualitative features so far seen. Actually, the forward-backward peaking of the accompanying baryons/hyperons is quite well reproduced (compare fig. 4 and fig. 7); the predicted angular distribution of $\bar{\Xi}^+$ appears, however, rather too much peaked towards the extreme forward direction (compare fig. 3 and fig. 7). A more direct and sophisticated fitting is not possible with the present data. It is clear that the number of contributing amplitudes may change, or different (exotic?) amplitudes may also be found important (with respect to those in fig. 6) when there are substantially more data available.

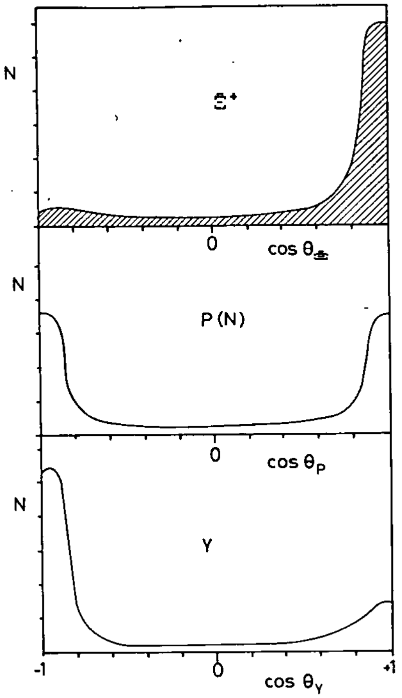

Fig. 7. Smoothed angular distributions from C.L.A. model for the incoherent sum of three amplitudes represented in fig. 6. The vertical axes in arbitrary units.

4. THE $\overline{\Xi}^+$ MASS AND LIFETIME ESTIMATES

The $\overline{\Xi}^+$ particles studied are almost always produced in reactions which are highly constrained, and often $\overline{\Lambda}^o$'s are also seen to decay. In our sample of 47 measured $\overline{\Xi}^+$ events we have 35 measured events in which the Λ^o visibly points to the charged-particle decay vertex. The Birmingham part of the sample (23 events) was re-measured ten times to study possible random measurement errors.

Weighted (by the inverse square of individual errors) values of the relevant quantities were used and the fitted mass of $\overline{\Xi}^+$ from all 35 events $\overline{\Xi}^+ \to \overline{\Lambda}^o \pi^+$ was computed to be (1321.6 ± 0.6) MeV/c^2, where the error is only statistical. Using the maximum likelihood technique [10], with a likelihood function

$$L(\tau) = \prod_i \frac{1}{\tau} \left\{ \frac{\exp(-t_i/\tau)}{[\exp(-t_i^{\min}/\tau) - \exp(-t_i^{\max}/\tau)]} \right\} ,$$

we obtained for the $\overline{\Xi}^+$ lifetime the value $\tau = (1.55 {}^{+0.35}_{-0.20}) \times 10^{-10}$ sec. In the above formula, τ is the proper lifetime to be obtained, t is the observed proper time, $t_i^{\min}$

and $t_i^{\max}$ is the minimum and maximum proper time consistent with the conditions of observation of the *i*th particle. A constant cut-off minimum length of $\overline{\Xi}^+$ track of 0.3 cm was taken.

Using the same measurement and computation procedures we obtained for a sample of 169 well-constrained events containing $\overline{\Lambda}^0$ decays (from a part of the same film batch) the values for the mass $m_{\overline{\Lambda}^0} = (1115.55 \pm 0.34)$ MeV/c^2, and for the lifetime $\tau_{\overline{\Lambda}^0} = (2.45\,^{+0.12}_{-0.11}) \times 10^{-10}$ sec (errors purely statistical). Both these values compare well with the accepted ones [11].

We also tried to take into account possible systematic errors involved in the mass values; following [12] we roughly estimate, in our case, the quadratically combined errors from possible curvature distortions, magnetic field inhomogeneities and a variation in Λ^0 mass value used in fitting, not to exceed ~ 0.50 MeV/c^2. Together with the statistical error already quoted this leads to the resulting uncertainty in the $\overline{\Xi}^+$ mass of (1321.6 ± 0.8)MeV/c^2.

The authors wish to express their gratitude to Dr. D.C. Colley and Dr. G.R. Evans for their constant support and interest in this work, and to Drs. M. Jobes, P.M. Watkins, J.G. Colvine, N.E. Fancey, for help and useful discussions. We are also very grateful to Dr. D.J. Candlin for theoretical discussions. The work on rare events was started by Drs. L. Riddiford and Gillian M. Jones. The authors also express their indebtedness to the crews of the CERN P.S. and of the CERN 2m HBC, as well as to measurement and programming teams in Birmingham and Glasgow-Edinburgh.

The financial support by the U.K. Science Research Council is gratefully acknowledged.

REFERENCES

[1] P. Lazeyras, CERN Internal Report (1968).
[2] D.G. Scotter et al., Nuovo Cimento 62A (1969) 1057.
[3] S.L. Stone et al., Phys. Letters 32B (1970) 515 and the UR 875–307 preprint (1970).
[4] B.C. Shen et al., Phys. Letters 25B (1967) 443 and the UCRL 19408 (1969) report, published in D. Lissauer et al., Nucl. Phys. B18 (1970) 491;
A. Firestone et al., Phys. Rev. Letters 26 (1971) 410.
[5] M. Firebaugh et al., Phys. Rev. 172 (1968) 1354.
[6] J.C. Berlinghieri et al., Phys. Letters 27B (1968) 665;
G. Bassompiere et al., Nuovo Cimento 48A (1967) 589.
[7] J. Ranft, Fortschr. Phys. 18 (1970) 1.
[8] Chan Hong-Mo et al., Nuovo Cimento 57A (1968) 93.
[9] F. James, FOWL Program, CERN Program Library.
[10] C. Baltay et al., Phys. Rev. 140B (1965) 1027.
[11] Review of Particle Properties, by Particle Data Group, at LRL, Berkeley/CERN, Geneva.
[12] P.F. Schultz et al., Phys. Rev. 168 (1968) 1509.
[13] L. Montanet, Yellow Report CERN 67–23, p. 5.